Forschungszentrum Jülich
in der Helmholtz-Gemeinschaft

Development of Ellipsometric Microscopy as a Quantitative High-Resolution Technique for the Investigation of Thin Films at Glass-Water and Silicon-Air Interfaces

Felix Linke

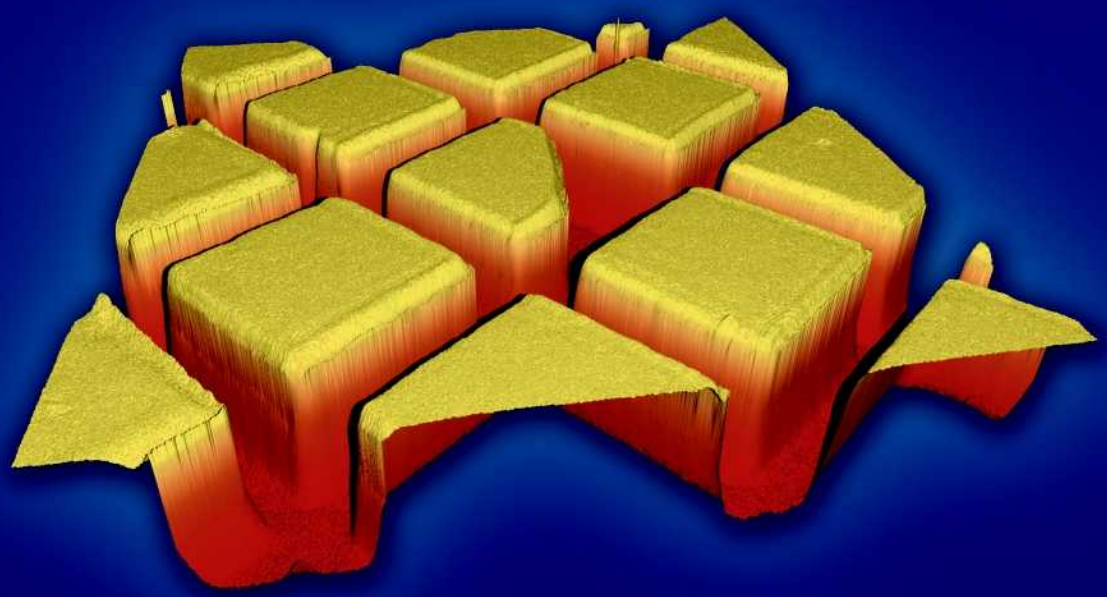

Materie und Material
Matter and Materials

Schriften des Forschungszentrums Jülich
Reihe Materie und Material / Matter and Materials Band / Volume 23

Forschungszentrum Jülich GmbH
Institut für Schichten und Grenzflächen

Development of Ellipsometric Microscopy as a Quantitative High-Resolution Technique for the Investigation of Thin Films at Glass-Water and Silicon-Air Interfaces

Felix Linke

Schriften des Forschungszentrums Jülich
Reihe Materie und Material / Matter and Materials Band / Volume 23

ISSN 1433-5506 ISBN 3-89336-373-4

Bibliographic information published by Die Deutsche Bibliothek.
Die Deutsche Bibliothek lists this publication in the Deutsche Nationalbibliografie; detailed bibliographic data are available in the Internet at <http://dnb.ddb.de>.

Publisher and Distributor:	Forschungszentrum Jülich GmbH Zentralbibliothek 52425 Jülich Phone +49 (0) 2461 61-5368 · Fax +49 (0) 2461 61-6103 e-mail: zb-publikation@fz-juelich.de Internet: http://www.fz-juelich.de/zb
Cover Design:	Grafische Betriebe, Forschungszentrum Jülich GmbH
Printer:	Grafische Betriebe, Forschungszentrum Jülich GmbH
Copyright:	Forschungszentrum Jülich 2004

Schriften des Forschungszentrums Jülich
Reihe Materie und Material / Matter and Materials Band/Volume 23

D 91 (Diss., München, TU, 2004)

ISSN 1433-5506
ISBN 3-89336-373-4

Contents

Abstract

The presented work deals with ellipsometric microscopy, an optical technique for the investigation of thin films. Ellipsometric microscopy combines two powerful optical techniques, microscopy and ellipsometry. The latter technique exploits the fact that the state of polarization of light changes in a well known way upon reflection at interfaces covered by thin films. Ellipsometry is a very accurate technique for simultaneously measuring thin film thickness and refractive index or extinction coefficient. Its main drawback is poor lateral resolution which is overcome in ellipsometric microscopy.

The basic idea of ellipsometric microscopy had been proposed before and its feasibility was shown. The aims of this thesis were twofold. On the one hand, ellipsometric microscopy was to be converted from a qualitative technique into a reliable and quantitative method. On the other hand, the technique had to be improved to a point were the glass-water interface could be investigated for biophysical questions. These goals proved to be very demanding because interpreting ellipsometric data requires an exact control over the angle of incidence and the polarization of light. However, in microscopy it is necessary to use cones of light with opening angles as large as possible. Finding the best balance between these conflicting demands and interpreting the ellipsometric data accurately required careful theoretical analysis and very substantial improvements of the setup.

The former setup was converted into a fully-fledged ellipsometric device. All optical and opto-electronic parts and most opto-mechanical parts of the setup were changed and optimized for the specific demands of the technique. Moreover, approaches for accurate alignment and calibration known from ellipsometry were adapted to ellipsometric microscopy. Zone averaging was implemented for systematic cancellation of remaining experimental uncertainties to first order. In order to enable quantitative experiments it was important to analyze and correct imperfections of the utilized CCD camera. However, the most important issue was to correct for the influence of the imaging optics on the ellipsometric data. This was solved by describing the optical components as part of the sample, i.e. they were modeled to contribute their own ellipsometric angles Δ and Ψ. The validity of this model and the performance of the improved setup were verified experimentally in the full domain of the ellipsometric angles $\Psi \in [0°, 90°[$ and $\Delta \in [0°, 360°[$ by systematic measurements on calibrated objects. These were silicon substrates coated with carefully controlled thin layers of MgF_2 and ZnS. To the best of my knowledge neither this nor any other approach for correcting the influence of the imaging optics on the ellipsometric data was described before.

It was shown that ellipsometric microscopy was indeed converted into a very reliable and accurate technique: Now heights can be determined on silicon substrates with an accuracy of 1-3 nm at a lateral resolution of 1 μm. Deviations from this limit were only observed for substrates which were most unsuitable for this particular thin film height. Such difficult samples can be easily analyzed if prepared on an alternative silicon substrate exhibiting a contrast layer of thermal silicon oxide. The measured refractive indices were accurate to approximately 2.3% and the height sensitivity of the instrument was observed to be better than 5 Å.

The second aim of this thesis was the quantitative investigation of thin films at glass-water interfaces at high lateral resolution. It proved that this aim was particularly demanding. The reason for this was the low reflectivity of the glass-water interface. Therefore the light intensities obtained at this interface were very weak and masked by stray light created at the optical components constituting the setup. Because of these difficulties quantitative and laterally resolved ellipsometry at glass-water interfaces has never been reported up to now. A very efficient remedy for this problem was found by introducing an additional stray light filtering aperture into the optical setup. While enabling quantitative ellipsometric experiments, this aperture had also an influence on the lateral resolution of the setup. Because no structures with sufficiently well defined edges could be produced on glass substrates this effect was characterized at the silicon-air interface. Etched silicon oxide structures were used for the measurement of the modulation transfer function of the microscope. It was found that down to pinhole sizes of 300 μm the effect on the lateral resolution was negligible. For the most often used pinhole size of 200 μm the lateral resolution was reduced to 1.5 μm.

The addition of this pinhole improved the ellipsometric data very substantially resulting in almost identical performance at glass-water and silicon-air interfaces. This was shown by investigating calibrated thin films of MgF_2 deposited on microscope cover slides. MgF_2 was chosen because its refractive index is close to the ones of most biological materials. However, it was found that for such thin film structures (i.e. glass - biomaterial - water) the ellipsometric angles vary less with thickness than in the case of silicon substrates. Therefore thicknesses of MgF_2 films at the glass water interface could be determined to an accuracy of just 10 nm albeit the accuracy of the ellipsometric angles is close to the one achieved at silicon interfaces. Nevertheless, refractive indices can be obtained with an astonishing accuracy of 0.5%. In view of the intrinsic difficulties of the glass-water interface for ellipsometry, a very good ellipsometric performance at high lateral resolution was achieved.

Chapter 1

Introduction

Thin films and surface coatings play an important role in many technical applications as well as in nature. For example, within living cells ultra thin lipid layers separate compartments, whereas in semiconductor technology thin films of metals and dielectrics are used to construct devices. Besides the classical solid state systems soft surfaces and soft surface coatings have attracted considerable interest during the last years. Furthermore, biophysicists are very often interested in properties of microstructured surfaces and, more importantly, their interactions with cells. For instance microstamped poly-L-lysine structures are frequently used to achieve patterned growth of cells on substrates [Chang et al., 2003, Singhvi et al., 1994]. This induced self assembly of cells can be utilized to study the activity of neuron networks: The neuronal cells are cultured on poly-L-lysine patterned multielectrode arrays serving as trigger or detector of neuronal activity [James et al., 2000]. Furthermore, biosensor devices can be constructed by monitoring changes of surfaces functionalized with different proteins. This allows investigation and detection of binding reactions [Jin et al., 1996]. If the surface is functionalized on a microscopic scale, high throughput screening of substances is possible and can aid pharmacology to accelerate drug discovery [van Noort et al., 2000].

These examples show that there is a strong need to develop analytical techniques for thin films. An ideal technique should be non-destructive and combine high lateral with superb vertical resolution. Additionally it would be most desirable that the technique is able to discern different materials and that it can operate with many different types of thin film solid state supports. In this thesis an existing technique, ellipsometric microscopy, was advanced to the state where it meets all these requirements.

Ellipsometry is a non-invasive, label-free optical method for measuring thickness with high accuracy (< 1 Å). Additionally optical properties such as the refractive index or the extinction coefficient can be determined at the same time. This allows for discrimination of different materials or enables indirect measurements of quantities affecting the refracting index, e.g. temperature or concentration. The technique utilizes that light changes its state of polarization upon reflection at the coated surface. By measuring this change and applying a mathematical model based on multiple reflections one can infer the desired quantities [Azzam and Bashara,

1996]. Hence, characterization of hidden layers which are inaccessible to other techniques is also possible. The combination with microscopy yields high spatial resolution (ca 1 μm), allowing for investigation of microstructured surfaces.

In the past many light microscopy techniques were invented that are based on interferometry [Feke et al., 1998, Pluta, 1989b, Shatalin et al., 1995]. While these techniques are well established and exhibit impressive resolution, they are not able to discern thickness and index of refraction simultaneously.

To overcome this limitation alternative approaches based on ellipsometry were developed and meanwhile several imaging ellipsometric instruments are commercially available. As will be discussed in Section 1.1 none of these approaches is entirely satisfactory.

An approach which overcomes these difficulties by enabling an optical microscope to perform ellipsometric measurements was presented in Neumaier et al. [2000]. In this setup, called "ellipsometric microscope", the high lateral resolution of the microscope could be maintained. The technique avoids scanning of the sample and allows ellipsometric image formation in a parallel manner, resulting in fast acquisition times. Unfortunately measurements at silicon substrates with different heights of thermal silicon oxide (SiO_2) showed that the ellipsometric performance of this original setup did not allow accurate height and refractive index determination. In addition the technique was restricted to nontransparent supports of the adsorbed thin film, e.g. silicon substrates.

The aims of this thesis were two-fold: First of all the technique had to be further improved and fully characterized in order to enable accurate quantitative measurements of thin films on silicon substrates. Secondly, modifications had to be implemented for making the instrument more versatile, i.e. allowing for different kinds of thin film solid state supports. Of special interest was the possibility to investigate thin films at the glass-water interface, thus allowing for measurements at biological relevant systems in their native environment. This aim turned out to be particularly demanding as these interfaces reflect very weakly due to the small refractive index difference between substrate (glass) and the ambient medium (water).

This work is structured as follows: The first chapter offers a short overview to other approaches of imaging ellipsometry and closely related techniques (Section 1.1). Chapter 2 gives a short introduction to the theoretical foundation of this thesis. It comprises the description of reflection of polarized light at stratified, planar layers and the basic theory of ellipsometry in the "rotating-analyzer configuration". It concludes by giving an introduction to the Fourier description of coherent image formation within a microscope. In Chapter 3 the setup of the ellipsometric microscope is presented and details about the calibration of the incident angle and the azimuthal angles of the rotating polarization components are explained. Chapter 4 presents a detailed analysis of the most important systematic error sources of this technique. Utilized materials and methods (i.e. preparation of samples, utilized hardware and developed software) are described in Chapter 5. The results are presented in Chapter 6. The experiments are organized in sections according to the employed substrate: First measurements at the air-silicon interface are shown and the necessary calibration procedure for the instrumental polarization of the imaging optics is developed (Section 6.1). As it turned out, ellipsometric measure-

ments of arbitrary thin film materials are now possible with an excellent accuracy. Section 6.2 presents measurements at the glass-water interface. It became apparent that accurate ellipsometric measurements at the glass-water interface were not possible with the existing setup. The analysis of the associated problems led to a modification of the setup, which is presented in Section 6.3. This modification allowed for ellipsometric measurements at the glass-water interface with almost the same accuracy as observed for silicon substrates. The chapter concludes with a detailed analysis of the accomplished lateral and vertical resolution (Sections 6.4 and 6.5). An outlook of this work is given in Section 7.

1.1 Ellipsometers with Spatial Resolution in the Literature

Traditional approaches of imaging ellipsometry frequently utilize one of the following alternatives: either the surface is scanned by a focused laser beam (see Fig. 1.1(a)) or the sample is illuminated by parallel light and the surface imaged onto a CCD camera (see Fig. 1.1(b)).

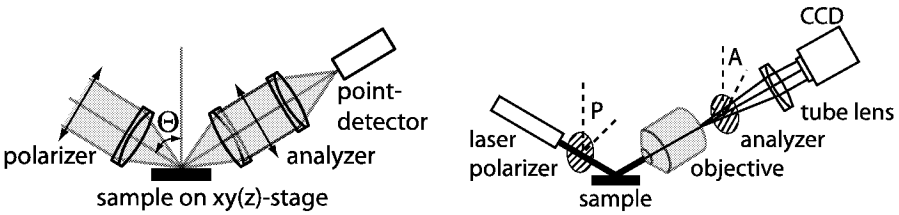

Figure 1.1: (a) Microspot technique and (b) typical setup employing imaging ellipsometry. The microspot technique uses focused light bundles to scan the surface of the sample. In the second configuration the sample is illuminated with a parallel beam of light.

The method of focused light bundles is also used for local point measurements and is often called "microspot optics". The intensity of the reflected light is measured with a point detector, e.g. a photo diode. In order to achieve small spot sizes it is necessary to bundle the light with a large numerical aperture. As the incident angle has to be as close as possible to the Brewster angle of the substrate (75° for air-silicon-interfaces) the smallest achievable spots have a diameter of $\approx 10\,\mu$m, which limits the lateral resolution. In addition the range of the incident angles influences the measurements and has to be corrected for [Erman and Theeten, 1986]. An improvement of this approach was presented by Zhan and Leger [2002b]. Here the objective is placed perpendicularly to the object plane allowing for very small spot sizes. The signal to noise ratio is decreased by illuminating the spot under a certain incident angle from all radial symmetric directions simultaneously. Their design is most distinguished due to its clever use of custom-engineered optical components.

Since scanning the sample is time consuming, most efforts concentrated on the second approach. Its advantage is that it is relatively simple to extend existing point ellipsometer with

the necessary imaging optics. As a result most commercial imaging ellipsometers are based on this scheme (Nanofilm, Göttingen; Optrel, Kleinmachnow). Unfortunately this simple scheme suffers from a number of drawbacks. The tilt angle of the objective is geometrically limited due to collision of objective and sample. This limits the numerical aperture of the objective and thus the lateral resolution to $\approx$ 3-5μm. Because the object plane is tilted with respect to the optical axis of the microscope, the image plane is inclined, too, causing image distortion. The limited depth of focus gives rise to clear image formation only in a narrow strip. The extent of this region depends on the numerical aperture of the objective, i.e. the achievable resolution, and the angle of incidence [Harke et al., 1997]. Employing low magnifications ($M \leq 2$) and being content with poor resolution the image distortions may be removed by setting the CCD camera obliquely to the optical axis [Jin et al., 1996]. Using imaging optics with small numerical aperture the depth of focus problem is also curable [Pak and Law, 1995] - again at cost of poor lateral resolution. Both of the latter cited publications vastly overestimated their achievable resolution by just considering the reproduction scale and not taking into account the diffraction limit due to the imaging optics. At reasonable spatial resolution the limited depth of focus problem can only be cured by mounting the sample to a motorized translation stage and merging several consecutively scanned images with help of an image processing software [Harke et al., 1997].

Ellipsometric setups can be realized in many ways. The most common configurations are either of the rotating-analyzer or of the null-ellipsometry kind (see Section 2.2). Imaging ellipsometer setups were based on both kinds. While the majority of the published setups were based on null-ellipsometry [Jin et al., 1996, Liu et al., 1994, Reiter et al., 1992], Albersdörfer et al. [1998] utilized the rotating-analyzer configuration. The major advantage of setups employing null ellipsometry is their fast image acquisition and the reduced demands on the CCD camera: because measurements proceed at minimum intensity detector nonlinearities are not an issue and cheap CCD cameras are sufficient. Most commercial instruments rely on null-ellipsometry (Nanofilm, Optrel). Null-ellipsometry approaches suffer from the drawback that for inhomogeneous samples minimizing the measured intensity is only possible for one spot and not simultaneously for the full field of view. Within a small thickness range quantitative statements can still be made by applying off-null ellipsometry [Arwin et al., 1993].

Other types of imaging ellipsometers use algorithms for determination of the ellipsometric quantities, which are based on direct intensity measurements at typically four discrete settings of the polarization-optical components [Beaglehole, 1988, Cohn et al., 1988, Pak and Law, 1995]. These instruments are built in the configuration shown in Fig. 1.1(b). This technique demands either an extreme homogeneity of the incident light or a pixel by pixel calibration in order to remove spatial variations of the incident illumination.

A different class of instruments related to ellipsometric microscopes is called *interferometric back focal plane microellipsometer* [Feke et al., 1998, See et al., 1996]. This setup (Fig. 1.2) is similar to the scanning microspot technique, but the intensity distribution in the back focal plane instead of the one in the object plane is imaged onto the CCD camera. In the object space a single point is illuminated with an angular spectrum of plane waves. These waves are reflected at the sample and appear spatially separated in the back focal plane. Angle of inci-

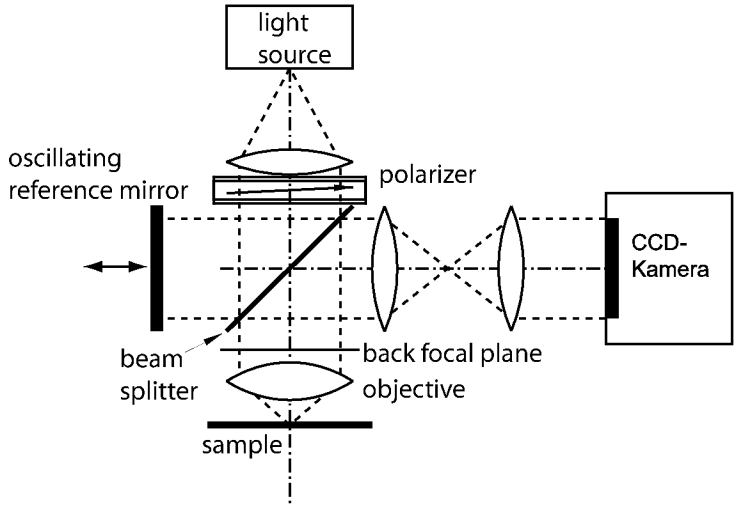

Figure 1.2: Interferometric back focal plane microellipsometry.

dence and radial distance in the back focal plane are related by Abbe's sine condition (Eq. 3.3). At the CCD camera this light interferes with a reference beam and by taking a series of images for several different positions of the reference mirror the amplitude and phase distribution in the back focal plane can be extracted. Thus in principle at each point the ellipsometric angles Ψ-Δ are measured simultaneously for a whole range of incident angles. However, in praxis determination of Ψ seems to be fault-prone. Thus, with help of the determined local phase shift the height profile is determined from the interferogram.

All approaches mentioned above suffer from diffraction limited lateral resolution. First attempts to overcome this limit by usage of near-field optics have been published [Karageorgiev et al., 2001]. Combining an ordinary null-ellipsometer with an SFM[1] enables to obtain images with ellipsometric contrast: the SFM tip interacts with the evanescent field, disturbing the null-ellipsometry conditions. The lateral resolution is determined by the SFM tip dimension. So far no attempt has been undertaken to interpret these pictures quantitatively.

The very advantage of the scheme as realized in this work is the solution to the problem of illuminating the sample under a certain angle of incidence while keeping the optical axis of the imaging microscope perpendicular to the sample, thus allowing for imaging of the surface with high lateral resolution. Finally, a quite unorthodox solution to exactly this problem shall be mentioned: Lheveder et al. [1998] drilled a hole into a custom made Schwarzschild objective allowing for oblique angle illumination without introducing a tilt angle between sample and objective (Fig. 1.3).

[1] SFM: scanning force microscope

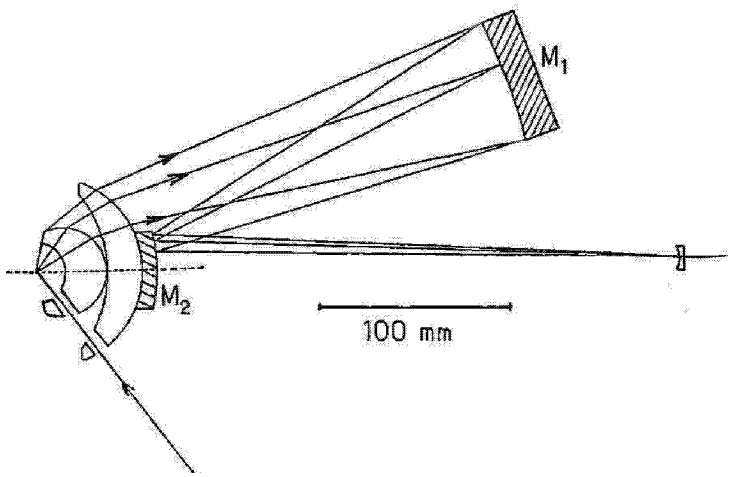

Figure 1.3: Modified Schwarzschild objective. Two front lenses reduce the object side aperture before passing the light into a catadioptric (i.e. based on mirrors $M_{1,2}$) Schwarzschild objective. Drilled holes allow for Brewster angle illumination of the sample. Redrawn from Lheveder et al. [1998].

Chapter 2

Theory

Ellipsometry is a non-invasive, label-free optical method for simultaneous determination of film thickness and optical properties such as the refractive index or the extinction coefficient. The technique relies on measurement of the change the polarization state undergoes due to reflection at the sample. Because every layer within a multi-layer stacked sample influences its reflection properties, the technique is also suited for non-destructive investigations of inner layers.

In this section the physical bases of reflection and transmission of light at interfaces are described. A detailed description of ellipsometry follows and a description of microscopy based on Fraunhofer diffraction concludes the section.

2.1 Reflection of Polarized Light at Layered Interfaces

Whenever light is reflected at an interface between two semi-infinite homogeneous optically isotropic media with complex indices of refraction $n_j = \tilde{n}_j - \mathrm{i}k_j$ ($j \in \{1,2\}$)[1] reflection and transmission is described by the Fresnel formulae [Born and Wolf, 1999]

$$r^p = \frac{n_2 \cos\Theta_1 - n_1 \cos\Theta_2}{n_2 \cos\Theta_1 + n_1 \cos\Theta_t} \tag{2.1}$$

$$r^s = \frac{n_1 \cos\Theta_1 - n_2 \cos\Theta_2}{n_1 \cos\Theta_1 + n_2 \cos\Theta_2} \tag{2.2}$$

$$t^p = \frac{2n_1 \cos\Theta_1}{n_2 \cos\Theta_1 + n_1 \cos\Theta_2} \tag{2.3}$$

$$t^s = \frac{2n_1 \cos\Theta_1}{n_1 \cos\Theta_1 + n_2 \cos\Theta_2}. \tag{2.4}$$

[1] k_j is called the extinction coefficient. If the time dependence of all harmonic fields is chosen to be $e^{\mathrm{i}\omega t}$ k_j fulfills $k_j > 0$.

The electrical field vector of the incident light is decomposed into a component parallel ($\mathbf{E}_p$) and one perpendicular ($\mathbf{E}_s$) to the plane of incidence. $r^{p,s}$ ($t^{p,s}$) are the reflection (transmission) coefficients for those components, Θ_1 is the angle of incidence and Θ_2 the angle of refraction. All angles are measured with respect to the normal of the interface (see Fig. 2.1). The angle of incidence Θ_1 and the angle of refraction Θ_2 are related by *Snell's law*:

$$n_1 \sin\Theta_1 = n_2 \sin\Theta_2 \tag{2.5}$$

In case of absorbing media, i.e. either one or all n_i are complex, the presented equations formally maintain validity. However, the physical picture of the fields becomes complicated [Azzam and Bashara, 1996].

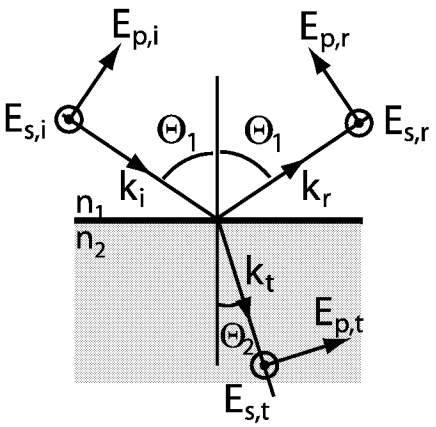

Figure 2.1: Reflection at an interface: Definition of the coordinate systems the wave-vectors $\mathbf{k}_{i,r,t}$ form together with the parallel ($\mathbf{E}_p$) and perpendicular ($\mathbf{E}_s$) components of the electrical field vectors.

If the reflecting surface is more complex, e.g. it is coated with a stack of thin transparent films, the Fresnel formulae need to be extended to stratified planar layer structures. It is assumed that between the two semi-infinite half spaces N-2 thin, isotropic and planar films are located. In order to compute the resulting reflection coefficients for this system all possible multi-reflections within the stack of layers, the attenuation due to reflections and transmissions at each interface and the phase shifts due to propagation of the light waves within the thin films have to be taken into account. In the following a matrix formalism capable to compute the resulting reflection coefficients is described [Azzam and Bashara, 1996].

At each interface *interface matrices*

$$\mathbf{I}^{p,s}_{j,j+1} = \frac{1}{t^{p,s}_{j,j+1}} \begin{pmatrix} 1 & r^{p,s}_{j,j+1} \\ r^{p,s}_{j,j+1} & 1 \end{pmatrix} \tag{2.6}$$

have to be calculated by usage of the Fresnel Formulae (Eq. (2.1)). The superscripts p,s denote that such a matrix has to computed for each eigenpolarization p and s. For the computation of $r^{p,s}_{j,j+1}$ and $t^{p,s}_{j,j+1}$ the *local* angle of incidence

$$\cos\Theta_j = \sqrt{1 - \left(\frac{n_1}{n_j}\right)^2 \sin^2\Theta_1} \tag{2.7}$$

has to be employed. Thereby Θ_1 is the external incident angle (in medium 1 with refractive index n_1). The propagation within each layer is taken into account by the *layer matrices*

$$\mathbf{L}_j = \begin{pmatrix} e^{i\beta_j} & 0 \\ 0 & e^{-i\beta_j,} \end{pmatrix} \tag{2.8}$$

where the phase shift β_j is given by

$$\beta_j = \frac{2\pi}{\lambda} d_j n_j \cos\Theta_j. \tag{2.9}$$

λ denotes the wavelength of the light in vacuum and d_j is the thickness of layer j. After computing the *scattering matrices*

$$\mathbf{S}^{p,s} = \left(\prod_{j=1}^{N-2} \mathbf{I}^{p,s}_{j,j+1} \mathbf{L}_{j+1} \right) \cdot \mathbf{I}^{p,s}_{N-1,N} \tag{2.10}$$

the overall reflection coefficients of the stratified structures can be computed by

$$R_{p,s} = \frac{\mathbf{S}^{p,s}_{21}}{\mathbf{S}^{p,s}_{11}} \tag{2.11}$$

$$T_{p,s} = \frac{1}{\mathbf{S}^{p,s}_{11}}. \tag{2.12}$$

Using Eqs. (2.6)-(2.12) the complex reflection coefficients can be computed in dependence of the composition of the interface, the utilized wave length λ and the incident angle Θ. The equations maintain validity for media with imaginary refractive index (e.g. gold or silicon).

2.2 Ellipsometry

In reflection-ellipsometry a sample is illuminated with monochromized parallel light of a well defined polarization. In any ellipsometric setup the state of polarization after reflection at the sample is measured. The change in the state of polarization can be parameterized by means of the *ellipsometric angles* Ψ and Δ which are defined by the ratio of the reflection coefficients:

$$\tan\Psi \cdot e^{i\Delta} = \frac{R_p}{R_s} = \frac{|R_p|}{|R_s|} \cdot e^{i(\varphi_p - \varphi_s)}. \tag{2.13}$$

The change of the amplitude ratio of the electromagnetic field components is parameterized by $\tan\Psi$. Δ denotes the phase shift introduced between both perpendicular components. The range of the amplitude ratio comprises the interval $[0,\infty]$, i.e. $\Psi \in [0°, 90°]$, while the phase shift Δ is defined in $[0°, 360°[$.

Using a model for the reflection coefficients $R_{p,s}$, e.g. based on Fresnel formulae as described in Section 2.1, one can use the inverse of Eq. (2.13) in order to compute Ψ and Δ for any sample:

$$\tan\Psi = \sqrt{\frac{R_p R_p^*}{R_s R_s^*}} \tag{2.14}$$

$$\cos\Delta = \frac{\Re(R_p R_s^*)}{\sqrt{R_p R_p^* R_s R_s^*}} \tag{2.15}$$

$$\sin\Delta = \frac{\Im(R_p R_s^*)}{\sqrt{R_p R_p^* R_s R_s^*}}. \tag{2.16}$$

The symbols $\Re$ and $\Im$ denote the real and imaginary part operators. Because Ψ is only defined in the first quadrant Eq. (2.14) is sufficient for its determination. Determining Δ from Eq. (2.15) alone results in a quadrant ambiguity. At least the sign of Eq. (2.16) has to be evaluated in order to resolve it (or vice versa).

2.2.1 Interpretation of the Ellipsometric Angles Ψ and Δ

If the incident light is polarized under 45°, i.e. p- and s-component of the electrical field are initially equal in strength, Ψ and Δ can be interpreted in terms of a simple picture: As $\tan\Psi$ describes the ratio of the moduli of the reflection coefficients (see Eq. (2.13) or (2.14)) Ψ is the orientation of the ellipse of the electrical field vector after reflection at the sample (see Fig. 2.2). The meaning of Δ can be demonstrated by looking at the time dependent vector $\mathbf{E}$ in the p-s-coordinate system:

$$\mathbf{E} = \begin{pmatrix} \mathbf{E}_p \\ \mathbf{E}_s \end{pmatrix} = \begin{pmatrix} R_p & 0 \\ 0 & R_s \end{pmatrix} \cdot \begin{pmatrix} 1 \\ 1 \end{pmatrix} E_0 \, e^{i\omega t} \tag{2.17}$$

When the perpendicular component of $\Re(\mathbf{E})$ vanishes

$$\Re(\mathbf{E}_s) = 0$$

the parallel component has a strength of

$$h = \tan\Psi R_s E_0 \sin\Delta. \tag{2.18}$$

Using $H = |R_p| E_0$ (see Fig. 2.2) this results in

$$|\sin\Delta| = \frac{h}{H}, \tag{2.19}$$

i.e. Δ as the phase shift between both perpendicular components influences the ellipticity of the ellipse.

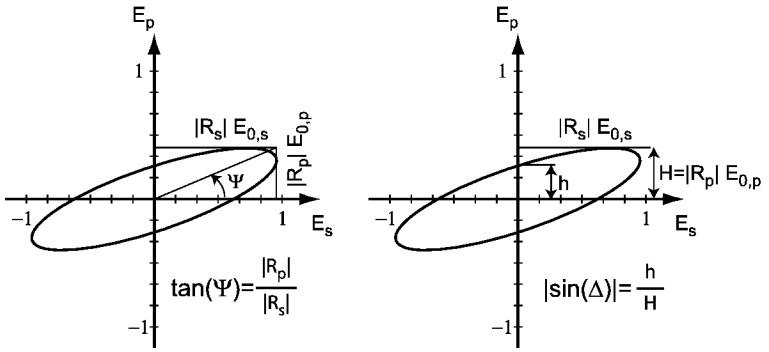

Figure 2.2: Interpretation of Ψ and Δ. If the incident light is polarized under 45°, i.e. p- and s-component of the electrical field were equal in strength, Ψ describes the new orientation and Δ the broadness of the ellipse the electrical field vector describes after reflection at the sample.

2.2.2 The Rotating-Analyzer Setup

Ellipsometric measurements can be realized by many alternative methods [Azzam, 1976, En Naciri et al., 2002, Kleim et al., 1994, Nguyen et al., 1991]. In general, all setups can be divided in two classes: Null-ellipsometers and photometric ellipsometers. Utilizing null-ellipsometry the polarizer and analyzer, which generate the incident and analyze the reflected polarization, are adjusted in order to minimize the intensity at a detector. From the azimuthal settings of these components Ψ and Δ can be computed. Using photometric ellipsometry, e.g. the rotating-analyzer setup applied in this work, the intensity at the detector is measured in dependence of the orientation of a polarizer.

The design of the ellipsometric microscope (see Section 3.1) is based on a rotating-analyzer type ellipsometer [Hauge and Dill, 1973] (see Fig. 2.3). In this kind of ellipsometer the incoming light is linearly polarized at an angle P with respect to the plane of incidence. Light reflected at the sample is analyzed by traversing a rotating polarizer, the analyzer. A $\lambda/4$-wave plate (the compensator) can be rotated into the light path in order to allow for illumination of the sample with elliptically polarized light. Because of the sequence of optical elements this configuration is called P(C)SA-Ellipsometer (polarizer-(compensator)-specimen-analyzer).

The primary measured quantity in this instrument design is the intensity of the light that passes the analyzer set at an azimuthal angle A, $I(A)$. This intensity can be computed from the electrical field strength at the detector $\mathbf{E}_{Det}$.

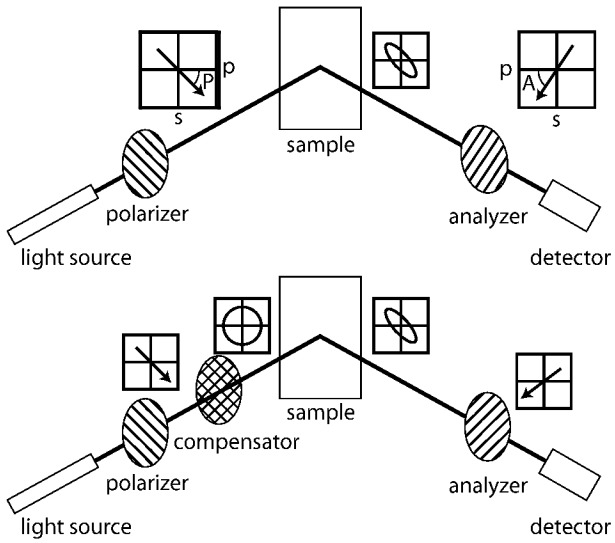

Figure 2.3: Schematic setup of a P(C)SA-ellipsometer. Light with a defined polarization is reflected at a sample. Thereby its state of polarization changes. This change is analyzed by measuring the intensity at the detector as a function of the analyzer orientation A. In order to allow for an unambiguous determination of Δ, measurements with *and* without the compensator have to be performed. Between the optical components the polarization is given schematically with respect to the p-s-coordinate system of the sample.

The PSA-configuration

The electric field strength at the detector can be modeled by usage of the Jones calculus [Azzam and Bashara, 1996]:

$$\mathbf{E}_{Det} = \mathbf{R}_{-A}\,\mathbf{T_A}\,\mathbf{R}_A\,\mathbf{T_S}\,\mathbf{R}_{-P}\begin{pmatrix}1\\0\end{pmatrix}E_0 \tag{2.20}$$

with

$$\mathbf{T_A} = \begin{pmatrix}1 & 0\\ 0 & 0\end{pmatrix} \quad , \quad \mathbf{T_S} = \begin{pmatrix}R_p & 0\\ 0 & R_s\end{pmatrix} = R_s\begin{pmatrix}\tan\Psi e^{i\Delta} & 0\\ 0 & 1\end{pmatrix} \tag{2.21}$$

representing Jones matrices for the analyzer ($\mathbf{T_A}$) and the specimen ($\mathbf{T_S}$). $\mathbf{R}_X$ represents the rotation matrix (with rotation angle X)

$$\mathbf{R}_X = \begin{pmatrix}\cos X & \sin X\\ -\sin X & \cos X\end{pmatrix},$$

A and P denote the azimuthal angles of the polarizer and the analyzer with respect to the plane of incidence of the sample (see Fig. 2.3). E_0 represents the electric field strength transmitted

by the polarizer. Exploiting Eq. 2.20 one finds for the measured intensity, $I(A)$, at the detector

$$I(A) = \mathbf{E}_{Det}^{\dagger} \cdot \mathbf{E}_{Det} = I_0(1 + a\cos(2A) + b\sin(2A)) \tag{2.22}$$

where

$$I_0 = \frac{E_0^2}{2}(R_p R_p^* \cos^2 P + R_s R_s^* \sin^2 P) \tag{2.23}$$

$$a = \frac{R_p R_p^* \cos^2 P - R_s R_s^* \sin^2 P}{R_p R_p^* \cos^2 P + R_s R_s^* \sin^2 P} \tag{2.24}$$

$$b = \frac{2\Re(R_p R_s^*)\cos P \sin P}{R_p R_p^* \cos^2 P + R_s R_s^* \sin^2 P}. \tag{2.25}$$

The symbol $\Re(z)$ denotes the real part of the complex number z. The definition of the ellipsometric angles (Eq. 2.13) together with Eq. (2.24) and Eq. (2.25) yields

$$\tan\Psi = |\tan P| \cdot \sqrt{\frac{1+a}{1-a}} \tag{2.26}$$

$$\cos\Delta = \mathrm{sgn}(\cos P \sin P) \cdot \frac{b}{\sqrt{1-a^2}}. \tag{2.27}$$

The function $\mathrm{sgn}(x)$ returns the sign of x. Because the polarizer orientation P is known it is possible to determine Ψ and Δ of the sample by analyzing the Fourier modes a, b of the normalized intensity incident at the detector. Note the ambiguity in Eq. (2.27), where the quadrant of Δ is undetermined, i.e an ellipsometric angle Δ of δ cannot be distinguished from $360° - \delta$. That is why a second measurement, with a compensator in the light path, is necessary. If the compensator is orientated such that it adds a phase shift of 90° to the incident light, ellipsometric measurements retrieve the $\sin\Delta$. This can be understood from Eq. (2.27): Because the phase shift of the compensator just adds to the phase shift introduced by the sample effectively $\cos(\Delta + 90°) = -\sin\Delta$ is measured and the quadrant ambiguity can be resolved. The following section describes the PCSA-ellipsometer configuration for arbitrary P and C orientations.

The PCSA-configuration

Analogous to Eq. (2.20) the electrical field strength at the detector with a compensator present can be computed by

$$\mathbf{E}_{Det}^{c} = \mathbf{R}_{-A}\,\mathbf{T_A}\,\mathbf{R}_A\,\mathbf{T_S}\,\mathbf{R}_{-C}\,\mathbf{T}_{\lambda/4}\,\mathbf{R}_C\,\mathbf{R}_{-P}\begin{pmatrix}1\\0\end{pmatrix}E_0 \tag{2.28}$$

where C is the angle the slow axis the $\lambda/4$-wave plate encloses with the plane of incidence and $\mathbf{T}_{\lambda/4}$ is the Jones matrix of a $\lambda/4$-wave plate

$$\mathbf{T}_{\lambda/4} = \begin{pmatrix}1 & 0\\ 0 & i\end{pmatrix}. \tag{2.29}$$

The intensity at the detector is

$$I^c(A) = \mathbf{E}_{Det}^{c\dagger} \cdot \mathbf{E}_{Det}^{c} = I_0^c(1 + a^c \cos(2A) + b^c \sin(2A)) \tag{2.30}$$

where

$$I_0^c = \frac{E_0^2}{2}[\alpha R_p^* R_p + \beta R_s^* R_s] \tag{2.31}$$

$$a^c = \frac{\alpha R_p^* R_p - \beta R_s^* R_s}{\alpha R_p^* R_p + \beta R_s^* R_s} \tag{2.32}$$

$$b^c = \frac{2\Re(R_p^* R_s \gamma)}{\alpha R_p^* R_p + \beta R_s^* R_s}. \tag{2.33}$$

In the previous equations the abbreviations

$$\alpha = \cos^2(C-P)\cos^2 C + \sin^2(C-P)\sin^2 C \tag{2.34}$$

$$\beta = \cos^2(C-P)\sin^2 C + \sin^2(C-P)\cos^2 C \tag{2.35}$$

$$\begin{aligned} \gamma &= \sin C \cos C(\cos^2(C-P) - \sin^2(C-P)) - \\ &\quad -i\sin(C-P)\cos(C-P) = \\ &= \gamma_1 + I\gamma_2 \end{aligned} \tag{2.36}$$

have been used. Again, the definition of the ellipsometric angles (Eq. 2.13) together with Eq. (2.32) and Eq. (2.33) are employed in order to relate Ψ and Δ with the Fourier coefficients a^C, b^C of the measured intensity $I^C(A)$:

$$\tan\Psi = \sqrt{\frac{\beta}{\alpha}} \cdot \sqrt{\frac{1+a^c}{1-a^c}} \tag{2.37}$$

$$\sin(\Delta + \tan^{-1}\frac{\gamma_1}{\gamma_2}) = \mathrm{sgn}(\gamma_2) \cdot \frac{b^c}{\sqrt{1-a^{c2}}} \tag{2.38}$$

If the slow axis of the compensator is orientated at 90° these formulae are simplified to

$$\tan\Psi = |\tan P| \cdot \sqrt{\frac{1+a^c}{1-a^c}} \tag{2.39}$$

$$\sin\Delta = -\mathrm{sgn}(\cos P \sin P) \cdot \frac{b^c}{\sqrt{1-a^{c2}}}. \tag{2.40}$$

As already noted at the end of the last section in this case $\sin\Delta$ is measured and the quadrants of the both Δ-measurements, with and without compensator, can be mutually corrected. Thus, a typical measurement always yields two sets of ellipsometric quantities: a set of quadrant corrected (Ψ, Δ) from measurement without compensator and a second set of quadrant corrected (Ψ^c, Δ^c) from measurement with compensator.

If the compensator azimuth is set to $C = 0°$ or $90°$, i.e. $\gamma_1 = 0$, the quadrant ambiguity can be resolved according to the following rules:

$$\text{Correction of } \Delta: \quad \begin{cases} \sin\Delta^c \geq 0 & \Rightarrow \quad \Delta \rightarrow \Delta \\ \sin\Delta^c < 0 & \Rightarrow \quad \Delta \rightarrow 360° - \Delta \end{cases} \tag{2.41}$$

$$\text{Correction of } \Delta^c: \quad \begin{cases} \cos\Delta \geq 0 & \Rightarrow \quad \Delta^c \rightarrow \Delta^c \\ \cos\Delta < 0 & \Rightarrow \quad \Delta^c \rightarrow 180° - \Delta^c \end{cases} \tag{2.42}$$

2.2.3 Determination of n and d from the Ellipsometric Angles

Ellipsometry is an extremely sensitive technique. In favorable cases thicknesses of thin films can be measured with Å accuracy. The task of finding the unknown optical properties of a stratified structure from the ellipsometrically measured ratio of reflection coefficients (Eq. 2.13) is basically just the reverse problem of the equations presented in Section 2.1. Because of the nonlinear and transcendental nature of these equations an analytical inversion is only possible for a few simple special cases, e.g. a three-phase system (ambient-film-substrate) with known refractive indices or a two-phase system with known refractive index of one phase [Azzam and Bashara, 1996]. In all other cases the equations have to be inverted numerically. As the experiment provides two measured quantities (Ψ, Δ) up to two optical quantities can be obtained by ellipsometry. The numerical inversion of the ellipsometric equations proceeds by varying n and d until some error function is minimized, i.e. the optical quantities are obtained by fitting a model function (usually based on the Fresnel equations presented in Section 2.1) to the measured ratio of reflection coefficients (Eq. 2.13). The error function which may be chosen is not unique and can affect the resulting values. Throughout this work the error function

$$G = (\Psi^c(d_j, n_j) - \Psi^m)^2 + (\Delta^c(d_j, n_j) - \Delta^m)^2 \tag{2.43}$$

was employed [Azzam and Bashara, 1996], i.e. the sum of the quadratic deviations of computed (Ψ^c, Δ^c) and measured quantities (Ψ^m, Δ^m) was minimized. An alternative error function could have been based on the complex ratio $\rho = R_p/R_s = \tan\Psi e^{i\Delta}$

$$F \quad = \quad (\delta\rho)^2 = \tan^2\Psi \cdot \left(\frac{4}{\sin^2 2\Psi} \delta\Psi^2 + \delta\Delta^2 \right). \tag{2.44}$$

where $\delta\rho = \rho^c(d_j, n_j) - \rho^m$ is the difference of computed and measured ratio of the reflection coefficients. Comparison with Eq. (2.43) reveals that such an error function weights Ψ-errors with respect to Δ-errors. Such weightening is generally unwanted, but can be introduced if the experimental accuracies of Ψ and Δ differ [Azzam and Bashara, 1996].

2.2.4 Limitations of Ellipsometry

Because of the interferometric nature of the technique Ψ and Δ are periodic in the film thickness, i.e. at an incident angle Θ a film with thickness d has the same ellipsometric character-

istics as a film with thickness $d + D_\Theta$ (see Fig. 2.4), where

$$D_\Theta = \frac{\lambda}{2n_j}(1 - \frac{n_1^2}{n_j^2}\sin^2\Theta)^{-\frac{1}{2}}. \tag{2.45}$$

and n_j is the refractive index of the film. A direct consequence of this periodicity is the fact that for very thin films (how thin depends on the quality of the ellipsometer) ellipsometry suffers from a reduction of measurable quantities: Ψ and Δ depend only on the film thickness d_i of the layer under consideration. This is shown in Fig. 2.4 where Ψ-Δ-trajectories for different refractive indices all emerge with the same slope from the same location, i.e. ultra thin films "look alike". This makes it impossible to determine refractive indices below a

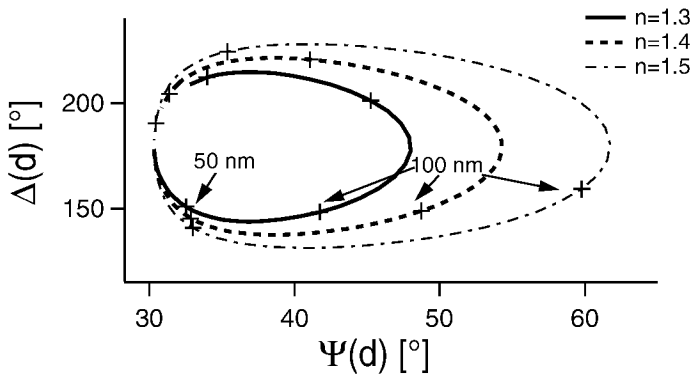

Figure 2.4: Parametric plot of $\Delta(d)$ vs. $\Psi(d)$ for thin films with different refractive indices n on a silicon substrate ($n_{Si} = 4.152 - i * 0.0462$). The thicknesses range from 0 to 210 nm and the incident angle is 53.13°. The crosses mark data points with 50 nm spacing. The periodic nature of Ψ and Δ leads to a degeneration of the ellipsometric quantities at the periodic boundaries, i.e. Ψ and Δ show little dependence on the refractive index n for small thicknesses.

certain thickness. Because of the periodicity of the ellipsometric quantities the same argument holds for all layer thicknesses close to $k \cdot D_\Theta$ ($k \in \mathbf{N}_0^+$). As the phase shift introduced by the thin film ($\sim n_i \cdot d_i$, Eq. (2.9)) is still measured accurately an error in the resulting refractive index affects also the determined film thickness (see Fig. 2.5). For this figure two sets of 50 Gaussian distributed random numbers with standard deviation $\sigma = 0.1°$, one for Ψ and Δ each, were computed and added to calculated Ψ and Δ values in order to simulate statistical experimental errors. From this noisy data n and d were obtained by means of a 2D-fit. Their mean values were plotted against each other and the standard deviations were taken as error bars. This was done for several thicknesses of MgF_2 ($n = 1.389$) in the range of 10 to 240 nm (10 nm spacing). While for intermediate thicknesses the resulting error bars are very small they tend to diverge near the periodic boundaries of Ψ and Δ, meaning that at these thicknesses it is impossible to determine the refractive index and thicknesses accurately. This problem can be avoided by imposing the refractive index and obtaining the thickness d_i by a 1D-fit only.

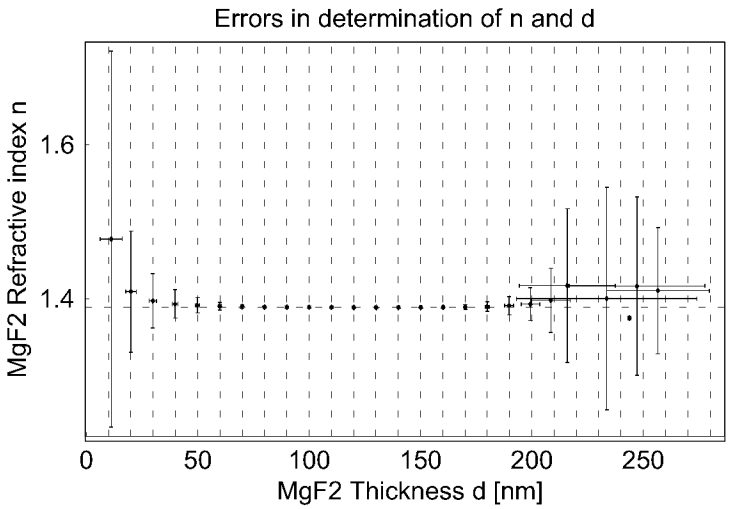

Figure 2.5: Monte Carlo simulation for a silicon substrate with deposited MgF_2 films of various thicknesses. In order to demonstrate accuracy and limitations of ellipsometric measurements refractive indices and thicknesses were retrieved by means of a 2D-fit from artificial noise added Ψ-Δ-pairs (Gaussian, $\sigma = 0.1°$). The mean values of the resulting n- and d-sets were plotted against each other and their standard deviations were taken as error bars. The inaccuracies at the periodic boundaries can be avoided by imposing the refractive index n_i and determination of d_i by means of a 1D-fit. Note, that for clarity of the plot the errors chosen here are not realistic. Realistic estimates on the accuracy of the ellipsometric microscope will be presented in Sections 6.1.2 and 6.3.3.

2.3 Microscopy

The basic design of an infinity-corrected microscope is shown in Fig. 2.6 (left). The object is placed exactly in the front focal plane of the objective. The tube lens forms an intermediate image of the object. The magnification of this intermediate image is given by the ratio of the focal lengths of tube lens (f_{tube}) and objective (f_{obj}). The region of parallel optical trains between tube lens and objective is called *infinity space*. It can be used by microscope manufacturers to add accessories (polarizers, retardation plates, DIC prisms) with little distortion of the image. The intermediate image is viewed through an eyepiece, which further magnifies the image. The final image is formed on the retina of the eye. To the right the simplified layout chosen for the imaging optics applied in this work (right) is shown. Tube lens and objective form an image of the object on the CCD camera.

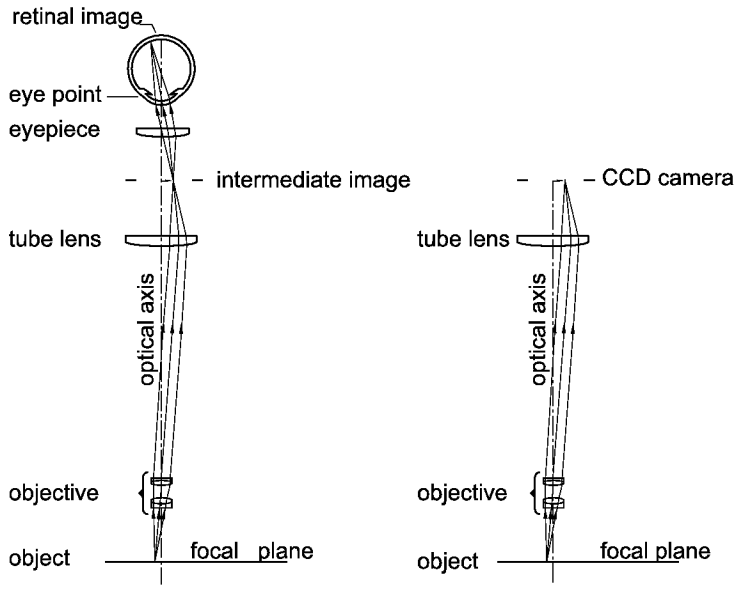

Figure 2.6: Setup of an infinity corrected microscope.

2.3.1 Fourier Description of Microscopy

In 1873 Ernst Abbe proposed a theory for microscope image formation based on Fraunhofer diffraction of light at the object [Born and Wolf, 1999]. Assuming coherent and unpolarized illumination the waves diffracted by the object give rise to a Fraunhofer diffraction pattern in the back focal plane of the objective. If the object's transmittance (or reflectance) can be expressed by a two-dimensional function $F(x,y)$, the optical disturbance $U(\xi,\eta)$ in the back focal plane of the objective is given by

$$U(\xi,\eta) = C_1 \iint_{\mathscr{A}} dx\,dy F(x,y) e^{-i\frac{2\pi}{\lambda}\left[\frac{\xi}{f_{\text{obj}}}x+\frac{\eta}{f_{\text{obj}}}y\right]}, \tag{2.46}$$

where $\mathscr{A}$ is the area in the object plane the object occupies [Born and Wolf, 1999]. It is important to note that Eq. 2.46 was derived under the assumption, that only axis-near rays are considered. In the following it is assumed, that $F(x,y)$ is zero outside this region and the integration with respect to x, y is formally extended to infinity. Every point in the back focal plane of the objective may be considered as a center of secondary disturbance, whose strength is proportional to the amplitude $U(\xi,\eta)$ at that point. Parameterizing any limitations on the aperture in the exit pupil ξ-η-plane by the pupil function $G(\xi,\eta)$ the optical disturbance

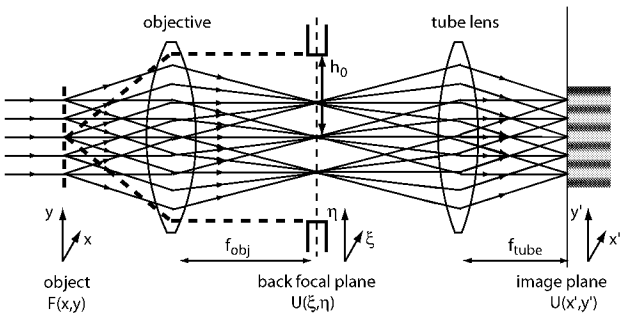

Figure 2.7: Illustration of Abbe's theory of image formation in a microscope. The incident light is diffracted at the structure of the object. This light is collected by an objective and a Fraunhofer diffraction pattern is formed in its back focal plane. Finally, the tube lens forms an image. Because the objective collects only a finite number of diffraction orders the image lacks details.

$U(x',y')$ in the image plane can be written as

$$\begin{aligned} U(x',y') &= C_2 \iint_{\mathscr{B}} d\xi\, d\eta\, U(\xi,\eta) G(\xi,\eta) e^{-\mathrm{i}\frac{2\pi}{\lambda}\left[\frac{x'}{f_{\mathrm{tube}}}\xi+\frac{y'}{f_{\mathrm{tube}}}\eta\right]} \\ &= C_1 C_2 \iint_{\mathscr{A}} dx\,dy F(x,y) \iint_{\mathscr{B}} d\xi\, d\eta\, G(\xi,\eta) e^{-\mathrm{i}\frac{2\pi}{\lambda}\left[\frac{x}{f_{\mathrm{obj}}}+\frac{x'}{f_{\mathrm{tube}}}\right]\xi} e^{-\mathrm{i}\frac{2\pi}{\lambda}\left[\frac{y}{f_{\mathrm{obj}}}+\frac{y'}{f_{\mathrm{tube}}}\right]\eta} = \\ &= C_1 C_2 \iint_{\mathscr{A}} dx\,dy F(x,y) A(x,y,x',y'), \end{aligned} \tag{2.47}$$

where the region $\mathscr{B}$ extends to infinity. Thus, image formation can be described by a convolution of two functions, one of which is the object function $F(x,y)$ and the other is the amplitude point spread function $A(x,y,x',y')$ of the imaging system,

$$A(x,y,x',y') = \iint_{\mathscr{B}} d\xi\, d\eta\, G(\xi,\eta) e^{-\mathrm{i}\frac{2\pi}{\lambda}\left[\frac{x}{f_{\mathrm{obj}}}+\frac{x'}{f_{\mathrm{tube}}}\right]\xi} e^{-\mathrm{i}\frac{2\pi}{\lambda}\left[\frac{y}{f_{\mathrm{obj}}}+\frac{y'}{f_{\mathrm{tube}}}\right]\eta}. \tag{2.48}$$

Note, that here coherent imaging is considered. In the case of incoherent illumination the result would be similar: The optical disturbance would be replaced by the intensity and the amplitude impulse response would correspond to the point spread function of the imaging system [Reynolds et al., 1989]. The amplitude point spread function of an ideal objective, i.e. $G(\xi,\eta) \equiv 1$ everywhere, is given by

$$\begin{aligned} A_{\mathrm{id}}(x,y,x',y') &= \int_{-\infty}^{\infty} d\xi\, e^{-\mathrm{i}\frac{2\pi}{\lambda}\left[\frac{x}{f_{\mathrm{obj}}}+\frac{x'}{f_{\mathrm{tube}}}\right]\xi} \int_{-\infty}^{\infty} d\eta\, e^{-\mathrm{i}\frac{2\pi}{\lambda}\left[\frac{y}{f_{\mathrm{obj}}}+\frac{y'}{f_{\mathrm{tube}}}\right]\eta} = \\ &= \left(\frac{\lambda f_{\mathrm{obj}}}{2\pi}\right)^2 \delta\left(x+\frac{f_{\mathrm{obj}}}{f_{\mathrm{tube}}}x'\right) \delta\left(y+\frac{f_{\mathrm{obj}}}{f_{\mathrm{tube}}}y'\right), \end{aligned} \tag{2.49}$$

where $\delta(x)$ denotes the Dirac delta function. For an ideal microscope hence the optical disturbance in the image plane is

$$U(x',y') = C'\lambda^2 f_{\text{obj}}^2 F(-\frac{f_{\text{obj}}}{f_{\text{tube}}}x', -\frac{f_{\text{obj}}}{f_{\text{tube}}}y'), \tag{2.50}$$

i.e. the object is magnified by $M = -f_{\text{tube}}/f_{\text{obj}}$.

2.3.2 Lateral Resolution of Microscopy

While there is no upward limit for the magnification of a microscope its resolving power is limited, i.e. above a certain magnification no further details of the object can be rendered. The resolving power of a microscope is inevitably linked to the ability of the objective to collect higher orders of the at the object diffracted light (see Fig. 2.7), i.e. with increasing aperture angle σ (see Fig. 2.8) the resolving power will also rise. The quantity describing the resolving

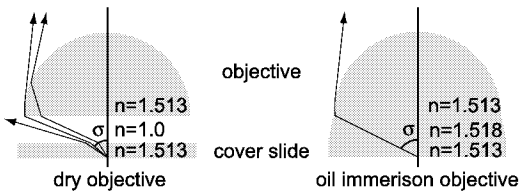

Figure 2.8: When cover slides are used oil immersion objectives own a much higher light collecting power than dry objectives. They can collect higher diffraction orders and thus exhibit a much higher resolving power.

power of a microscope is the *numerical aperture* NA

$$\text{NA} = n\sin\sigma \tag{2.51}$$

of the objective, where n is the refractive index of the object side ambient medium. Immersion objectives can typically reach a NA of 1.4, while dry objectives are limited to NA$\leq$0.99. By usage of Abbe's Sine condition [Born and Wolf, 1999], which holds for aplanatic lenses such as objectives, the numerical aperture can be related to the radius h_0 of the aperture in the exit pupil of the objective, i.e. its back focal plane:

$$h_0 = f_{\text{obj}} \cdot n\sin\sigma = f_{\text{obj}} \cdot \text{NA}. \tag{2.52}$$

Using spherical coordinates

$$\xi = r\cos\phi \qquad \eta = r\sin\phi \tag{2.53}$$

$$\frac{x}{f_{\text{obj}}} + \frac{x'}{f_{\text{tube}}} = \rho\cos\Phi \qquad \frac{y}{f_{\text{obj}}} + \frac{y'}{f_{\text{tube}}} = \rho\sin\Phi \tag{2.54}$$

the amplitude point spread function (Eq. (2.48)) of a numerical aperture limited but otherwise ideal imaging system is given by

$$A(\rho) = \int_0^{h_0} dr \int_0^{2\pi} d\phi \; r \cdot e^{-\mathrm{i}\frac{2\pi}{\lambda} r\rho\cos(\phi-\Phi)} = \frac{J_1\left(\frac{2\pi}{\lambda}h_0\rho\right)}{\frac{2\pi}{\lambda}h_0\rho}, \tag{2.55}$$

where the integral representation of the Bessel function of the first kind $J_1(r)$ has been employed [Abramowitz and Stegun, 1970]. The shape of the amplitude point spread function is shown in Fig. 2.9. The optical disturbance arising in the image plane due to a point-like structure is given by

$$U(x',y') = C_1C_2 \iint_{\mathscr{A}} dx\,dy\,\delta(x-x_0)\,\delta(y-y_0)A(x,y,x',y') = \tag{2.56}$$

$$= C_1C_2 \frac{J_1(\frac{2\pi}{\lambda}\mathrm{NA}\,\rho')}{\frac{2\pi}{\lambda}\mathrm{NA}\,\rho'} \tag{2.57}$$

with $\rho' = \sqrt{(x_o - M^{-1}x')^2 + (y_o - M^{-1}y')^2}$. The observable intensity

$$I \sim U(x',y') \cdot U^*(x',y') \sim \left(\frac{J_1(\frac{2\pi}{\lambda}\mathrm{NA}\,\rho')}{\frac{2\pi}{\lambda}\mathrm{NA}\,\rho'} \right)^2 \tag{2.58}$$

is called Airy pattern. Following the Rayleigh criterion two points in object space can still be resolved if the principal intensity maximum of one Airy pattern coincides with the first intensity minimum of the other Airy pattern. The first minimum of the Airy pattern is located at $2\pi/\lambda\,\mathrm{NA}\,\rho' = 3.83$, i.e. the resolving power Δx may be estimated as

$$\Delta x \approx \frac{1.22\lambda}{2\mathrm{NA}}. \tag{2.59}$$

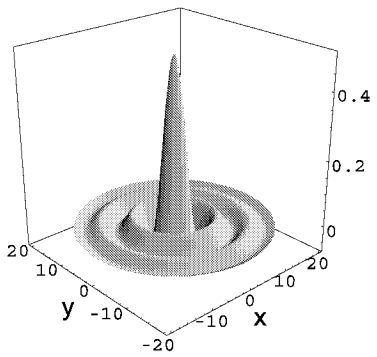

Figure 2.9: Shape of the amplitude point spread function: plot of $\frac{J_1(\sqrt{x^2+y^2})}{\sqrt{x^2+y^2}}$.

2.3.3 Oblique Illumination and Resolution

If the light incident on the object encloses an angle Θ with the optical axis the resulting lateral resolution will change. Following from Abbe's sine condition the resulting diffraction patterns

in the back focal plane of the objective will be translated by $\Delta\xi = \pm n f_{\mathrm{obj}} \sin\Theta$, where the $(+)$-sign applies for transmitted-light and the $(-)$-sign for reflected-light microscopes. In essence the objective now collects the diffracted orders asymmetrically (cf. Fig. 2.10).

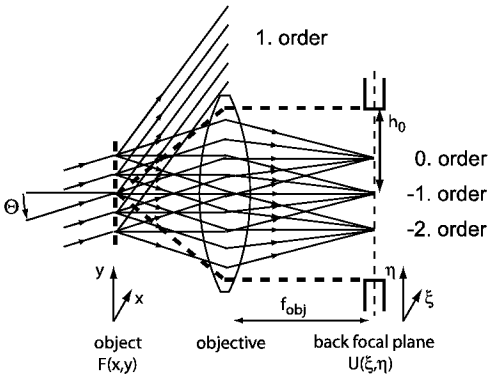

Figure 2.10: In the case of oblique illumination of the sample the diffraction orders are collected asymmetrically by the objective. For clarity the situation is shown for transmitted-light microscopy.

In the following a reflection-type microscope is assumed. If the reflectivity of the object is a step-like function oriented parallel to the plane of incidence, i.e.

$$F(x,y) = U(x) \tag{2.60}$$

with $U(x)$ denoting the Heaviside unit function, the optical disturbance $U(x',y')$ in the image plane (following from Eqs. (2.47)-(2.48)) is given by

$$U(x',y') \sim \frac{1}{2} - \frac{1}{\pi}\mathrm{Si}(k_0 y) \quad \text{with} \quad k_0 = \frac{2\pi}{\lambda}(\sqrt{\mathrm{NA}^2 - n^2\sin^2\Theta}). \tag{2.61}$$

$\mathrm{Si}(z)$ denotes the sine integral function

$$\mathrm{Si}(z) = \int_0^z \frac{\sin t}{t}\,dt,$$

similarly $\mathrm{Ci}(z)$ will denote the cosine integral function

$$\mathrm{Ci}(z) = -\int_z^\infty \frac{\cos t}{t}\,dt.$$

If the step-like structure is perpendicular to the plane of incidence, i.e.

$$F(x,y) = U(y) \tag{2.62}$$

the optical disturbance $U(x',y')$ in the image plane computes to

$$U(x',y') \sim \frac{1}{2\pi}\left(\pi - i\mathrm{Ci}(-k_1 x) + i\mathrm{Ci}(k_2 x) + \mathrm{Si}(k_1 x) - \mathrm{Si}(k_2 x)\right) \tag{2.63}$$

$$k_1 = -\frac{2\pi}{\lambda}(\mathrm{NA} - n\sin\Theta) \tag{2.64}$$

$$k_2 = \frac{2\pi}{\lambda}(\mathrm{NA} + n\sin\Theta). \tag{2.65}$$

The quantities k_1, k_2 are the minimum and maximum spatial frequencies gathered by the objective. In case they are symmetric ($k_1 = -k_2$ for $\Theta = 0°$) Eq. (2.63) simplifies to Eq. (2.61).

Figure 2.11 shows computed intensity profiles for step-like objects oriented parallel and perpendicular to the plane of incidence. While an incident angle $\Theta \neq 0°$ has only minor influence on the resolution limit for parallel structures the resolving power reduces strongly for perpendicular structures [2].

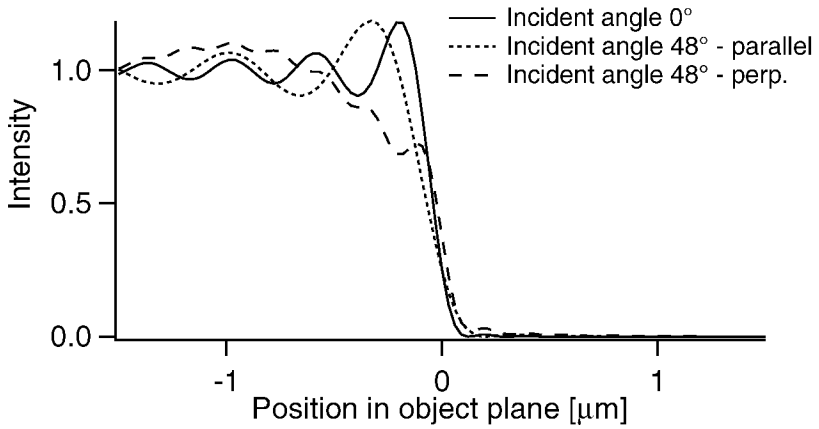

Figure 2.11: Lateral resolution: Assuming a numerical aperture of NA= 1.4 the figure shows computed intensity profiles for step-like structures oriented parallel and perpendicular to the plane of incidence. An incident angle $\Theta \neq 0°$ degrades the lateral resolution especially for structures perpendicular to the plane of incidence. $\Theta = 48°$ represents the angle of incidence measured in the cover slide. It is the typical angle of incidence chosen for ellipsometric measurements at the glass-water interface (see Section 6.2). Note that the assumed numerical aperture NA=1.4 is extremely large. Because of the paraxial assumption which entered Eq. 2.46 the presented curves are expected to capture the essential features of actual measurements while a quantitative description will be certainly not achieved.

[2] If the illuminating numerical aperture (INA) is small, oblique illumination can indeed help to resolve periodic structures, which are otherwise unresolvable. This can be also seen at the computed profiles: For the perpendicular structure the first local maximum is indeed closest to the true position ($x = 0$) of the edge. However, for a single edge the full transition region is considerably enlarged.

Chapter 3

Experimental Setup

Ellipsometry and microscopy differ in an essential point: While ellipsometry is based on reflection of parallel light rays, in microscopy cones of light rays with opening angles as large as possible are employed - not only in the imaging path, but also in the illuminating beam. This allows to further enhance the resolution. In order to combine both techniques it is thus necessary to follow a middle course and to maintain illumination of the sample with a parallel beam of light, which worsens the lateral resolution of microscopy by roughly a factor of two. On the other hand it is necessary to use higher diffraction orders for imaging in order to be able to resolve structures laterally. The intensities inherent in the higher diffraction orders, collected by the microscope objective in order to gain lateral resolution, result in spurious stray light in ellipsometric measurements and hence limit the ability to measure film thicknesses.

In this chapter the setup of the ellipsometric microscope is explained. The equation for the incident angle of the illumination is given and compared to measurements. Finally the calibration procedures for accurate determination of the azimuthal angles of polarizer, analyzer and compensator are presented.

3.1 Ellipsometric Microscopy

The setup is constructed as an inverted microscope employing epi-illumination (cf. Fig. 3.1): A parallel, polarized beam of light is focused into the back focal plane of an infinity-corrected high-power microscope objective. For measurements at the glass-water interface an oil immersion microscope objective (Plan-Apochromat 63x, NA=1.4, Zeiss) is used. At the silicon-air-interface a dry objective (MPlanApo 50x, NA=0.95, Olympus) is utilized. The parallel beam of light is created by spatially filtering monochromized light (546.1 nm) from a mercury arc lamp with a small pinhole (50 μm) and imaging it to infinity (lens 1, f_1=50 mm). The finite diameter of the pinhole introduces a small divergence of the beam ($\approx \pm 0.03^\circ$). The beam traverses a polarizer (Glan-Thompson of interferometric quality: PGT2.12 + PGT 0.1, B. Halle, Berlin) and the object is therefore illuminated with almost parallel light of well defined polar-

ization. The crucial point in the design is, that the angle of incidence can be controlled in order to maximize ellipsometric contrast. By laterally displacing the deflection mirror and thus the intermediate image of the pinhole on it, the pinhole is imaged by the lenses 3 and 4 (f_3=50mm and f_4=80 mm) into the back focal plane with a certain displacement to the optical axis of the system, cf. Fig. 3.1. This displacement causes oblique illumination of the object plane and is controlled by shifting the rigid mechanically coupled system of deflection mirror and lens 2 (f_2=60mm).

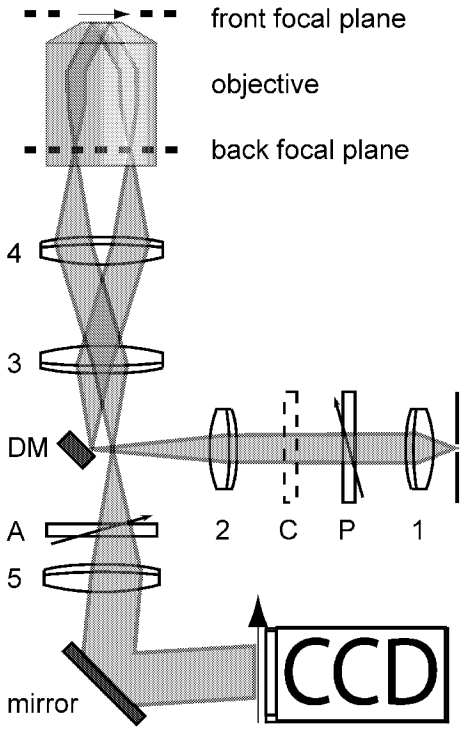

Figure 3.1: Design of the ellipsometric microscope: lenses 2-4 focus a parallel beam of light in an off-axis point of the back focal plane, resulting in oblique illumination of the object in the front focal plane. The incoming light passes a polarizer (P). The angle of incidence in the front focal plane can be controlled by horizontally shifting the rigidly coupled system of lens 2 and deflection mirror (DM). An optional compensator (C) allows illumination with elliptically polarized light. Light reflected and diffracted at the object is collected by the objective, passes a computer controlled analyzer (A) and is focused onto a CCD camera (lens 5). Lenses 3 and 4 form a telescopic system, i.e. they influence the magnification of the microscope. Here the illumination beam path is depicted, i.e. wherever a focus is indicated, the illumination pinhole is imaged. Lens 5 images the pinhole to infinity and forms an image of the object on the CCD at the same time.

At the object light is reflected and diffracted. This light is collected by the objective and imaged onto a CCD camera (C4880-50, Hamamatsu, Herrsching). Thereby the infinity space between tube lens 5 (f_5=150 mm) and objective (see Section 2.3) accommodates the optical components necessary for illumination of the object and the polarization-analysis of the reflected light. As the image is maximally blurred in this region those components create almost no image distortion. For each pixel the intensity $I(A)$ is measured as a function of the analyzer angle A. Thus each pixel of the CCD acts as a stand-alone ellipsometer in a rotating-analyzer configuration.

As commercially available microscopes do not offer enough space for the necessary modifications the setup is realized on an optical bench. All lenses are high grade achromatic doublets (Melles Griot) with anti-reflection coatings optimized for the wavelength used. Great care was used to encapsulate all optical components in order to avoid contamination with dust particles. Dust particles on the optical components are troublesome, because when the illuminating numerical aperture is small they cause the formation of Fresnel fringes. These fringes are then visible as artifacts in the resulting Ψ- and Δ-pictures. For encapsulation a tube mounting system (Linos, Göttingen) was used.

Especially tricky is the construction to achieve encapsulation of the components which are used to control the incident angle. The deflection mirror has to be adjustable with respect to five degrees of freedom (x,y,z and two angular directions). In addition it should be possible to easily read of the actual distance of the focus on the deflection mirror to the optical axis. From this distance the incident angle Θ can be computed very accurately (see Section 3.2). The unit should be completely closed, in order to prevent contamination with dust and ambient light and all the positioning units mentioned have to be integrated. Figure 3.2 shows how this was accomplished.

The polarizers are mounted in stepper motor driven goniometers (DRT 65, Owis, Staufen). A compensator (0.th order $\lambda/4$-plate, Owis, Staufen) mounted in a motorized filter wheel (Filterwheel 40, Owis) can be rotated into the optical path. All these devices are computer controlled. Ellipsometric measurements are performed by acquiring two stacks of pictures (with and without compensator), each taken typically at 18 equally spaced analyzer angles between 0° and 170°. For processing of raw data a separate image processing software was developed that computes the ellipsometric angles Ψ and Δ for each pixel of the camera. The inherent quadrant ambiguity of Δ is automatically resolved by combining the two data sets with and without the compensator. Within the software it is possible to define a model for the optical properties of the planar stratified layers of the sample and to fit the corresponding model function to either whole pictures or selected profiles of Ψ and Δ. By this procedure laterally resolved information about the refractive index n and the thickness d of any layer can be retrieved.

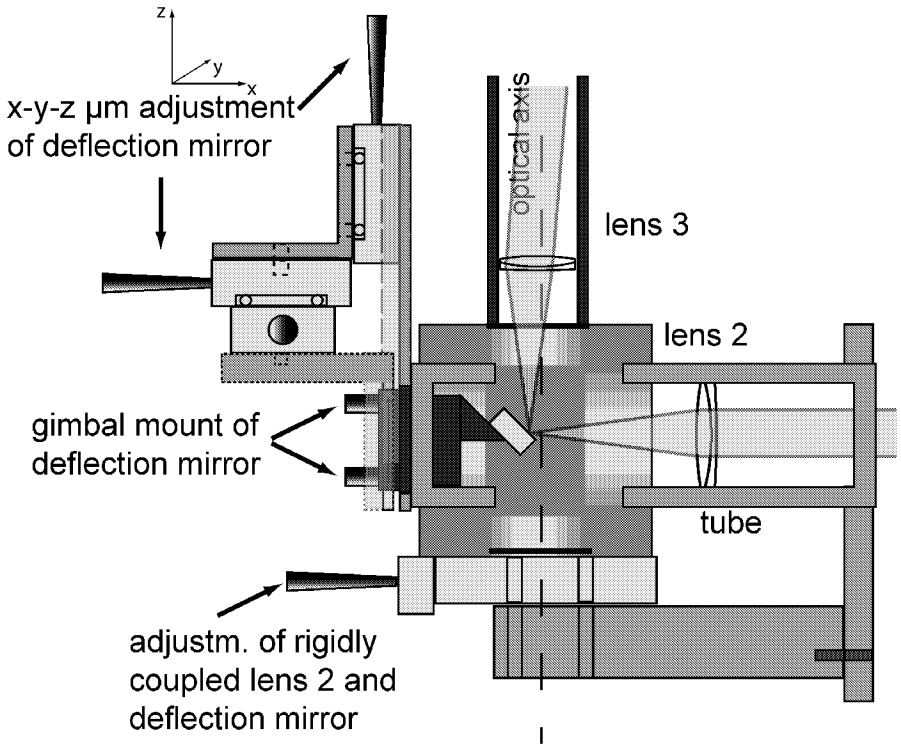

Figure 3.2: Detailed sketch of the positioning unit, which controls the incident angle and allows for encapsulation of all optical components. Lens 2 and the x-y-z positioning unit are mounted to a custom made tube. The x-y-z positioning unit holds the gimbal-mount to which the deflection mirror is mounted. The gimbal mount fits with some tolerance into the tube in order to allow for y-z-adjustment of the deflection mirror. The x-y-z positioning unit is only used to calibrate the incident angle Θ to 0°. The tube is suspended in a cube. It is rigidly connected to the cube by a μm-translation stage, which allows to shift the tube (and hence lens 2 and deflection mirror) horizontally. This enables very accurate setting of the incident angle Θ. If properly gauged, the distance of the focus (created by lens 2) to the optical axis can be read of from the translation stage. The resulting angle of incidence Θ can then be computed by use of Eq. 3.4. In reality the translation stage is not mounted to the bottom of the cube (as shown in the sketch), but to its side. To the bottom and the top of the cube the tube mounting system (Linos), to which all other lenses are mounted, is connected.

Specifications of the Microscope:

In this section the imaging properties of the microscope are summarized. The lateral extension of the epi-illuminated region in the object space can be estimated by multiplying the diameter D_{GT} of the parallel light bundle between lens 1 and 2 with the reproduction scale of the lens system 2-3-4-objective:

$$D_{IL} = \frac{-f_{\text{obj}}}{f_4} \cdot \frac{-f_3}{f_2} \cdot D_{GT}. \tag{3.1}$$

At the moment the maximum diameter D_{GT} is limited by the aperture of the Glan-Thompson polarizer ($D_{GT} = 11$ mm). As the illuminated region is larger than the field of view (see Table 3.1) in praxis this aperture is reduced with help of an iris diaphragm in order to reduce stray light. This iris diaphragm is located between polarizer and lens 1.

The lateral field of view, i.e. the region imaged onto the CCD-chip of the camera, is estimated by multiplying the size of the chip ($D_{\text{Chip}} = 13.3$ mm) with the reproduction scale of the lens system 5-3-4-objective:

$$D_{FV} = \frac{-f_{\text{obj}}}{f_4} \cdot \frac{-f_3}{f_5} \cdot D_{\text{Chip}}. \tag{3.2}$$

For the air objective the calculated result (199.5 μm) is in very good agreement agreement with the measurement at a microscope scale bar (196 μm).

	silicon substrates	glass substrates
f_{obj}	3.6 mm	2.61 mm
Magnification	66.7x	92x
Max. illuminated region	413 μm	299 μm
Field of view	196 μm	145 μm
Lateral resolution	1 μm	—
μm per pixel	0.191	0.142

Table 3.1: Specifications of the ellipsometric microscope. The given magnification includes the magnification arising from all additional lenses. Concerning glass substrates the field of view was estimated by Eq. 3.2. The value given for silicon substrates was measured with a microscope scale bar. The discussion about the lateral resolution is given in Section 6.4. Glass substrates suited for experimental determination of the lateral resolution were not available.

3.2 Controlling the Incident Angle Θ

High-power microscope objectives are highly optimized optical components which are corrected for many spherical aberational errors such as chromatic, astigmatic, comatic and field

distortion errors. As a result of the spherical aberational and coma error correction microscope objectives are aplanatic, i.e. it gives sharp images not only of axial points, but also of neighboring points of the object plane [Born and Wolf, 1999]. Aplanatic systems obey Abbe's sine condition

$$\frac{n \sin \sigma}{n' \sin \sigma'} = \frac{y'}{y} = M = const. \tag{3.3}$$

where y (y') is the height of the object (image) and σ, σ' are the angles conjugated rays enclose with the optical axis (Fig. 3.3). By use of Eq. (3.3) the relation between incident angle Θ and displacement d_M of the deflection mirror is given by

$$\sin \Theta = \frac{d_M}{n \cdot f_{\text{obj}}} \cdot \frac{f_4}{f_3} \tag{3.4}$$

where n is the refractive index of the object side medium, f_{obj} is the focal length of the microscope objective and the magnification due to different focal lengths of lenses 3 and 4 has been considered.

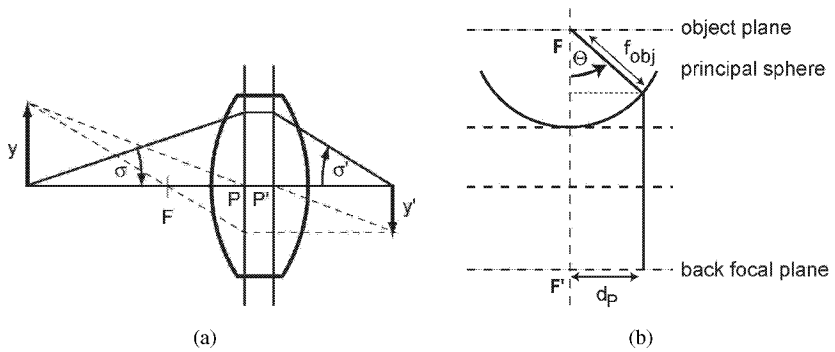

(a) (b)

Figure 3.3: (a) Geometric construction of the image: The object is located at the intersection of the ray passing through the principal points P,P' and the ray passing through the front focal point F (broken lines). In between the principal planes rays are assumed to propagate parallel to the optical axis. This construction method is only valid for paraxial rays, i.e. for rays very close to the optical axis. (b) Aplanatic lenses obey Abbe's sine condition and in the geometric construction method the principal planes must be replaced by "principal spheres"[Haferkorn, 1986]. This construction is also valid for rays far from the optical axis and the relation between incident angle Θ and distance of the pinhole image to the optical axis d_p (Eq. 3.4) can be easily identified.

Figures 3.5 and 3.6 show geometrically measured incident angles for the two microscope objectives in use. For the dry objective the incident angles were obtained by measuring the distance of the light spot on the ceiling for several deflection mirror displacements d_M. Likewise measurements were done for the oil immersion objective. The difficulty here was to measure the incident angle within the glass-substrate. This was done by measuring the lateral

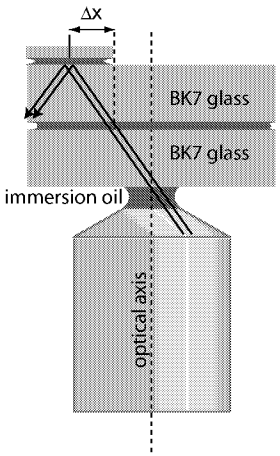

Figure 3.4: By measuring the lateral displacement introduced by a second glass plate (1 cm thick) it is possible to determine the incident angle within the glass substrate. The location of the reflex on the top side of each glass plate was determined with help of cross hairs mounted to a μm-translation stage. All glass plates were matched with immersion oil in order to avoid total internal reflection.

displacement Δx of the reflex on the topside of a 1 cm thick BK7 glass plate when a second identical glass plate was inserted (see Fig. 3.4). The material BK7 (n@546.1 nm: 1.518) was chosen, because its refractive index is very close to the refractive index of the utilized cover slides (Schott D263 glass, n@546.1 nm: 1.5255).

A comparison of the geometrically measured incident angles with the predictions of Abbe's sine condition (Fig. 3.5 and 3.6) shows an excellent agreement for both microscope objectives. The uncertainty $\Delta\Theta$ in the incident angle is approximately 0.5° for the air objective and 1° for the oil immersion objective.

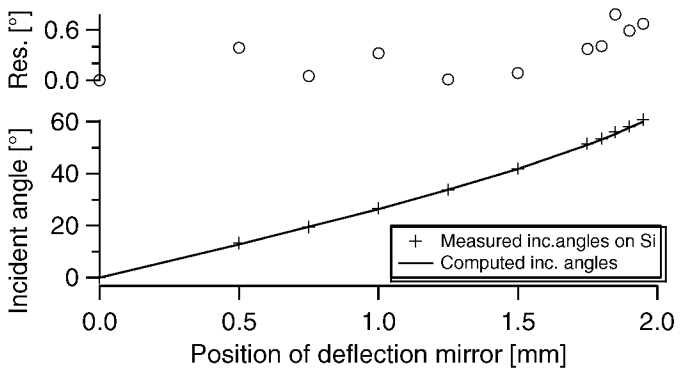

Figure 3.5: The incident angle in the object plane for the dry objective (Olympus MPlanApo 50x, NA=0.95) in dependence of the distance of the deflection mirror to the optical axis. Geometrically measured angles Θ (crosses) are in excellent agreement with the predictions from Abbe's sine condition ($f_{\mathrm{obj}} = 3.6$ mm, straight line is not a fit).

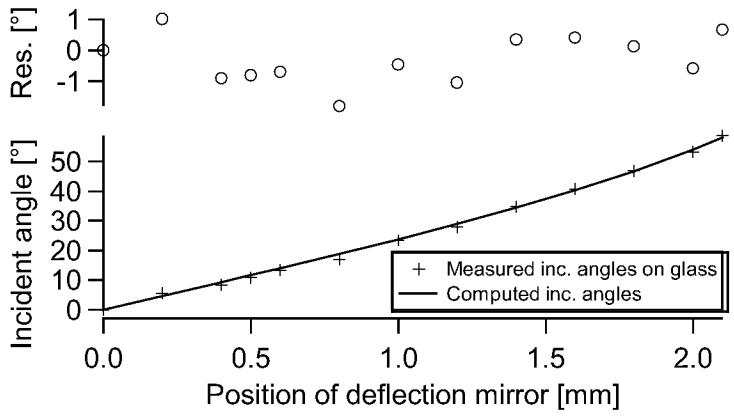

Figure 3.6: The incident angle for the oil immersion objective (Zeiss, Plan-Apochromat 63x) in dependence of the distance of the deflection mirror to the optical axis. Again, geometrically measured angles Θ are in excellent agreement with the predictions from Abbe's sine condition ($f_{\mathrm{obj}} = 2.61$ mm, $n = 1.518$, straight line is not a fit).

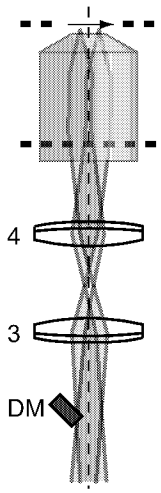

Figure 3.7: Masking of parts of the image forming light bundle due to the deflection mirror (DM). Compare with Fig. 3.1, where the light path carrying the ellipsometric information is shown.

As depicted in Fig 3.1 the deflection mirror does not collide with the part of the light bundle carrying the ellipsometric information, i.e. the primary reflex reaches the CCD camera undisturbed. But some part of the at the object diffracted light is blocked. This is schematically shown in Fig. 3.7 where the image forming ray paths are drawn. Blocking is obviously unwanted, because it leads to increased internal reflections and therefore to stray light disturbing ellipsometric measurements. In addition this blocking reduces the lateral resolution slightly. In the setup as it is realized up to now this masking unfortunately cannot be avoided: The

waist-radius r_w of the image forming ray bundle at the location of the deflection mirror is given by

$$r_w = \mathrm{NA} \cdot f_{\mathrm{obj}} \frac{f_3}{f_4}, \tag{3.5}$$

i.e. the radius $\mathrm{NA} \cdot f_{\mathrm{obj}}$ of the beam after the objective is just enlarged by the reproduction scale f_3/f_4 of the telescopic system. A comparison with Eq. (3.4) yields

$$\frac{d_M}{r_w} = \frac{n \sin\Theta}{\mathrm{NA}} = \frac{\sin\Theta}{\sin\sigma}, \tag{3.6}$$

i.e. the portion blocked by the deflection mirror depends only on the aperture angle σ of the objective and the adjusted incident angle Θ. Obviously Θ necessarily satisfies $\Theta < \sigma$ and therefore masking is inevitable.

The experiments of this thesis (Section 6.4) and experiences made with other microscopy techniques (Hoffman modulation contrast, phase contrast [Pluta, 1989b]) show that this blocking causes only a minute loss of lateral resolution. Nevertheless Section 7 presents a solution to this problem.

3.3 Calibration of the Azimuthal Angles *P*, *A* and *C*

The azimuthal angles of polarizer, analyzer and compensator have to be carefully calibrated with respect to the plane of incidence of the sample to achieve a decent ellipsometric performance of the setup. For rotating-analyzer ellipsometry several established calibration procedures can be found in the literature [Aspnes, 1974a, Kawabata, 1987, Meulen and Hien, 1973, Nijs et al., 1988]. Those procedures can readily be applied to ellipsometric microscopy. In the following two calibration procedures are described because they are complementary as they fail and succeed in opposite Δ regions. A third calibration method, based on two-zone averaging [Kawabata, 1987], was not considered because it is more prone to random errors [Collins, 1990].

The basic aim of any calibration procedure is to retrieve reliable corrections for the azimuthal angles A, P and C. In the following two different calibration procedures are described. Both yield calibrations for P and A. The calibration of the compensator azimuth C will be described in Section 3.3.4. The mathematical foundations of these calibration procedures can be derived by rewriting the measured normalized intensity at the detector (Eq. (2.22)):

$$\begin{aligned} I^{ex}(A) &= 1 + a' \cos 2A + b' \sin 2A \\ &= 1 + \sqrt{a'^2 + b'^2} \cos\left(2(A - \theta)\right) \qquad \text{with} \quad \theta = \arctan\left(b'/a'\right)/2. \end{aligned} \tag{3.7}$$

Here a', b' are the experimentally determined and error afflicted Fourier coefficients. From this form two functions can be identified which characterize the ability of the ellipsometer to measure the modulation $\sqrt{a'^2 + b'^2}$ (residual function) and the phase θ of the sinusoidal curve $I^{ex}(A)$ accurately (phase function).

3.3.1 Calibration according to Aspnes

The calibration method developed by Aspnes [Aspnes, 1974a, Collins, 1990] is most sensitive to azimuthal errors if samples with Δ values far away from 0° or 180° are used.

The Residual Function

$I^{ex}(A)$ shows maximum modulation if the wave emerging from the sample is linearly polarized, i.e. $a'^2 + b'^2 = 1$ (Eq. (2.27) for $\Delta = 0^\circ, 180^\circ$). The deviation from this 100% modulation can be characterized by the **residual function**:

$$R(P) = 1 - \eta^{-2}(a'^2 + b'^2). \tag{3.8}$$

The instrumental frequency attenuation factor η describes the attenuation of the 2ω frequency components ($a' \cdot I_0$, $b' \cdot I_0$) with respect to the dc component I_0 due to electrical circuit deficiencies. As the Fourier analysis in this setup is performed by a computer η is expected to fulfill $\eta = 1$.

The basic idea behind this calibration method can be described as follows: If the incident light is linearly polarized and exactly aligned parallel (or perpendicular) to its plane of incidence the reflected light will be linear polarized, too. Note that this holds for any isotropic sample. At this position of the polarizer $R(P) = 0$. Only if there is a small misalignment of polarization orientation and plane of incidence, can the phase shift Δ of the sample introduce an ellipticity in the reflected light. This causes an increase of the residual function $R(P) > 0$. Thus a' and b' are determined at several polarizer settings P and the residual function is plotted. At its minimum the polarizer axis coincides with the plane of incidence (cf. Fig. 3.8).

Let us cast these considerations in formulas: The experimentally observed a' and b' can be computed by repeating the calculations Eq. (2.20) - Eq. (2.25) in the presence of azimuth-angle errors δA and δP, i.e. the electric field strength at the detector is given by

$$\mathbf{E}_{Det} = \mathbf{R}_{-(A'-\delta A)}\, \mathbf{T_A}\, \mathbf{R}_{A'-\delta A}\, \mathbf{T_S}\, \mathbf{R}_{-(P'-\delta P)} \begin{pmatrix} 1 \\ 0 \end{pmatrix} E_0. \tag{3.9}$$

In the following P and A denote the true polarizer azimuth angles while $P' = P + \delta P$ and $A' = A + \delta A$ denote uncalibrated polarizer azimuths. The residual function is thus

$$R(P') = (1 - \eta^{-2}) + \frac{4\sin^2\Delta \tan^2(P' - \delta P)\tan^2\Psi}{\eta^2(\tan^2(P' - \delta P) + \tan^2\Psi)^2}. \tag{3.10}$$

A first order expansion in $P = P' - \delta P$ yields

$$\begin{aligned} R(P') &= 1 - (a'^2 + b'^2) \\ &\approx \begin{cases} (1 - \frac{1}{\eta^2}) + \frac{4\sin^2\Delta}{\eta^2\tan^2\Psi}\,(P' - \delta P)^2 + \ldots & \text{for} \quad (P \approx 0) \\ (1 - \frac{1}{\eta^2}) + \frac{4\sin^2\Delta\tan^2\Psi}{\eta^2}\,(P' - \delta P - \frac{\pi}{2})^2 + \ldots & \text{for} \quad (P \approx \pi/2). \end{cases} \end{aligned} \tag{3.11}$$

Thus calibration of the azimuthal polarizer angle P (with respect to the plane of incidence at the sample!) is performed by measuring a' and b' at several P' around the estimated direction of the transmission axis of the polarizer and fitting a parabolic function to the computed residual function (see Fig. 3.8 or 3.9). The location of the minimum provides δP. The instrumental attenuation factor η is then determined from the minimum value of the best fitting function. For optimum sensitivity to δP the curvature of the residual function must be maximized by choosing an adequate calibration sample. Therefore samples with expected Δ near 0° and 180° must be avoided.

The Phase Function

The **phase function** (compare with Eq. (3.7)) is defined as

$$\theta(P') = \arctan(b'/a')/2. \tag{3.12}$$

Analog to Eq. (3.10) an analytical expression for $\theta(P')$ in the presence of azimuth-angle errors can be derived. After a first order expansion in both, δA and P, this results in:

$$\begin{aligned} \theta(P') &= \arctan(b'/a')/2 \\ &\approx \begin{cases} \delta A + \frac{\cos\Delta}{\tan\Psi}\cdot(P'-\delta P)+\ldots & \text{for} \quad P \approx 0 \\ \delta A + \cos\Delta\tan\Psi\cdot(P'-\delta P-\frac{\pi}{2})+\ldots & \text{for} \quad P \approx \pi/2 \end{cases} . \end{aligned} \tag{3.13}$$

Thus, the azimuth-angle error δA can be found by evaluating the phase function at the minimum $P' = \delta P$ found in the residual function calibration (cf. Fig. 3.8).

3.3.2 Calibration according to de Nijs

The calibration method described by de Nijs [Collins, 1990, Nijs et al., 1988] is superior to the residual function calibration method if calibration samples with Δ values near 0° or 180° are used.

Phase Difference Function:

The **phase difference function** is defined as

$$\Phi(P') = \theta(P') - \theta(P'+\pi/2) \tag{3.14}$$

A first order expansion of $\Phi(P')$ yields:

$$\Phi(P') \approx \frac{2\cos\Delta}{\tan 2\Psi}\cdot(P'-\delta P). \tag{3.15}$$

Thus calibration of the azimuthal polarizer angle (with respect to the plane of incidence at the sample!) is performed by subtracting the phase functions for the different P-zones at several

azimuthal positions P' of the polarizer and fitting a linear function to the data points. δP can be read of as the P-axis intercept of the fitting function. The procedure is most accurate for large slopes of the linear relationship, i.e. for δ values near 0° or 180°. The azimuthal angle correction of the analyzer δA is retrieved like in the previous calibration method from the phase function $\Theta(P')$.

Figure 3.8 presents a sketch of both calibration schemes.

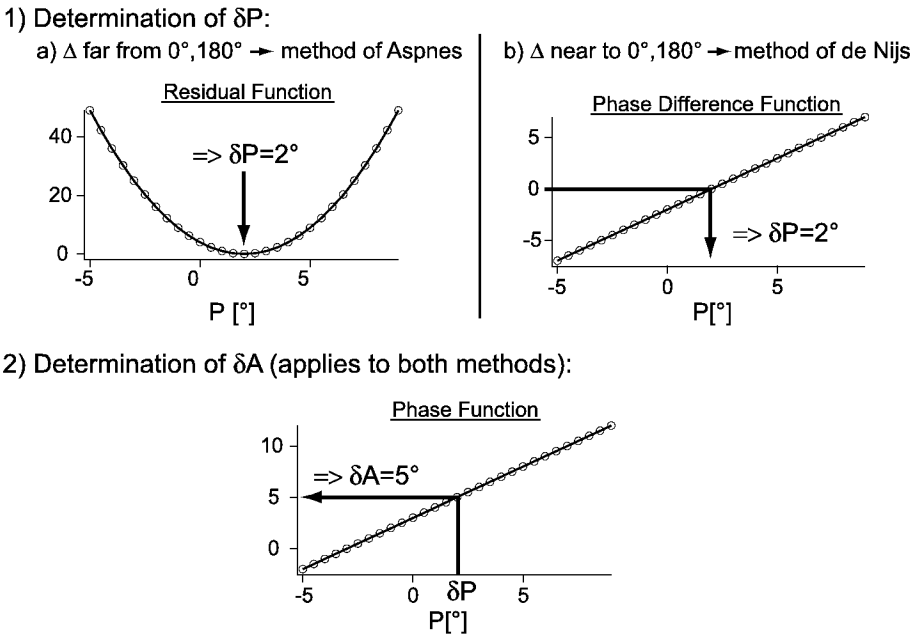

Figure 3.8: The two calibration schemes: Depending on the sample-value of Δ δP has to be extracted from either the residual function or from the phase difference function. Once δP is known δA can be obtained from the phase function.

3.3.3 Influence of Component Optical Activity on the Calibration Methods

Imperfect polarizers and analyzers not only influence the measured Ψ and Δ values (see Section 4.5) but may also have an influence on the calibration procedures described above. The most common imperfection is, that the polarizing components pass light with an **residual ellipticity**, i.e. the from the component emerging Jones vector is of the form $\begin{pmatrix} 1 \\ i\Gamma_{P,A} \end{pmatrix}$ instead of $\begin{pmatrix} 1 \\ 0 \end{pmatrix}$. This residual ellipticity affects both calibration procedures described above [Collins,

1990]. If δP_1 and δA_1 represent near $P \approx 0°$ experimentally determined azimuthal correction values found in the residual function calibration those values have to be corrected by

$$\delta P_s = \delta P_1 - \frac{\Gamma_A \tan\Psi' + \Gamma_P \cos\Delta'}{\sin\Delta'} \tag{3.16}$$

$$\delta A_s = \delta A_1 - \frac{\Gamma_P \cot\Psi' + \Gamma_A \cos\Delta'}{\sin\Delta'}, \tag{3.17}$$

where Ψ' and Δ' denote zero order approximations (without optical activity corrections) [Aspnes, 1974a, Collins, 1990]. Note that the corrections diverge for Δ' close to 0° or 180°. The effect of residual ellipticity on the polarizer calibration angles retrieved from the zone-difference phase function method is given to first order by

$$\delta P_s = \delta P_0 + \Gamma_P \frac{\tan\Delta'}{\cos 2\Psi'} \tag{3.18}$$

$$\delta A_s = \delta A_0 + \Gamma_P \frac{\sin\Delta'}{\tan 2\Psi'}. \tag{3.19}$$

Here δP_0 is the P'-axis intercept of the phase difference function and δA_0 is the phase function evaluated at δP_0.

An upper estimate for the residual ellipticity Γ of a polarizer can be computed from the extinction ratio k given by the manufacturer:

$$|\Gamma| \leq \frac{1}{\sqrt{2}}\sqrt{k} \tag{3.20}$$

These corrections to the Jones matrices of the polarizers are small for the employed components (Glan-Thompson: $k < 10^{-5}$, sheet polarizer: $k < 10^{-4}$). Nevertheless, even if only appropriate combinations of samples and calibration methods are used, the azimuthal corrections (Eq. (3.16)-(3.19)) can amount up to 0.5°. References [Aspnes, 1974a] and [Radman and Cahan, 1981] describe how to determine $\Gamma_{P,A}$ from the residual function calibration method: If δP_1 and $\delta P_2 + \pi/2$ are the location of the minima of $R(P)$ near $P \approx 0°$ and $P \approx \pi/2$, respectively, and $\delta A_1, \delta A_2$ are the corresponding values of the phase function, $\Gamma_{P,A}$ can be computed according to

$$\Gamma_P = \left[(\delta P_1 - \delta P_2)\cos\Delta' - (\delta A_1 - \delta A_2)/\sin 2\Psi'\right]/D_1 \tag{3.21}$$

$$\Gamma_A = \left[(\delta A_1 - \delta A_2)\cos\Delta' - (\delta P_1 - \delta P_2)/\sin 2\Psi'\right]/D_1 \tag{3.22}$$

$$D_1 = 2(\cos^2\Delta' - \sin^{-2} 2\Psi')/\sin\Delta'. \tag{3.23}$$

3.3.4 Calibration Results

It was possible to apply the methods described above to ellipsometric microscopy by measuring laterally homogeneous samples and computing the Fourier coefficients a and b from laterally averaged intensities ($\sim 25 \times 25$ μm). Due to the lack of structure it seems difficult

to focus the region of interest on homogeneous samples correctly. In praxis the surface of the sample is covered sparsely with small dust particles, allowing for accurate focusing.

Table 3.2 and Fig. 3.9 summarize the results of a typical calibration. Three different samples were chosen: a bare gold substrate optimally suited for residual function calibration, a bare silicon substrate optimal for the phase difference calibration and a silicon substrate covered with 40 nm MgF_2 which allows for both calibrations. The preparation of the samples is described in Section 5.1. After correcting for the influence of the optical activities $\Gamma_{P,A}$ average values of $P_s = 0.34 \pm 0.16^\circ$ and $A_s = -0.04 \pm 0.11^\circ$ were found (see Table 3.2).

In the setup the azimuthal angle of the compensator is not automated. Therefore it is not possible to apply likewise calibration procedures. One of the principal axes of the compensator was found by placing the already calibrated polarizer (oriented at $P = 45^\circ$), compensator, analyzer and detector in line and adjusting the azimuthal angle of the compensator in order to minimize variations in $I(A)$. In the manually found minimum position the orientation of the axes of the compensator should enclose an angle of 45° with the transmission axis of the polarizer. This kind of calibration procedure minimizes $|\delta P - \delta C|$ and thus it is a good assumption that when all components are reassembled to the ellipsometric microscope the azimuthal errors with respect to the plane of incidence of the sample satisfy $\delta C \approx \delta P \approx 0^\circ$.

The adaption of well-established ellipsometric calibration procedures to ellipsometric microscopy allowed for very precise calibration of the azimuthal angles P and A. In addition, these methods ensure calibration with respect to the plane of incidence. This is extremely important in order to avoid systematic errors. From the results of Table 3.2 residual azimuth errors are estimated to be smaller than 0.2°. In Section 4.2 a method for systematic cancellation of these residual errors will be presented.

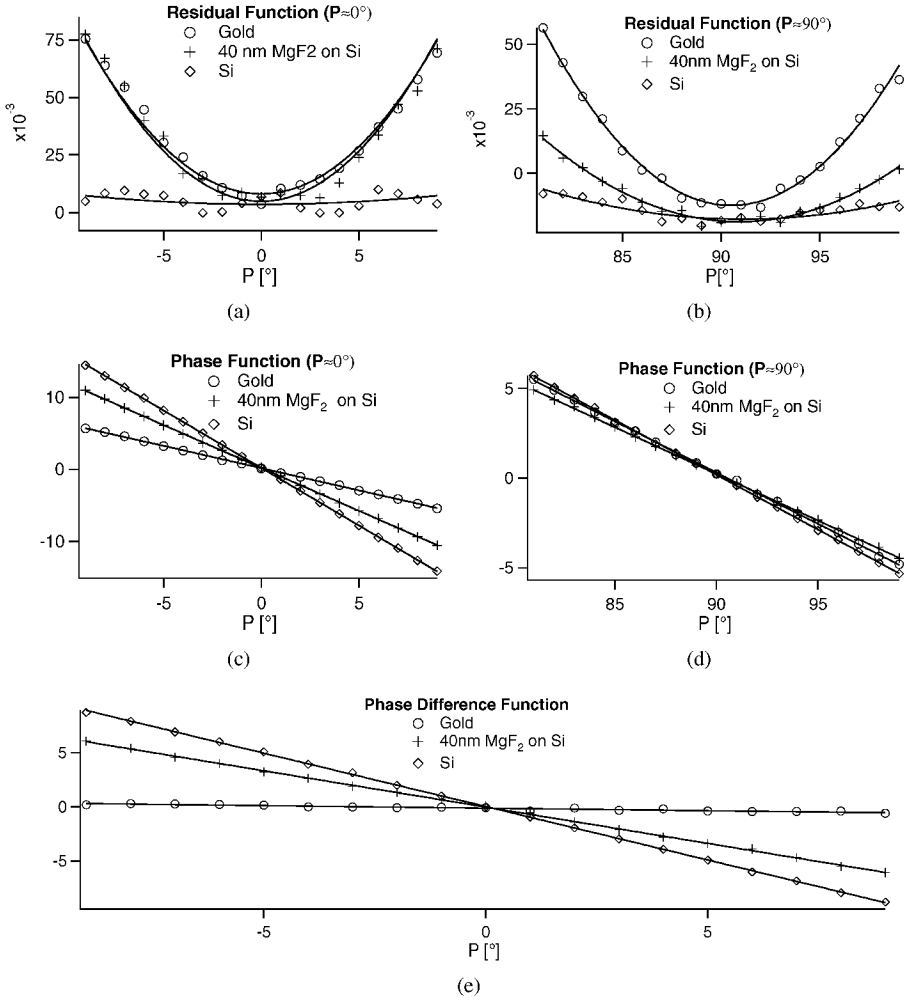

Figure 3.9: Plot of the residual (a), (b), the phase (c), (d) and the phase difference function (e) as measured with the ellipsometric microscope for 3 different samples: gold substrate, 40 nm MgF_2 on silicon and a bare silicon substrate. Note that the residue calibration fails for the bare silicon substrate while for the gold substrate the phase difference calibration is less suitable. The minimum value of the residual function is not the same for all samples, i.e. the instrumental attenuation factor η cannot be determined accurately. This is probably not due to the use of different samples, but due to different camera (detector) settings such as exposure time.

		Sample		
Method	Quantity	40 nm MgF_2	Gold	bare Si
Res. Func.	η_1	1.0024	1.004	1.0018
Res. Func.	η_2	0.9908	0.994	0.9913
Res. Func.	δP_1 [°]	0.354	0.267	(1.18)
Res. Func.	δP_2 [°]	0.919	0.511	(1.11)
Res. Func.	δA_1 [°]	-0.214	0.015	(-1.68)
Res. Func.	δA_2 [°]	-0.247	0.010	(-0.50)
Phase Dif. Func.	δP_0 [°]	-0.035	(-2.68)	0.024
Phase Dif. Func.	δA_0 [°]	0.249	(1.83)	0.164
Res. Func.	$\Gamma_P[\cdot 10^{-3}]$	-4.4	-1.5	-5.1
Res. Func.	$\Gamma_A[\cdot 10^{-3}]$	-6.0	-2.6	-4.5
	Ψ [°]	34.4	44.1	31.9
	Δ [°]	144.5	126.8	173.0
Res. Func.	corrected δP_s [°]	0.41 | 0.45	0.38 | 0.29	(0.10 | -7.87)
Phase Dif. Func.	corrected δP_s [°]	0.46 | 0.53	(1.30 | -0.32)	0.11 | 0.12
Res. Func.	corrected δA_s [°]	-0.06 | -0.11	0.02 | 0.06	(0.10 | 12.84)
Phase Dif. Func.	corrected δA_s [°]	-0.13 | -0.20	(-0.55 | 0.42)	0.09 | 0.07

Table 3.2: Calibration results for 3 different samples: 40 nm MgF_2 deposited on a silicon substrate, a gold substrate and a bare silicon substrate. Ψ and Δ values were computed from the curvature and slope of the residual and phase function. $\delta P_{1,2}$ and $\delta A_{1,2}$ were determined from the residual function measurements at $P' \approx 0°$, $P' \approx 90°$ respectively. δP_0 and δA_0 were obtained from measuring the phase difference function. The residual ellipticities Γ_P and Γ_A were determined as described in Section 3.3.3. Using those values the azimuthal angle offsets were corrected according to the respective calibration procedure (see Section 3.3.3). This yielded δP_s and δA_s. In order to give an estimate about the sensitivity on the number of data points utilized for determination of the presented values, the analysis was repeated utilizing only the subrange $P \in [-5°, 5°]$ of the measured calibration function values (data given to the right of the "|"-symbol in the last four rows). The good agreement shows, that the calibration procedures are very stable, if the appropriate procedures are utilized. Bracketed values indicate that the values are not trustworthy, because the calibration method is not appropriate for this sample. Only for the MgF_2 sample both calibration procedures are applicable.

Chapter 4

Error Analysis

The fundamental quantities measured in the rotating-analyzer setup are the Fourier coefficients a and b. From these quantities Ψ and Δ are computed by formulas which exhibit singularities (cf. Eq. 2.26, 2.27). Because of this it is necessary to consider the propagation of errors δa and δb to errors in Ψ and Δ:

$$\begin{aligned}
\delta\Psi &= \frac{\partial\Psi}{\partial\tan\Psi}\frac{\partial\tan\Psi}{\partial a}\,\delta a = \cos^2\Psi\,\frac{\tan^2 P}{(a-1)^2\tan\Psi}\,\delta a = \\
&= \frac{1}{4}\frac{\cos^2\Psi}{\tan\Psi}\left(\frac{\tan^2 P+\tan^2\Psi}{\tan P}\right)^2\delta a \qquad (4.1)\\
\delta\Delta &= \sqrt{\left(\frac{\partial\Delta}{\partial a}\delta a\right)^2+\left(\frac{\partial\Delta}{\partial b}\delta b\right)^2} = \sqrt{\frac{\delta b^2+a^2\cos\Delta^2\delta a^2}{1-a^2-b^2}} = \\
&= \sqrt{\frac{(\tan^2 P+\tan^2\Psi)^2\;\delta b^2+\frac{1}{4}(\frac{\tan^3 P}{\tan\Psi}-\frac{\tan^3\Psi}{\tan P})\cos^2\Delta\;\delta a^2}{4\;\tan^2 P\;\tan^2\Psi\;\sin^2\Delta}} \qquad (4.2)
\end{aligned}$$

or similarly for measurements with compensator

$$\begin{aligned}
\delta\Psi^c &= \frac{\partial\Psi}{\partial\tan\Psi}\frac{\partial\tan\Psi}{\partial a^c}\,\delta a^c = \cos^2\Psi\,\frac{\tan^2 P}{(a^c-1)^2\tan\Psi}\,\delta a^c = \\
&= \frac{1}{4}\frac{\cos^2\Psi}{\tan\Psi}\left(\frac{\tan^2 P+\tan^2\Psi}{\tan P}\right)^2\delta a^c \qquad (4.3)\\
\delta\Delta^c &= \sqrt{\left(\frac{\partial\Delta}{\partial a^c}\delta a^c\right)^2+\left(\frac{\partial\Delta}{\partial b^c}\delta b^c\right)^2} = \sqrt{\frac{\delta b^{c2}+a^{c2}\sin\Delta^2\delta a^{c2}}{1-a^{c2}-b^{c2}}} = \\
&= \sqrt{\frac{(\tan^2 P+\tan^2\Psi)^2\;\delta b^{c2}+\frac{1}{4}(\frac{\tan^3 P}{\tan\Psi}-\frac{\tan^3\Psi}{\tan P})\sin^2\Delta\;\delta a^{c2}}{4\;\tan^2 P\;\tan^2\Psi\;\cos^2\Delta}}. \qquad (4.4)
\end{aligned}$$

In the latter equation it was assumed, that the slow axis of the compensator encloses an angle of 90° with the plane of incidence, i.e. $C = 90^\circ$. All measurements were performed at this

setting angle. Because in this setting the compensator just adds a phase shift of 90° to Δ of the sample it does not affect Ψ (compare Eq. (2.26) and (2.39)) and error propagation for Ψ and Ψ^c are identical. For the same reason the error propagation of Δ^c can be obtained by replacing Δ in Eq. (4.2) with $\Delta + 90°$.

Apart from the properties of the sample (Ψ, Δ) the error propagations are also influenced by the setting of the polarizer angle P. Setting the derivate with respect to P of Eq. (4.1)-(4.4) equal to zero and solving for P yields for each equation the same **optimum polarizer angle** which obeys the surprisingly simple equation [Aspnes, 1974b, Collins, 1990]

$$|P_{opt}| = \Psi. \tag{4.5}$$

At this polarizer setting all error influences are minimized and it is recommended to perform ellipsometric measurements at this angle. At this angle Eq. (4.1)-(4.4) simplify considerably:

$$\delta\Psi = \frac{1}{2}\sin(2\Psi)\delta a \quad , \quad \delta\Delta = -\frac{\mathrm{sgn}(P_{opt})}{|\sin\Delta|}\,\delta b \tag{4.6}$$

$$\delta\Psi^c = \frac{1}{2}\sin(2\Psi)\delta a^c \quad , \quad \delta\Delta^c = -\frac{\mathrm{sgn}(\cos P_{opt})}{|\cos\Delta|}\,\delta b^c. \tag{4.7}$$

The function $\mathrm{sgn}(x)$ returns the sign of x. Note that errors $\delta\Delta$ diverge for samples with $\Delta \approx 0°, 180°$ while errors $\delta\Delta^c$ diverge for samples with $\Delta \approx 90°, 270°$. Hence the compensator is not only necessary for the mutual quadrant correction (see Section 2.2.2). It is also necessary for accurate full-domain Δ-determination.

In the following various sources for systematic errors and their influence on the Fourier coefficients a, b are going to be discussed.

4.1 Influence of Stray Light

In the presence of completely depolarized stray light, I_S, the at the detector measured intensity $I(A)$ has to be extended to

$$I_D = I_0(1 + a\cos(2A) + b\sin(2A)) + I_S. \tag{4.8}$$

Rewriting this to

$$I_D = I_0(1+x)\cdot(1 + \frac{a}{1+x}\cos(2A) + \frac{b}{1+x}\sin(2A)) \quad \text{with} \quad x = \frac{I_S}{I_0} \tag{4.9}$$

reveals the effect of unpolarized stray light: The average incident intensity I_0 seems increased and the Fourier coefficients a' and b' appear to be damped:

$$a' = a/(1+x) \tag{4.10}$$

$$b' = b/(1+x) \tag{4.11}$$

Employing Eqs. (2.26) and (2.27) the erroneous $\Psi' = \Psi + \delta\Psi$ and $\Delta' = \Delta + \delta\Delta$ can be computed. When measuring at $P = \Psi$ the errors are given by (cf. Fig. 4.1, 4.2)

$$\delta\Psi = \delta\Psi^c = 0 \tag{4.12}$$

$$\delta\Delta = \cos^{-1}\left(\frac{\cos\Delta}{1+x}\right) - \Delta \quad , \quad \delta\Delta^c = \sin^{-1}\left(\frac{\sin\Delta}{1+x}\right) - \Delta. \tag{4.13}$$

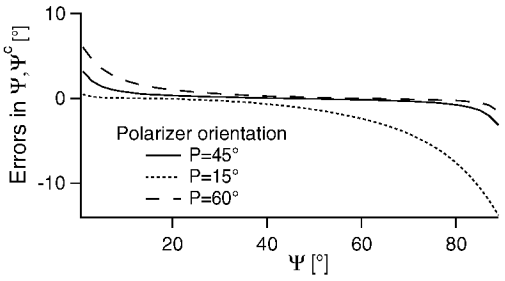

Figure 4.1: Errors in Ψ due to unpolarized stray light (x=1%). At $P = \Psi$ stray light does not affect Ψ.

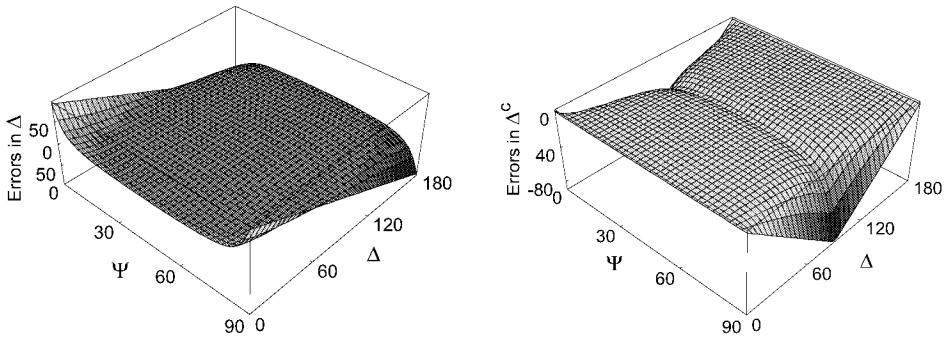

Figure 4.2: Errors in Δ and Δ^c due to unpolarized stray light (x=1%). The polarizer is set to $P = 45°$.

4.2 Errors due to Azimuthal Angle (P,A,C) Misalignment

Section 3.3 described calibration methods by which experimental errors δP, δA and δC can be minimized. Due to other systematic errors, e.g. polarizer imperfections, the accuracy of these calibration methods is limited. Studying systematic error propagation reveals, that there is a way to eliminate errors due to δP, δA and δC to first order.

The general framework for the derivation of these systematic errors was already explained in Section 2.2.2: First model the electric field strength $\mathbf{E}_{Det}$ incident on the detector (Eq. (2.20),

(2.28) respectively). In order to account for azimuthal errors A,P and C are replaced by $A-\delta A$, $P-\delta$P and $C-\delta C$. Computing the intensity incident on the detector

$$I_{Det} = \mathbf{E}_{Det}^{\dagger}\mathbf{E}_{Det} \tag{4.14}$$

the erroneous Fourier coefficients a' and b' are determined by Fourier analysis:

$$I_0 = \frac{1}{\pi}\int_0^{\pi} dA \cdot I_{Det}(A) \tag{4.15}$$

$$a' = \frac{2}{\pi}\int_0^{\pi} dA \cdot \frac{I_{Det}(A)}{I_0}\cos(2A) \tag{4.16}$$

$$b' = \frac{2}{\pi}\int_0^{\pi} dA \cdot \frac{I_{Det}(A)}{I_0}\sin(2A). \tag{4.17}$$

Employing Eq. (2.26) and Eq. (2.27) the erroneous $\Psi' = \Psi + \delta\Psi$ and $\Delta' = \Delta + \delta\Delta$ can be computed.

Errors due to Azimuthal Analyzer Angle A Misalignment

If the azimuthal angle of the analyzer deviates by δA from the true one, the resulting Fourier coefficients a' and b' are connected with the true coefficients a and b by a rotation matrix

$$\begin{pmatrix} a' \\ b' \end{pmatrix} = \begin{pmatrix} \cos(2\delta A) & -\sin(2\delta A) \\ \sin(2\delta A) & \cos(2\delta A) \end{pmatrix} \begin{pmatrix} a \\ b \end{pmatrix}. \tag{4.18}$$

The influence of δA on Ψ and Δ are up to first order:

$$\delta\Psi = -\cos\Delta \frac{1-\cos(2P)\cos(2\Psi)}{\sin(2P)}\,\delta A + \ldots \tag{4.19}$$

$$\delta\Delta = -|\sin\Delta| \frac{2(\cos(2\Psi)-\cos(2P))}{\sin(2P)\,\sin(2\Psi)}\,\delta A + \ldots \tag{4.20}$$

Note that
- the sign for the Δ-correction is only valid for non-quadrant corrected Δ-values.
- the contributions due to δA are asymmetric in P.

When measuring at $P = \Psi$ the errors are given by

$$\delta\Psi = -\mathrm{sgn}(P)\cos\Delta\sin 2\Psi\,\delta A + \ldots \tag{4.21}$$

$$\delta\Delta = 0 + \mathcal{O}(\delta A^2) + \ldots. \tag{4.22}$$

Errors due to Azimuthal Polarizer Angle P Misalignment

An by δP erroneous polarizer azimuth P affects the ellipsometric angles by

$$\Psi' = \Psi + \frac{\sin 2\Psi}{\sin 2P}\delta P + \ldots \tag{4.23}$$

$$\Delta' = \Delta \tag{4.24}$$

Note that
- in spite of the erroneous polarizer azimuth Δ is correctly determined.
- the contribution due to δP is asymmetric in P.

When measuring at $P = \Psi$ the errors are given by

$$\delta\Psi = \mathrm{sgn}(P)\ \delta P + \ldots \tag{4.25}$$

$$\delta\Delta = 0. \tag{4.26}$$

Errors due to Azimuthal Compensator Angle C Misalignment

$$\Psi' = \Psi - \frac{\sin 2\Psi}{\sin 2P}\delta C + \ldots \tag{4.27}$$

$$\Delta' = \Delta + 2\frac{\mathrm{sign}(\cos\Delta)}{\tan 2P}\delta C \quad (C = 90^\circ) \tag{4.28}$$

Note that
- the sign for the Δ-correction is only valid for non-quadrant corrected Δ-values.
- the contributions due to δC are asymmetric in P.

When measuring at $P = \Psi$

$$\Psi' = \Psi - \mathrm{sgn}(P)\delta C \tag{4.29}$$

$$\Delta' = \Delta + 2\,\mathrm{sgn}(P)\frac{\mathrm{sign}(\cos\Delta)}{\tan 2\Psi}\ \delta C \quad (C = 90^\circ) \tag{4.30}$$

Elimination of Systematic Azimuth Errors by Zone Averaging

The first-order analysis of the last section yielded that corrections to Ψ and Δ due to azimuth-angle errors are all odd functions of P. Thus, by averaging quantities measured in different P-zones, azimuthal angle errors can be eliminated in first order without determining them explicitly:

$$\Psi = \frac{\Psi'(P) + \Psi'(-P)}{2} + \mathcal{O}(\delta P^2, \delta A^2, \delta C^2) \tag{4.31}$$

$$\Delta = \frac{\Delta'(P) + \Delta'(-P)}{2} + \mathcal{O}(\delta A^2, \delta C^2). \tag{4.32}$$

This systematic error reduction method is known as *zone averaging* [Collins, 1990, Nijs and Silfhout, 1988] and is of course only sensible if the higher order errors due to $\delta A, \delta P$ and δC are negligible. This is in general the case if the polarizer angle satisfies $10^\circ \leq P \leq 80^\circ$ and $10^\circ \leq \Psi \leq 80^\circ$ [Nijs and Silfhout, 1988].

4.3 Detector Nonlinearity

A slight nonlinearity introduced by the CCD-camera changes the observed spectrum of the measured intensities $I(A)$ (Eq. (2.22)). The apparent Fourier coefficients a' and b' are affected by the generation of higher order harmonics and therefore the computed Ψ and Δ are erroneous [Ilsin et al., 1991, Luttmann et al., 1998, Nguyen et al., 1991]. Modeling detector nonlinearities by expressing the detector output by

$$I_{\text{CCD}}(I_{Det}) \sim I_{Det} + \sum_{n=2}^{\infty} k_n I_{Det}^n \approx I_{Det} + k I_{Det}^2 \tag{4.33}$$

and computing a', b'

$$I_0 = \frac{1}{\pi}\int_0^\pi dA \cdot I_{\text{CCD}}(I_{Det}) \tag{4.34}$$

$$a' = \frac{2}{\pi}\int_0^\pi dA \cdot \frac{I_{\text{CCD}}(I_{Det})}{I_0}\cos(2A) = \frac{2\,(a+2ak)}{2+(2+a^2+b^2)\,k} \tag{4.35}$$

$$b' = \frac{2}{\pi}\int_0^\pi dA \cdot \frac{I_{\text{CCD}}(I_{Det})}{I_0}\sin(2A) = \frac{2\,(b+2bk)}{2+(2+a^2+b^2)\,k} \tag{4.36}$$

yields the relation between true and apparent Fourier coefficients. If the strength of the nonlinear contribution k is known the inverse of Eq. (4.35) and (4.36) can be used in order to correct for detector nonlinearities. In general it is advisable to correct this error directly on the intensity level.

In order to give an estimate about the linearity of the CCD camera a sample with large homogeneous structures was focused with the ellipsometric microscope. The acquisition time of the CCD camera was chosen such that its full dynamic range was used. The intensities incident on the CCD camera were then varied by insertion of neutral density filters. The measured intensities were obtained by averaging over laterally homogeneous regions (ca 25×25 μm^2). The expected incident intensities were computed from the nominal optical densities of the filters and scaled to pixel count units. Alternatively, the pixel count due to the incident intensity was varied by reducing the acquisition time of the CCD.

Figure 4.3 shows the measured linearity of the utilized CCD camera. Both curves, obtained by insertion of neutral density filters and by varying the acquisition time, show good agreement, but exhibit a small deviation from linear behavior. The good agreement between both methods proves an excellent linearity in exposure time of the CCD-camera. Normalizing the

measured intensity pixel counts to a maximum value of one and fitting Eq. (4.33) to incident and measured intensities yields a strength $k = 0.128$ of the nonlinearity.

Note that detector nonlinearities generate also an offset to the minimum of the residual function (see Section 3.3.1):

$$R(P) = 1 - \eta^{-2}(a'^2 + b'^2) \overset{a^2+b^2=1}{=} -\frac{k\,(4+7k)}{(2+3k)^2}. \tag{4.37}$$

Thus, the strength k of the nonlinearity can also be estimated by use of the residual function calibration. Fig. 3.9 shows already linearized results, but estimates from non-linearized measurements yield - in good agreement with the directly measured nonlinearity - a value of $k \approx 0.14$.

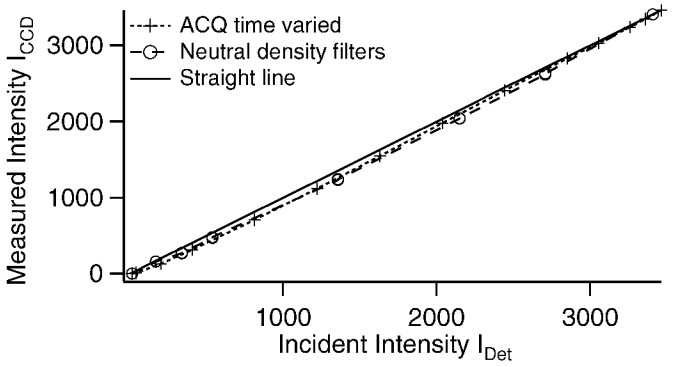

Figure 4.3: Linearity of the CCD in use (C4880-50, Hamamatsu): Measured intensities I_{CCD} are plotted against the expected intensities I_{Det}. The incident intensities were varied by inserting neutral density filters or varying the acquisition time of the CCD-camera. The unit of the intensity is the digitized value obtained from the CCD camera (12 Bit, $I \in [0, 4095]$). While the linearity is remarkably good a small nonlinearity remains. This nonlinearity is strong enough to seriously affect ellipsometric measurements. In unfavorable cases, without correction for nonlinearity, Ψ and Δ may even become uncomputable.

4.4 Image Persistence of the CCD Camera

Reference [Ilsin et al., 1991] reported that their photo diode array exhibited image persistence (IP) arising from incomplete readout of charges accumulated during the previous exposure, i.e. the measured count level C_n of the nth measurement owns a contribution proportional to I_{n-1} and is reduced by unread charges $\sim I_n$ affecting the subsequent image readout C_{n+1}:

$$C_n \sim (I_n - g \cdot I_n + g \cdot I_{n-1}). \tag{4.38}$$

In reference [Ilsin et al., 1991] $g = 0.55\%$ was found. In order to find out if this artifact affects the utilized CCD-camera, too, a series of images with varying exposure times was recorded. From these images only small regions exhibiting homogeneous intensity were utilized to compute laterally averaged intensities I. At each exposure time t

1. an image I^t_{o1} with open shutter (unaffected by IP, because of previous exposure with closed shutter)
2. a second I^t_{o2} image with open shutter (affected by IP)
3. an image I^t_{c1} with closed shutter (affected by IP)
4. a second image I^t_{c2} with closed shutter (unaffected by IP)

was taken. All intensities I^t_* were averaged over a small homogeneously illuminated partition of the full frame in order to avoid corruption due to nonlinearity. The leftovers from the last frame observable in a bright picture were computed by $I^t_{o2} - I^t_{o1}$, while for the image persistence visible in dark frames I^t_{c2} and I^t_{c1} were subtracted. The results are given in Fig. 4.4. Image persistence is present, but fortunately poses only a minor problem. Unlike reported in [Ilsin et al., 1991] the image persistence of the utilized CCD-camera is only weakly dependent on the count level of the previous frame, but there is a dependence on the pixel count level of the affected frame. The magnitude of this effect is considered to be negligible when the full dynamic range of the CCD camera is utilized.

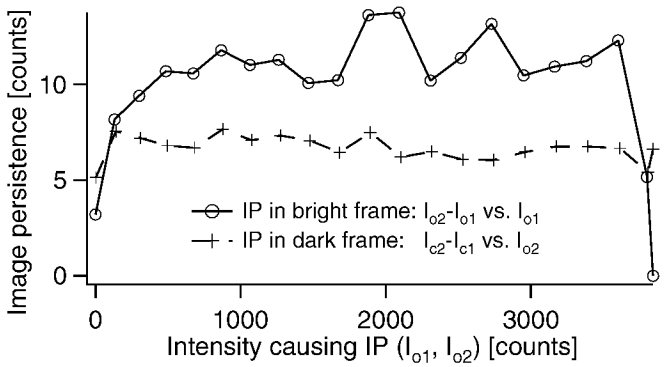

Figure 4.4: Image persistence (IP) visible in bright and dark images: The residual counts due to unread charges of previous frames were plotted against their inducing intensities. The inducing intensities were varied by adjusting the exposure time. The degree of IP seems to be almost independent of the inducing intensities, while there seems to be small dependence on the intensity of the affected frame. That way for the same inducing intensity IP is less pronounced in dark frames. The drop down of the last two points (bright frame - drawn line) is due to saturation of the CCD-camera.

4.5 Polarizer and Analyzer Imperfections

The quality of the utilized polarizers certainly has an influence on the measured Ψ and Δ values. The most common imperfection is, that the polarizing components pass light with an **residual ellipticity**, i.e. the Jones vector emerging from the component has the form $\begin{pmatrix} 1 \\ i\Gamma \end{pmatrix}$. The influence of this residual ellipticity on the calibration of the polarizer azimuth angles P and A was already discussed in Section 3.3.3. Here the effects on the measured ellipsometric quantities Ψ and Δ are discussed. Several publications [Aspnes, 1974a, Nijs and Silfhout, 1988, Radman and Cahan, 1981] treated the effects of component imperfections and here only the results are presented:

$$\delta\Psi = \Gamma_A \frac{(\cos(2P) - \cos(2\Psi))\sin(\Delta + Q)}{\sin(2P)} \tag{4.39}$$

$$\delta\Delta = -\Gamma_A \frac{(1 - \cos(2P)\cos(2\Psi))\cos(\Delta + Q)}{\sin(2P)\sin(2\Psi)} - \Gamma_P \frac{1}{\sin(2P)}. \tag{4.40}$$

Hence, the residual ellipticity Γ_P of the polarizer does not influence Ψ. Note that all contributions are again odd functions of the polarizer angle P. Thus they can be canceled by two-zone averaging at polarizer angles $-P$ and P. Especially when measuring near normal modes of the instrument, i.e. $P \approx 0°$ or $P \approx 90°$, a first order treatment may not be appropriate anymore. In that case the formulas treating optical activity exactly (derived in [Aspnes, 1974a]) have to be used. Due to the small magnitude of the residual ellipticities ($\Gamma \approx \mathcal{O}(10^{-3})$) the effect of component imperfections is almost negligible in typical operation modes of the ellipsometric microscope.

4.6 Influence of the Pinhole Size D

Assuming uniform illumination of the pinhole it is possible to give an estimate of the influence of the pinhole diameter D on the ellipsometric performance. The finite size of the pinhole affects the ellipsometric measurements in two ways: First, the finite diameter of the pinhole causes illumination of the sample with a broadened range of incident angles Θ. Second, the incident rays do not share a common plane of incidence anymore (Fig. 4.5(b)).

In the setup a magnified image of the pinhole is projected into the back focal plane of the microscope objective. The magnification factor is $\frac{D'}{D} = \frac{f_2 f_4}{f_1 f_3}$. Utilizing Abbe's sine condition $n \sin\Theta = const.$ (see Eq. (3.3)) and parameterizing the location within the pinhole with polar coordinates r, ϕ (see Figs. 3.3 and 4.5(a)) the relation between incident angle Θ and position (r, ϕ) within the pinhole is given by

$$\sin\Theta(r,\phi) = \frac{\sqrt{(d_M \frac{f_4}{f_3} + r\cos\phi)^2 + r^2 \sin^2\phi}}{n \cdot f_{\text{obj}}}, \tag{4.41}$$

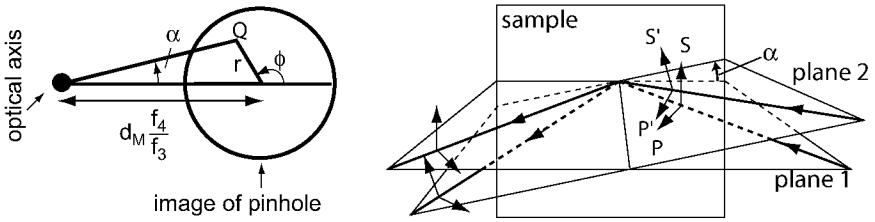

Figure 4.5: (a) shows how the location within the image of the pinhole is parameterized with spherical coordinates r, ϕ. This image is located in the back focal plane at a distance $d_M \cdot f_4/f_3$ to the optical axis. The sketch is not true to scale: at typical instrument settings the distance $d_M \cdot f_4/f_3$ is much larger than the diameter of the pinhole. Thus, the tilt angle α by which the different planes of incidence are inclinated is usually very small.
(b) Rays emerging from different locations within the pinhole do not share the same plane of incidence. Shown are two planes of incidence: Plane 1 represents the "ideal" plane of incidence if the pinhole would be infinitesimally small. All polarizer azimuthal angles are gauged with respect to this plane. Plane 2 is the plane of incidence for light originating from the point Q within the pinhole image. Both planes enclose a tilt angle α and therefore their p-s- and p'-s'-coordinate systems do not coincide. This causes mixing of p- and s- components of the incident and reflected electrical field vector.

where d_M is the distance of the deflection mirror to the optical axis, f_3, f_4, f_{obj} are the focal lengths of lenses 3, 4 and the microscope objective and n is the object side refractive index of the ambient medium.

The plane of incidence tilt angle α of a beam emerging from the point Q within the pinhole image is given by

$$\sin\alpha(r,\phi) = \frac{r\sin\phi}{d_M\frac{f_4}{f_3} + r\cos\phi}. \tag{4.42}$$

This tilt angle causes a mixing of p- and s-components (see Fig. 4.5(b)): The projection of the null-position of the polarizer-transmission axis into the p'-s'-plane of this tilted plane of incidence encloses an angle γ with the p'-axis (see Fig. 4.6). Thus, the polarizer and analyzer azimuth angles P and A are erroneous by the angle $\pm\gamma$.

The mixing angle γ can be computed according to the following geometric considerations: Parameterizing the direction of propagation $\mathbf{r}$ with spherical coordinates

$$\mathbf{r} = -\begin{pmatrix} \sin\Theta\cos\alpha \\ \sin\Theta\sin\alpha \\ \cos\Theta \end{pmatrix} \tag{4.43}$$

the axes parallel ($\mathbf{p}'$) and perpendicular ($\mathbf{s}'$) to the plane of incidence are given by

$$\mathbf{s}' = \frac{1}{|\sin\Theta|}\,\mathbf{r}\times\mathbf{e_z} \qquad \mathbf{p}' = \mathbf{s}'\times\mathbf{r}. \tag{4.44}$$

$\mathbf{s}'$ and $\mathbf{p}'$ are already normalized to unit length and $\mathbf{e_z} = (0,0,1)$ represents the normal to the surface of the sample. The projection $\mathbf{p_i}$ of the null-position of the polarizer-transmission axis into the $\mathbf{p}'$-$\mathbf{s}'$-plane is a vector parallel to the **x**-**z**-plane and perpendicular to the direction of propagation **r**:

$$\mathbf{p_i} = \mathbf{e_y} \times \mathbf{r}. \tag{4.45}$$

Thus, the mixing angle can be γ obtained from

$$\cos\gamma = \frac{\mathbf{p_i} \circ \mathbf{p}'}{|\mathbf{p_i}||\mathbf{p}'|} = \frac{\cos\alpha}{\cos^2\Theta + \cos^2\alpha\ \sin^2\Theta}. \tag{4.46}$$

In order to take this mixing of p- and s- components into account two more rotation matrices $\mathbf{R}_{\pm\gamma}$ have to be inserted into Eq. 2.20:

$$\mathbf{E}_{Det} = \mathbf{R}_{-A}\,\mathbf{T}_A\,\mathbf{R}_A\,\mathbf{R}_{\gamma(r,\phi)} \begin{pmatrix} R_p(\Theta) & 0 \\ 0 & R_s(\Theta) \end{pmatrix} \mathbf{R}_{-\gamma(r,\phi)}\,\mathbf{R}_{-P} \begin{pmatrix} 1 \\ 0 \end{pmatrix} E_0. \tag{4.47}$$

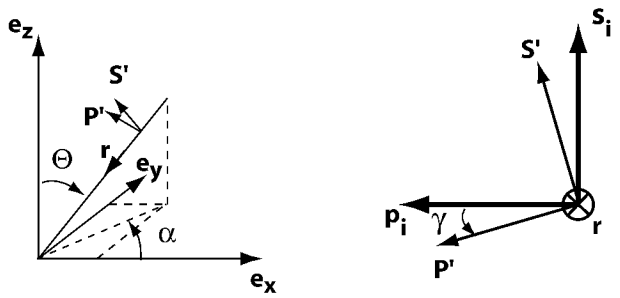

Figure 4.6: Geometry for computation of the mixing angle γ: The direction **r** of the incident light can be parameterized by spherical coordinates α, Θ (left). $\mathbf{p}'$ and $\mathbf{s}'$ are the axes parallel and perpendicular to the plane of incidence, respectively. The projection of the null-position of the polarizer-transmission axis - gauged with respect to the **x**-**z**-plane - into the $\mathbf{p}'$-$\mathbf{s}'$-plane yields the mixing angle γ (right).

Depending on the type of illumination (i.e. coherent or incoherent) either the electric field strength (Eq. (4.47)) or the intensity (Eq. (2.22)) measured at the detector has to be averaged over all incident angles. Although the primary light source is spatially incoherent a certain degree of spatial coherence is created in the object plane. The degree of coherence in the object plane can be estimated by the coherence parameter K [Haferkorn, 1986, Reynolds et al., 1989]

$$K = \frac{\mathrm{INA}}{\mathrm{NA}}, \tag{4.48}$$

where INA is the numerical aperture of the illumination and NA is the numerical aperture of the objective. In the limit $K \to 0$ the illumination is coherent while for $K \to \infty$ it is incoherent.

Here the INA is given by the diameter D of the pinhole projected into the back focal plane

$$\mathrm{INA} = n_1 \frac{D \cdot \frac{f_2 f_4}{f_1 f_3}}{2 f_{\mathrm{obj}}}, \tag{4.49}$$

resulting in completely coherent illumination for the utilized pinhole size of 50 μm ($K = 0.014$ for the dry objective and $K = 0.020$ for the oil immersion objective) and all further considerations are based on the averaged field strength at the detector $\overline{\mathbf{E}}_{Det}$

$$\overline{\mathbf{E}}_{Det} = \frac{1}{\pi (D'/2)^2} \int_0^{\frac{D'}{2}} dr \int_0^{2\pi} d\phi \; r \cdot \mathbf{E}_{Det} \overset{(4.47)}{=} \ldots \tag{4.50}$$

Thus, effects due to the finite pinhole size can be estimated by computing the intensity at the detector at several, in the range of 0° and 180° equally spaced analyzer angles A. For the model calculations shown in Fig. 4.7 and 4.8 averaged field strengths $\overline{\mathbf{E}}_{Det}$ were obtained by solving the integrals in equation 4.50 numerically using Mathematica. Converting field strengths into intensities the Fourier coefficients a and b can be extracted and the corresponding $\overline{\Psi}$ and $\overline{\Delta}$ were computed according to Eq. 2.26 and Eq. 2.27.

Model calculations of the effect of finite pinhole sizes are presented in Figures 4.7 and 4.8 for silicon and glass substrates. For both substrates deviations of Ψ become only important at pinhole diameters greater than 200 μm. At small pinhole diameters the moduli of the maximum deviations of Δ are approximately the same for both systems ($\approx 1°$). At larger pinhole sizes measurements utilizing glass substrates are much more error prone to finite pinhole sizes. The reason for this deviation is the existence of a thickness at which the incident angle equals the pseudo Brewster angle of the system, i.e. the angle where the parallel reflection coefficient exhibits a minimum due to maximal destructive interference. While the incident angle utilized for measurements on glass substrates is quite near to the Brewster angle of the interface ($\Theta_B = \tan^{-1}(n_3/n_1) \approx 41°$) the contrary holds for silicon substrates ($\Theta_B \approx 75°$) where angular averaging cannot effect great differences.

4.7 Influence of the Refractive Index of the Immersion Oil

The small mismatch in refractive index of immersion oil and cover slide might have an influence on the measured ellipsometric quantities. This small mismatch leads to an additional weakly reflecting interface. Depending on the coherence length and thickness of the cover slide this light superimposes either incoherently or coherently. Typical thicknesses d=170 μm cause the optical path difference within the cover slide to exceed the temporal coherence length $l_c < 300$ μm of high pressure mercury lamps [Born and Wolf, 1999]. Thus, the influence of the refractive index mismatch can be modeled by superimposing spurious stray light generated at this new interface. The results are shown in Fig. 4.9. Errors become largest where the deposited film of MgF_2 causes maximal destructive interference. Fortunately the effect is very

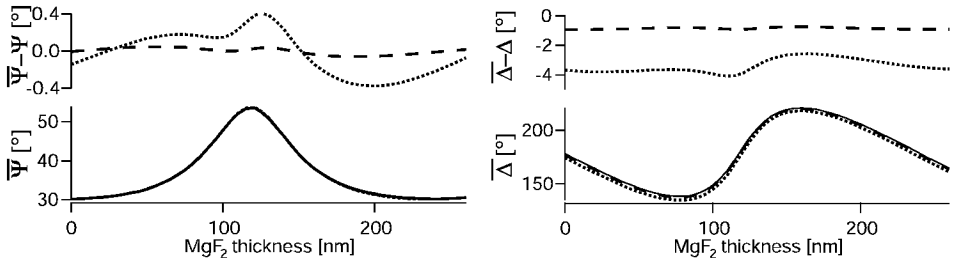

Figure 4.7: Influence of the finite pinhole diameter on Ψ and Δ for silicon substrates covered with thin layers of MgF_2 at an incident angle of 53.1°. Shown is the estimated influence of a pinhole with 50 μm (long dashed line) and 200 μm diameter (short dashed line), respectively. Ψ and Δ values for an infinitely small pinhole are represented by the thin continuous line.

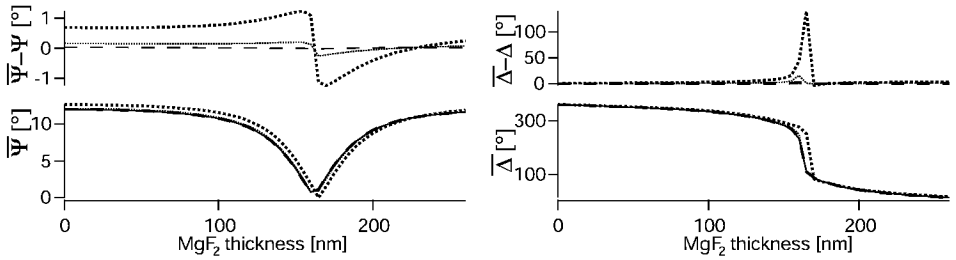

Figure 4.8: Influence of the finite pinhole diameter on Ψ and Δ for glass substrates covered with thin layers of MgF_2 at an incident angle of 46.3°. Shown is the estimated influence of a pinhole with 50 μm (long dashed line), 100 μm (thin short dashed line) and 200 μm diameter (thick short dashed line), respectively. Ψ and Δ values for an infinitely small pinhole are represented by the thin continuous line. Because of measuring near the pseudo Brewster angle of the interface deviations due to the finite pinhole size tend to become very large at thicknesses of maximal destructive interference. For the utilized pinhole (50 μm) the deviations are still acceptable.

localized to this special thickness regime. In this thickness regime very small values of Ψ are expected (cf. Fig. 4.8). Near $\Psi \approx 0°$ errors in Ψ and Δ tend to diverge (see Eqs. 4.1 and 4.2). Because of this, the influence of the immersion oil on the ellipsometric performance could not be distinguished experimentally from other systematic errors.

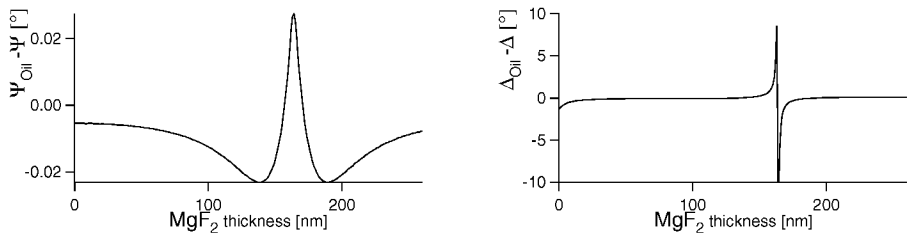

Figure 4.9: Influence of the refractive index difference between immersion oil (n=1.518) and cover slide (n=1.5255) assuming incoherent superposition of the reflected light. Effects are strongest for thicknesses of thin films which act like an anti-reflection coating, i.e. for film thicknesses which cause maximal destructive interference within the sample.

4.8 Instrumental Polarization

The imaging optical components are intended to transmit all polarization states equally. However, due to non normal incidence all optical components alter the polarization state of light to some degree. The overall polarization effect of an imaging device is referred to as *instrumental polarization* [Chipman, 1989].

Such instrumental polarization of optical systems can be analyzed by polarization ray tracing. By sending light rays of defined polarization through the optical system and keeping track of the changes its polarization suffers by transmission through optical surfaces, quantitative estimates of the instrumental depolarization can be obtained. A detailed introduction to this technique can be found in [Conrady, 1957, Waluschka, 1989]. In the following the basic idea of polarization ray tracing is summarized and an example of its application is given.

A polarized light ray owns several properties: a starting point, an unit length direction vector, two 3D-vectors of the current s- and p-coordinate system and a 2D-Jones vector describing the s- and p-component of the current electrical field, including the optical path length from the starting point. For each optical surface the following steps have to be executed:

- Compute the intersection of the ray with the optical surface. Add the optical path length to the phase of the electrical field.
- Compute the new direction of the at the surface refracted ray
- Compute the new s- and p- eigenvectors *before* the surface. Express the 2D-Jones vector in terms of this new coordinate system (projection).
- Multiply the Jones vector with the transmission coefficients of the surface.
- Compute the new s- and p- eigenvectors *after* the surface.

By repeating these calculations for several rays across the entrance pupil of the optical system its complete polarization aberration function can be sampled.

Such an analysis was performed for two lenses (Melles Griot, LAO 059, f=50 mm) forming a telescopic system (see Fig. 4.10). The data of the lens was obtained from the lens catalog of the optical design program SYNOPSYS (trial version). The code used for this simulation was a modified version[1] of a code written by my predecessor Klaus Neumaier [Neumaier, 1999].

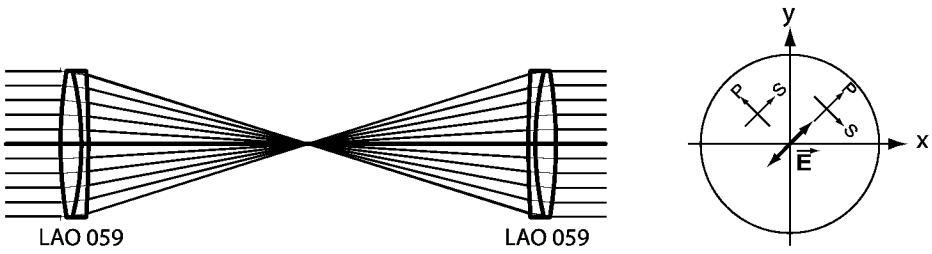

(a) (b)

Figure 4.10: (a) Setup for the depolarization study of lenses. Two doublets form a telescopic system. Shown are traces of rays entering the entrance pupil parallel to the optical axis of the system. (b) To the right the cross section of the entrance pupil is shown. The electrical field vector **E** of the incident light is polarized under 45°. The coordinate systems show that, although the initial polarization state is homogeneous, the different quadrants of the lenses have distinct dominating polarization states: While in the top-left quadrant the incident light predominantly is s-polarized the top-right quadrant shows almost complete p-polarization.

Figure 4.11 shows the computed intensity over the exit pupil of the telescopic system if it is placed between two crossed polarizers (oriented at ±45°). Along the diagonals of the exit pupil no intensity is transmitted, i.e. here the state of the incident polarization is unaltered. This is due to the fact, that along the diagonals the polarization of the incident light coincides with the eigenpolarizations of the surface, i.e. the incident light is either purely p- or s-polarized (see Fig. 4.10(b)). Hence depolarization is most pronounced in regions far from the center, where the incident polarization owns p- and s-components of equal strength. There the inequality of the transmission coefficients t_p and t_s (for incident angles $\neq 0°$) causes alteration of the polarization state.

Anti reflection coatings, here single $\lambda/4$-layers (n=1.37) on each outer surface of the lenses were assumed, seem to lower instrumental depolarization (Fig 4.11, right). This is just a result of the fact, that coatings designed to optimize transmittance $T_{p,s} \rightarrow 1$ (or reflectance) also minimize the difference $|T_p - T_s|$ of the transmission coefficients. Hence instrumental depolarization is less pronounced. Similar observations have also been described in Chipman [1989].

As a result of the inequality of the transmission coefficients T_p and T_s at non normal incidence the initial homogeneous and linearly polarized intensity is slightly inhomogeneous in the exit

[1]The modifications of this very well structured code regarded a general issue with the projections of s- and p-coordinate systems and an addendum to correctly handle anti-reflection coatings.

pupil (see Fig. 4.12). Because the different quadrants of the entrance pupil have distinct dominating polarization states (cf. Fig. 4.10(b)) the intensity profile in the exit pupil forms a saddle-like structure. Anti-reflection coatings again help to homogenize these variations.

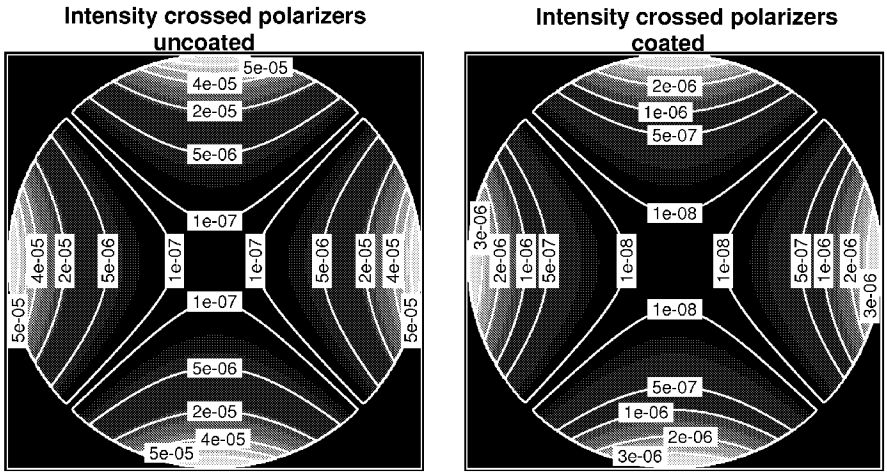

Figure 4.11: Visualization of instrumental depolarization by computing the transmitted intensity of a telescopic system placed between crossed polarizers. Anti-reflection coatings on the lenses (right) weakens instrumental polarization (see text).

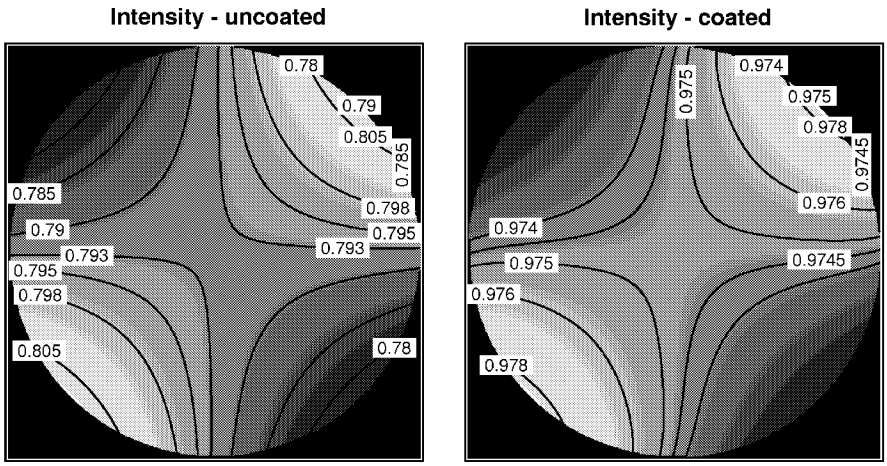

Figure 4.12: Influence of a telescopic system on a homogeneous, polarized and parallel light bundle: Instrumental polarization can lead to intensity variations across the exit pupil. Again, coatings (right) help to minimize this effect.

In order to quantify the meaning of instrumental polarization for ellipsometry Ψ and Δ of the telescopic system have been computed from the simulation data (Fig. 4.13). If the incident polarization is oriented at $P = 45^\circ$ Ψ and Δ are given by

$$\tan\Psi = \frac{E_y}{E_x} \tag{4.51}$$

$$\Delta = \phi_y - \phi_x, \tag{4.52}$$

where $\phi_{x,y}$ denotes the phase of the corresponding component $E_{x,y}$ of the electrical field vector. Phase shifts can only occur in coated systems. Because of that Fig. 4.13 shows Δ values only for the coated system. Hence, the lens system shows only diattenuation, i.e. intensity variation in dependence of the incident polarization, and almost no retardance [Chipman, 1989, Chipman and Chipman, 1989]. Depolarization is decreased to $\approx 20\%$ by the single-layer anti-reflection coating.

Considering the accuracy demands of ellipsometric microscopy the influence of a single telescopic system on the ellipsometric performance is negligible, especially if only high quality and anti-reflection coated lenses are used. However, instrumental polarization increases exponentially with the number of optical surfaces constituting the setup. The microscopic objective alone is built up of approximately ten lenses and hence is expected to exhibit a significant influence on the ellipsometric performance. For the introduced phase shift Δ birefringence induced by stress due to the mounting of the components is much more important than anti-reflection coatings. This is of course difficult to parameterize and hence computation of its effects from first principles is almost impossible. That is why microscope objectives employed in polarization applications are hand-selected by the manufacturer. For the ellipsometric microscope this means, that it will be necessary to treat instrumental polarization phenomenologically (see Section 6.1.1).

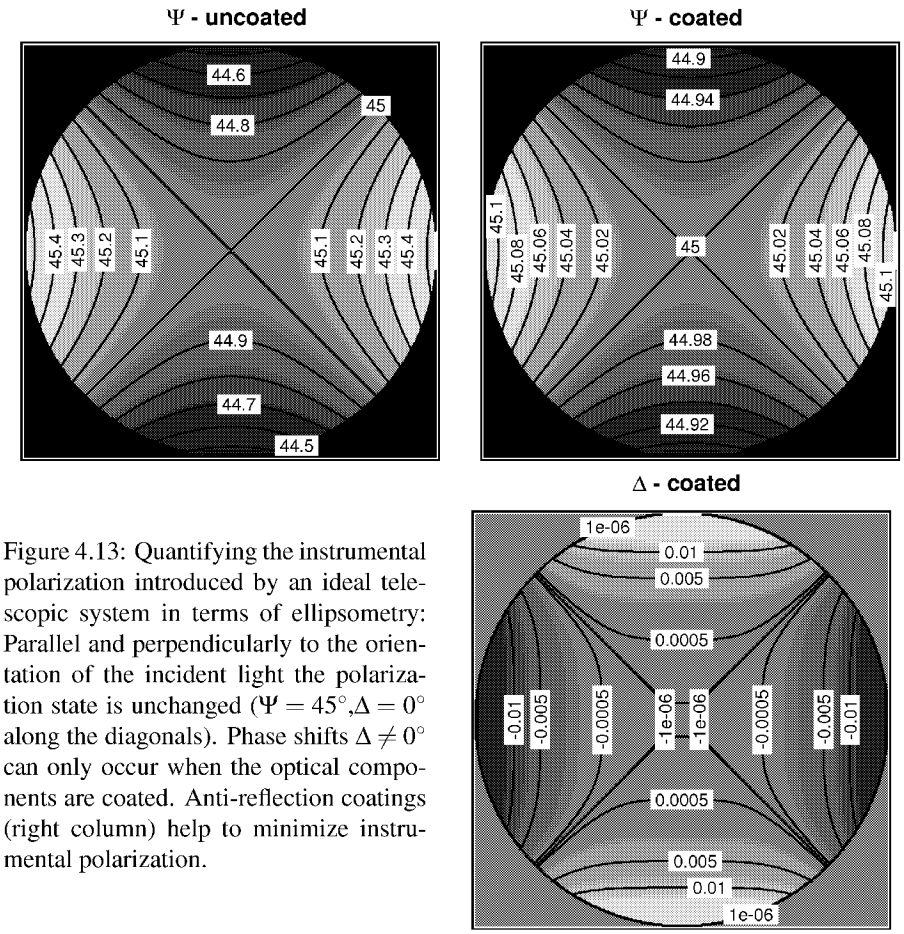

Figure 4.13: Quantifying the instrumental polarization introduced by an ideal telescopic system in terms of ellipsometry: Parallel and perpendicularly to the orientation of the incident light the polarization state is unchanged ($\Psi = 45°$,$\Delta = 0°$ along the diagonals). Phase shifts $\Delta \neq 0°$ can only occur when the optical components are coated. Anti-reflection coatings (right column) help to minimize instrumental polarization.

Chapter 5

Materials and Methods

5.1 Sample Preparation and Characterization

The samples used for calibration and measurements are thin structured films of MgF_2 or ZnS (99.99%, Goodfellow, Bad Nauheim) deposited upon a substrate by vacuum deposition. Because its refractive index is similar to hydrated proteins or lipids ($n \approx 1.40 - 1.48$ [Beuthan et al., 1996]) MgF_2 serves as a straightforward controllable model system. In order to check the performance of the ellipsometric microscope in a complete different refractive index regime thin films of ZnS (see Table 5.1) were deposited and measured (see Section 6.1.2). Cleaned silicon wavers (Wacker Siltronic, Burghausen) and standard microscope glass cover slides (Karl Hecht KG, Assistent) were taken as substrates. The silicon wavers were cleaned by successive ultrasonification in pure deionized water produced by a Millipore apparatus (Milli-Q Reagent Grade Water System, R>18 $M\Omega cm^{-1}$, pH 5.5, Millipore, Molsheim, France), ethanol and acetone for 15 minutes, each. Between each sonification step the wavers were rinsed ten times with Millipore water. The cover slides were cleaned by sonification (15 minutes) in a 2 vol% aqueous solution of Hellmanex (Hellma GmbH, Mühlheim, Germany). For removal of this detergent the cover slides were repeatedly rinsed (10 times) and sonificated in Millipore water. This cycle was repeated 3 times.

The structure was obtained by using an electron microscopy grid as a mask during the deposition (thermal evaporation, BOC Edwards Auto 306 Turbo, Kirchheim: substrate temperature 25°C, pressure $2 \cdot 10^{-6}$ mB, deposition rate: 4-7 nm/sec). The refractive index of deposited materials depends on the deposition parameters and has to be determined experimentally. In order to be able to determine the refractive index and thickness of the deposited layer accurately a second mask allowed for deposition within a 6×8 mm^2 region in close vicinity to the structured region. On these macroscopic plateaus refractive index and layer thickness were measured using a commercial point-ellipsometer ($\lambda = 632.8$ nm, Plasmos GmbH, München). The measured refractive indices were wavelength-corrected to 546.1 nm by multiplying with

ratios

$$\frac{n(\lambda = 546.1)}{n(\lambda = 632.8)} = \begin{cases} 1.0012 & \text{for} \quad MgF_2 \\ 1.0145 & \text{for} \quad ZnS \end{cases}$$

extracted from the literature[CrystalTechno LTD, Dodge, 1984, Opto - Technological Laboratory]. It was therefore assumed that contrary to the refractive index the dispersion does not depend on the deposition parameters.

Ordinary ellipsometry is not applicable for determination of the film thickness on glass substrates, because the backside air-glass interface introduces a spurious reflex. For these samples refractive indices were determined from ellipsometric measurements at auxiliary silicon substrates coated during the same deposition and closely located to the glass cover slides. Film thickness on the actual cover slides were determined by measuring the height of the macroscopic plateau with a stylus profiler (DekTak 3030ST, 2.5 μm needle, Veeco Instruments GmbH, München) and verified with geometry-corrected thicknesses measured with the point-ellipsometer on the auxiliary silicon wavers. While thickness measured on silicon wavers can be assumed to be precise, film thicknesses obtained for glass samples are assumed to be accurate up to ± 5 nm, which is the accuracy estimated from repeated stylus profiler measurements.

For the actual measurements the coated cover slides were mounted in a chamber which can be filled with fluids. Stress, which could make the cover slide birefringent, is only exerted at its very edge and therefore it is assumed to be free of birefringence.

Material	Refractive Index @ λ =546.1 nm
Air	1.000
Cover slide (Schott D263 glass)	1.5255 ± 0.0015
Immersion Oil (Immersol 518F, Zeiss)	1.518
MgF_2	1.389
Silicon	4.0879-0.03766i
SiO_2	1.465
Water	1.336
ZnS	2.379

Table 5.1: Refractive indices of the materials used. The values originate partly from specifications of the manufacturer (immersion oil, Schott D263 glass) and partly from wavelength-corrected measurements (MgF_2, silicon, SiO_2, ZnS). The refractive indices for air and water are widely accepted literature values [Schiebener et al., 1990].

5.2 Computer Hardware

The controlling computer (Pentium III, 500 MHz, 256 MB RAM) is equipped with a PCI-bus framegrabber card (PC-DIG, Stemmer Imaging, Puchheim) which is connected to the

12-/14-bit digital CCD camera (C4880-50-24, Hamamatsu, Hersching). Commands are sent to the CCD through the serial RS-232 interface. The shutter (electronic shutter ∅ 40 mm, Owis, Staufen), placed in the illumination path, is connected to the parallel interface of the computer. The polarizer stepping motors (DMT 65, Owis) and the motorized filter wheel (Owis) are controlled by an ISA-bus card (PC SM30, Owis).

5.3 Software

For image recording a new controlling software, based on Windows NT, was developed (MFC[1], Microsoft Visual C++ 6.0, 15.780 lines C++ code). It allows convenient adjustment of all camera parameters, acquisition and display of the current image, selection of regions and execution of automated calibration procedures. The measured data (2x18 pictures with and without compensator, each 1024^2 pixels) are stored in 16-bit TIFF file format [TIFF 6.0 Specifications], allowing interchange with commercial software (Photoshop, Mathematica, MatLab, IgorPro). Because of the need to store thickness and refractive index maps together with the measured raw data the TIFF image format was extended to allow for storage of floating point data.

For processing of the acquired raw data a separate image processing software was developed (30.000 lines C++ code, 3.700 lines FORTRAN code, cf. Fig. 5.1). It provides basic image processing capabilities such as profile selection, application of filters (median, Gaussian, high pass, etc...) and supports intuitive user handling (Drag and Drop). Apart from that it is specialized to ellipsometric needs and takes automatically care of all necessary computations and corrections. Using this software it is possible to compute the ellipsometric angles Ψ and Δ at each pixel recorded by the camera. The inherent quadrant ambiguity of Δ is automatically resolved by combining the two data sets with and without compensator. Within the software it is possible to define a model for the optical properties of the planar stratified layers of the sample and to fit the corresponding model function to either whole pictures or selected profiles of Ψ and Δ. By this procedure laterally resolved information about the refractive index n and the thickness d of any layer can be retrieved.

Fitting the model function to measured ellipsometric data involves heavy use of complex numbers and is relatively time consuming. Unfortunately complex numbers are seldom native data types of modern high level programming languages such as C/C++. FORTRAN is one of the few exceptions which still supports complex numbers as native data types. As a result of this FORTRAN computes complex number operations up to 37x faster than C++. Therefore all demanding calculations involving complex numbers were outsourced in a DLL[2] created by the FORTRAN 77 compiler of the GNU compiler collection (g77 from CygWin, open source)[3].

[1] Microsoft Foundation Classes: a library simplifying the development of Windows programs with graphical user interface.

[2] Win32 Dynamic Link Library: groups code in a library for reuse by other programs.

[3] There exists a C++ programming technique called "template metaprogramming" [Eisenecker and Krzysztof, 1998] which combines the ease of C++ operator notation, i.e. hiding a function call which implements complex number or matrix multiplication behind the notation $c = a * b$, with the speed accustomed from FORTRAN

Compared to a straightforward C++ implementation due to the use of FORTRAN the same algorithm is estimated to work about 10x faster (1D-fit of 1024^2 pixel: 15 minutes, 2D-fit: 3 hours [4]). The employed fitting algorithm is based[5] on the Powell minimization procedure presented in "Numerical Recipes" [Press et al., 1986]. This method was chosen, because it does not require analytic expressions for the derivatives of the function to be minimized.

5.4 Image Recording and Processing

During image recording several components have to be controlled: polarizer, analyzer, shutter, CCD camera and the framegrabber. Because of the rotating-analyzer-scheme intensity pictures had to be recorded at several analyzer settings. The 12-/14–bit count level output of the CCD camera exhibits a constant offset (ca 250 counts for the 12-bit mode). For removal of this offset additional pictures with closed shutter were subtracted from the measured data.

Because the intensity at the detector can differ significantly for the various analyzer settings, the exposure time of the CCD camera has to be controlled in order to avoid saturation. Two possible procedures were used:

- fixed exposure time
- variable exposure time

When fixed acquisition times are utilized it is necessary to determine the maximum possible exposure time in advance of the actual measurement: It is chosen such that the image at the analyzer position with the highest intensity transmission optimally utilizes the full dynamic range of the CCD camera. This exposure time is then used at all analyzer settings. In order to increase the dynamic range of the CCD camera further variable exposure times can be used: The optimum exposure time can be determined at each analyzer setting. Thus, in contrary to fixed acquisition times, the full dynamic range of the CCD camera is used at every analyzer setting angle. Fixed exposure times result in much faster measurement times. Especially when measuring weakly reflecting samples, e.g. at the glass-water interface, exposure times

programs. Metaprograms are pieces of code evaluated at compile time by the C++ preprocessor. These metaprograms generate the code necessary for the specific operation (e.g. multiplication of complex numbers or matrices), thus unrolling inner loops and avoiding overhead from function calls. The facility of this programming technique was detected after the C++ standard was extended with "templates" in 1994. Erwin Unruh circulated 1994 a program among the members of the C++ standard committee which generated a list of prime numbers. The program did not compile successfully but presented its output in form of warning messages. Nowadays template metaprogramming is used to highly optimize vector and matrix multiplication in C++. Though very instructive, because of its extreme difficulty to debug those metaprograms and its very distinct compiler dependence, this approach was not pursued here.

[4] Pentium compatible, 2.5 GHz

[5] Modifications were necessary because in rare occasions their code crashed. As evaluation of a full image implies 10^6 independent fits basically every measurement was affected. Modifications regarded the abortion criteria, which misjudged the achieved degree of minimization in rare occasions, leading to an overflow in another subroutine (mnbrak) of the Numerical Recipes.

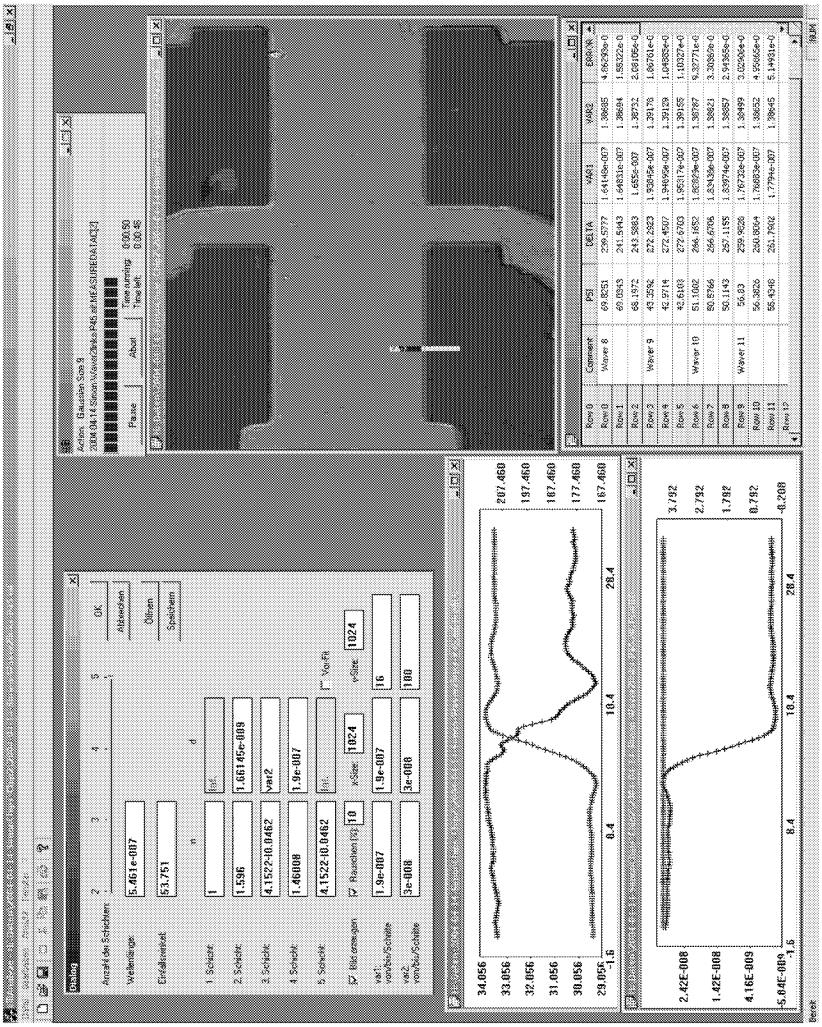

Figure 5.1: The ellipsometric image processing software developed for this thesis: To the right a Ψ picture of the sensitive area of a biosensor device is shown [Nikolaides et al., 2003]. Above the picture the progress of a background process, here Gaussian averaging of the measured raw data, is displayed. The top plot to the left shows the Ψ-Δ-profile selection across the edge of the structure. Edge diffraction phenomena are clearly visible. The bottom plot gives the resulting thickness, fitted with the layer system visible in the layer definition dialog (top left). To the bottom right data can be arranged within a spreadsheet, allowing fitting of ellipsometric data from point measurements or copy-paste data exchange with MS Excel.

$>$ 1 minute can make searching for optimum exposure times time consuming. But variable exposure times considerably enhance the dynamic range of the CCD camera. Therefore the software allows for predefined exposure time profiles, which avoids the time consuming search for optimum exposure times.

For acquisition of raw data the following steps were performed:

1. Setting polarizer at angle P.
2. Positioning the analyzer.
3. Opening shutter and recording an image. Averaging of several subsequent images is possible.
4. Closing the shutter and recording background image
5. Subtracting the background image from the recorded data.
6. Saving Image
7. Rotate compensator into the illumination beam and repeat steps 3.-6. Afterwards rotate compensator out of the beam again.
8. Repeating steps 2.-7. at each analyzer setting.

Images were saved in 16-bit TIFF file format. Within the separate image processing software the slight nonlinearity of the CCD camera was corrected. For that the inverse of the measured nonlinearity (see Fig. 4.3) was interpolated with cubic splines. The resulting images were converted to a 4-byte floating point format and normalized to an exposure time of one second. At each pixel discrete (Fourier) sine- and cosine-transformations were made through the stack of pictures at different analyzer angles. The resulting coefficients a, b, a^c and b^c from Eq. 2.22 (Eq. 2.30, respectively) were used to compute Ψ- and Δ- as well as Ψ^c- and Δ^c-images. The software thereby automatically takes care of correcting the quadrant ambiguity of Δ and Δ^c (see Section 2.2.2). Optionally, the resulting Ψ- and Δ-images can be averaged with Ψ- and Δ-images from a second measurement taken at polarizer angle $-P$. This zone averaging helps to suppress systematic errors (see Section 4.2). The resulting ellipsometric images were then corrected for the influence of the imaging optics (cf. Section 6.1.1).

5.5 More Image Processing: Selected Topics

Though lateral averaging of measured raw data is not compulsory at this stage of development of the ellipsometric microscope, it may be useful to smooth data, especially when very thin films, where the relative error becomes large, are measured. Because of the lateral optical resolution limit of ca 1 μm (cf. Section 6.4) any averaging procedure with a kernel diameter up to 5 pixels (7 when the oil immersion objective is used) does not remove physical information anyway.

5.5.1 Median Filter

An image is median filtered by moving a window over the image and replacing the center pixel by the median value of the brightnesses within this input window. If the window size is $J \times K$ and odd the $J \cdot K$ pixels are ordered in brightness and the median will be the $(J \cdot K + 1)/2th$ entry [Russ, 1995]. The median filter has some interesting properties: It leaves edges and smooth transitions (almost) unchanged and corrects particularly outliers (see Tab. 5.2 and Fig. 5.2).

structure	input	output
transition	...4 5 6 7 8 9...	...4 5 6 7 8 9...
edge	...7 7 7 0 0 0...	...7 7 7 0 0 0...
outlier	...4 5 100 7 8 9...	...4 5 7 8 8 9...

Table 5.2: Effect of a one dimensional median filter with kernel size 3. Smooth transitions and sharp edges are left untouched while outliers are corrected.

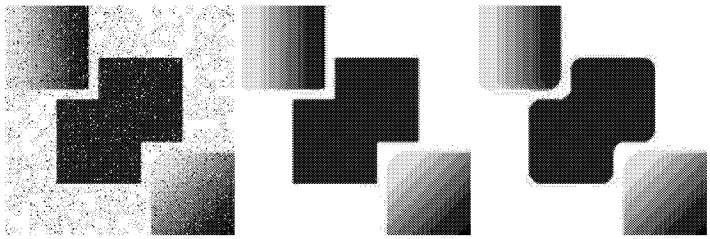

Figure 5.2: Effect of a two dimensional median filter. The "salt and pepper" noise of the image to the left is already removed by a median filter with kernel size 3 (middle). At very large kernel sizes image shapes tend to decay, especially where they intersect and corner (right, kernel size 21).

5.5.2 Isotropic Gaussian Filter

The Gaussian smoothing operator is also used to blur images and removes details and noise. Its kernel is chosen as to approximate the shape of a 2D-Gaussian distribution

$$G(x,y) = \frac{1}{2\pi\sigma^2} e^{-\frac{x^2+y^2}{2\sigma^2}}. \tag{5.1}$$

Here the standard deviation σ of the distribution was chosen equally for both orthogonal directions. Hence this Gaussian distribution is called isotropic. The filtered image $I'(x,y)$ is obtained by convolving the input Image $I(x,y)$ with the filter function $G(x,y)$. The discretized

convolution of an image with a square $M \times M$ kernel (M odd) is computed by

$$I'(i,j) = \sum_{m=0}^{M} \sum_{n=0}^{M} I(i-m-R, j-n-R) \cdot g(m,n). \tag{5.2}$$

where $R = (M-1)/2$ is the radius of the kernel. The kernel is shifted over the image and its value is multiplied with the corresponding pixel values of the image. The center pixel is replaced by the sum of those products. A straightforward implementation of this operation may be similar to the one shown in Listing 5.1. This implementation involves four nested **for**-loops and is therefore quite time consuming. As in this application usually not only one picture but all 36 raw data pictures have to be processed the need for the most efficient implementation is obvious.

The implementation can be made much more efficient by exploiting the fact, that the Gaussian filter is *separable*, i.e.

$$G(x,y) = \frac{1}{\sqrt{2\pi}\sigma} e^{-\frac{x^2}{2\sigma^2}} \cdot \frac{1}{\sqrt{2\pi}\sigma} e^{-\frac{y^2}{2\sigma^2}} = G_{1D}(x) \cdot G_{1D}(y). \tag{5.3}$$

Rewriting Eq. (5.2) in discretized form the convolution can be divided into two steps:

$$\begin{aligned} I_{\text{tmp}}(i,j) &= \sum_{m=0}^{M} I(i-m-R, j) \cdot g(m) \\ I'(i,j) &= \sum_{n=0}^{M} I_{\text{tmp}}(i, j-n-R) \cdot g(n). \end{aligned} \tag{5.4}$$

Thus filtering is carried out by two consecutive one dimensional filtering procedures, one within columns only and a second within only the rows. Implementing convolution following this scheme (see Listing 5.2) is already at the smallest kernel size 3 more than 1.5 times faster. The speed advantage increases rapidly with increasing kernel size.

Listing 5.1: Straightforward implementation of convolution. Four nested **for**-loops make this code quite inefficient.

```
//Naive convolution
for(i = R; i < N-R; i++){
  for(j = R; j < N-R; j++){
    ImageOut(i,j) =0;
    for(m = 0; m < M; m++){
      for(n = 0; n < M; n++){
        ImageOut(i,j) += ImageIn(i-m-R,j-n-R) * Kernel2D(m,n);
}}}}
```

Listing 5.2: Implementation of convolution exploiting separability of the kernel of the operation.

```
//First convolution within columns...
for(i = R; i < N-R; i++){
  for(j = R; j < N-R; j++){
    ImageTmp(i,j) = 0;
    for(m =0; m < M ; m++){
      ImageTmp(i,j) += ImageIn(i-m-R,j) * Kernel1D[m];
    }}}

//...then convolution within rows
for(i = R; i < N-R; i++){
  for(j = R; j < N-R; j++){
    ImageOut(i,j) = 0;
    for(n =0; n < M ; n++){
      ImageOut(i,j) += ImageTmp(i,j-n-R) * Kernel1D[n];
    }}}
```

Chapter 6

Results and Discussion

In this chapter the performance of the ellipsometric microscope is demonstrated. The experiments are presented in sections organized according to the employed substrate: First measurements at the air-silicon interface are shown and the necessary calibration procedure for the instrumental polarization of the imaging optics will be developed. The achieved accuracies for determination of film thicknesses and refractive indices are presented.

Subsequently experiments at the glass-water interface are shown. The small difference in refractive index between substrate (glass) and ambient medium (water) turned out to require additional measures in order to achieve good ellipsometric performance. Hence, the setup of the ellipsometric microscope had to be adapted. This modified setup is presented and the obtained results are shown.

The chapter is concluded by a discussion about the achieved lateral resolution and the vertical sensitivity of the instrument.

6.1 Measurements on Silicon Substrates

In order to obtain information on the accuracy of the ellipsometric microscope, homogeneous areas of the MgF_2 coated silicon substrates (described in Section 5.1) were measured. All presented ellipsometric quantities were computed from laterally averaged ($\sim 25 \times 25\ \mu$m) intensities. It will be shown later (cf. Section 6.1.2), that this lateral averaging is not necessary. Additionally the presented values were zone averaged in order to avoid systematic errors like component azimuth errors and polarizer imperfections (cf. Section 4.2). Great care was taken to accurately characterize the deposited thin films with an commercial point-ellipsometer to allow for accurate comparison with the expected data: The measured refractive indices were wavelength-corrected to the wavelength employed in the ellipsometric microscope. The measured film thicknesses and the corrected refractive indices were used to compute theoretically expected ellipsometric quantities Ψ and Δ. Figure 6.1 shows the results obtained by the ellipsometric microscope in comparison to this theoretical data.

While qualitatively the agreement between measured and expected data is remarkably good, systematic disagreements are clearly visible. More interesting is the fact, that measurements with and without the compensator show considerable disagreements as well. As the quantities shown are already zone averaged this does not stem from erroneous settings of the component azimuthal angles. Furthermore it was impossible to compute valid Δ values at several thicknesses: the experimentally determined Fourier coefficients a and b produced right-hand sides of Eq. (2.27) (Eq. (2.40), respectively) with moduli larger than one. In Fig. 6.1 the corresponding values were set to an arbitrary value of 100°.

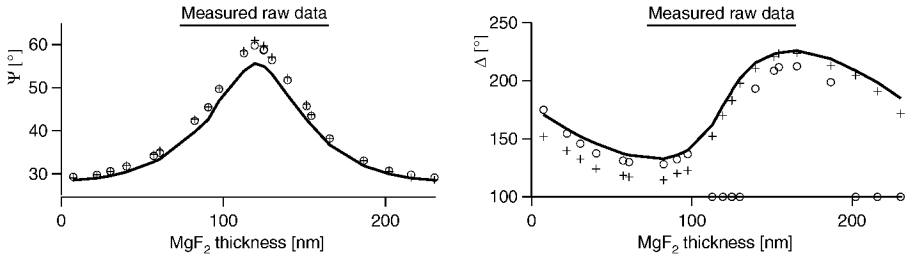

Figure 6.1: Measured ellipsometric quantities in comparison to expected data (thick line): Shown are plain and uncorrected Ψ and Δ values obtained at an incident angle $\Theta = 55.3°$ from MgF_2 coated silicon substrates. Measurements with (crosses) and without (circles) compensator ($\lambda/4$-wave plate) in the optical path show considerable disagreements.

Since azimuthal errors and component imperfections were already eliminated possible remaining error sources were stray light, arising from internal reflections at the optical components within the microscope, detector imperfections and instrumental polarization (see Chapter 4).

Recording pictures with no sample mounted in the object plane yielded pictures of the internal reflections within the microscope. Subtracting these images from the measured data and recomputing the ellipsometric quantities revealed, that residual stray light influences Ψ and Δ by not more than 0.5°. Naturally, this way only internal reflections created by the illuminating beam can be measured. Internal reflections created by the light reflected at the object cannot be taken into account. Nevertheless this attempt proved, that using silicon substrates internal stray light can be considered to be of minor importance.

The linearity of the employed CCD camera was already presented in Section 4.3. Correcting the observed slight nonlinearity can proceed following either of two possible ways: Either the measured intensities are linearized directly by generating a lookup table of the inverse of the measured linearity, or the Fourier coefficients a and b are computed from nonlinearity affected intensities and corrected according to the inverse of Eq. (4.35) and (4.36). Figure 6.2 shows intensity-linearized ellipsometric quantities in comparison to expected data. The mentioned lookup table was interpolated using cubic splines [Press et al., 1986].

Clearly the slight nonlinearity of the CCD camera was responsible for the observed disagreement of measurements with and without compensator. The excellent agreement of measure-

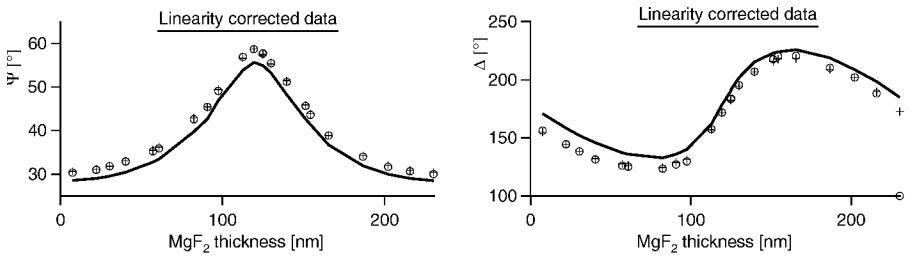

Figure 6.2: Measured and linearity-corrected ellipsometric quantities in comparison to expected data (thick line): Correcting the slight nonlinearity of the CCD camera brings measurements with (crosses) and without (circles) compensator in very good agreement. Nevertheless a considerable difference to the theoretical expected data remains.

ments with and without compensator are a strong indication that other detector imperfections (like polarization dependent sensitivity) are not present.

Furthermore, the nonlinearity correction rendered most former uncomputable Δ to sensible values. Correcting for nonlinearity on the level of the Fourier coefficients turned out to yield similar good corrections, but did not succeed to correct uncomputable ellipsometric quantities as frequently. Thus, in the following the nonlinearity is always corrected on the intensity level.

6.1.1 Calibration of the Instrumental Polarization

The influence of the imaging optical components on the state of polarization is called *instrumental polarization*. Instrumental polarization is difficult to treat from first principles. As already shown in Section 4.8 stress-induced birefringence due to mounting of the optical components is the major cause for the introduced phase shifts, causing deviations in Δ. If the exerted stress could be parameterized complicated FEM simulation might provide numerical corrections for this effect. As the manufacturers of the utilized objectives keep the construction plans confidential this is not practical, anyway.

Here a well motivated, phenomenological approach was found to account for instrumental polarization. The major source of depolarization is the microscope objective, being composed of numerous lenses. As the sample is illuminated through the objective, it alters the polarization of the light before and after reflection at the sample. Since the numerical aperture of the illumination is extremely small, the light bundle carrying the ellipsometric information covers only a small part of the cross section of the objective. Hence, its influence can be modeled neglecting the angular dispersion of the incident light and independent of the position in the object plane.

The simplest model for the instrumental polarization of the imaging optics thus is to formally treat it exactly as the sample itself: By parameterizing its influence with values Ψ_{Obj} and Δ_{Obj},

In Eq. (2.20) the Jones matrix of the sample

$$\begin{pmatrix} \tan\Psi e^{i\Delta} & 0 \\ 0 & 1 \end{pmatrix}$$

is then replaced by

$$\begin{pmatrix} \tan\Psi' e^{i\Delta'} & 0 \\ 0 & 1 \end{pmatrix} = \begin{pmatrix} \tan\Psi_{\text{Obj}} e^{i\Delta_{\text{Obj}}} & 0 \\ 0 & 1 \end{pmatrix} \cdot \begin{pmatrix} \tan\Psi e^{i\Delta} & 0 \\ 0 & 1 \end{pmatrix} \cdot \begin{pmatrix} \tan\Psi_{\text{Obj}} e^{i\Delta_{\text{Obj}}} & 0 \\ 0 & 1 \end{pmatrix},$$

giving rise to the following correction laws:

$$\tan\Psi' = \tan\Psi \cdot \tan^2\Psi_{\text{Obj}} \tag{6.1}$$

$$\Delta' = \Delta + 2\Delta_{\text{Obj}} \tag{6.2}$$

Thus, following this approximation the objective adds a constant offset $2 \cdot \Delta_{\text{Obj}}$ to the measured Δ and $\tan\Psi$ is scaled with a constant factor. Comparing this to the results presented in Fig. 6.2 shows that this is indeed very close to the observed behavior.

Minimizing the sum

$$\sum_i \left(\Psi_i^T - \tan^{-1}\left(\frac{\tan\Psi_i'}{\tan^2\Psi_{\text{Obj}}} \right) \right)^2 + \left(\Delta_i^T - \left(\Delta_i' - 2 \cdot \Delta_{\text{Obj}} \right) \right)^2, \tag{6.3}$$

where Ψ_i^T and Δ_i^T are theoretically expected values and Ψ_i' and Δ_i' are the experimentally determined ellipsometric quantities, yields the sought correction parameters Ψ_{Obj} and Δ_{Obj}. The index i comprises all performed measurements, including the ones with inserted compensator. For the employed objective (Olympus MPlanApo 50x, NA=0.95) the following values were found: $\Psi_{\text{Obj}} = 46.33^\circ$ and $\Delta_{\text{Obj}} = -4.51^\circ$. Figure 6.3 shows the very good agreement of corrected measurements with the expected ellipsometric quantities.

In order to check the validity of this calibration scheme (detector nonlinearity + instrumental polarization) several tests were made. The questions addressed by these tests were:

- Is the calibration scheme valid in the complete domain of the ellipsometric quantities ($\Psi \in [0^\circ, 90^\circ]$, $\Delta \in [0^\circ, 360^\circ[$)?
- Does it hold for incident polarizations $P \neq 45^\circ$ (as theoretically expected)?
- Do the quantities Ψ_{Obj} and Δ_{Obj} vary with the incident angle Θ?

In order to address the first question silicon substrates were covered with thin films of ZnS (n=2.38). These samples test exactly the complement of the Ψ-domain already measured with the MgF_2 coated samples and their Δ-values cover almost the whole domain $[0^\circ, 360^\circ[$ (e.g. compare Figures 6.1 and 6.5(a)).

The latter two points were tested by varying the polarizer setting angle P and the incident angle. Figures 6.5-6.8 display the experimental results: Figures 6.5(a)-6.8(a) show already

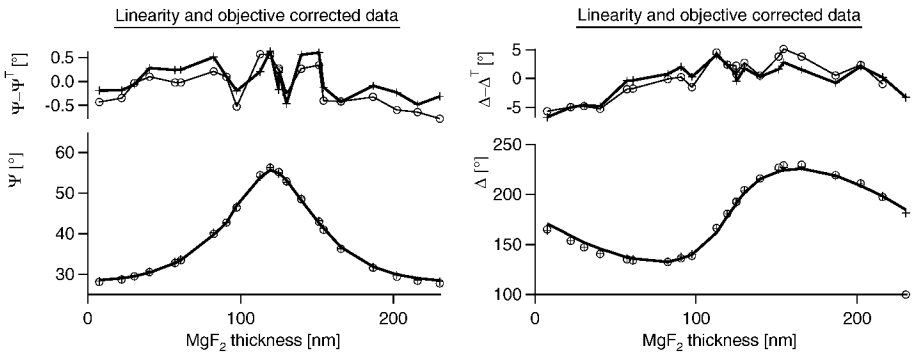

Figure 6.3: Measured and corrected ellipsometric quantities in comparison to expected data (thick line). The angle of incidence was $\Theta = 55.31°$. Accounting for detector nonlinearities and instrumental polarization removes all major systematic error sources. Data with (crosses) and without compensator (circles) are in good agreement and show similar residuals.

linearized measurements in comparison to expected data. Again, the measured quantities exhibit considerable systematic deviations. In Figures 6.5(b)-6.8(b) the measured values are corrected for instrumental polarization. The values found for Ψ_{Obj} and Δ_{Obj} by minimizing Eq. 6.3 are summarized in Table 6.1 [1]. The values are in excellent agreement with the values found utilizing the MgF_2 samples. As expected they are independent of the incident polarization. Within the screened range the instrumental polarization is also independent on the incident angle. Although the incident angles chosen do not differ much they represent the most typical settings: In order to achieve largest ellipsometric accuracy the incident angle should be as close as possible to the Brewster angle of the substrate (silicon $\approx 75°$) [Hauge and Dill, 1973]. $\Theta = 55.31°$ is the largest possible angle for the utilized objective, where the whole field of view can still be illuminated by epi-illumination.

The residue of the corrected ellipsometric quantities show larger deviations only near to a ZnS layer thickness of 61 nm, where Ψ displays a minimum and Δ is discontinuous. These deviations partly stem from the great proneness to systematic errors when measuring far from the $P_{opt} \approx \Psi$ condition (see Section 4). In addition, theoretical uncertainties about the optical properties n and d of the coated ZnS layer contribute also to the observed difference: An uncertainty of 1 nm in the layer thickness leads at an overall layer thickness of about 61 nm to 14° uncertainty in Δ. These are the reasons why the discontinuous feature in Δ is difficult to reproduce.

[1] Because of great proneness to systematic errors the discontinuous feature in Δ is difficult to reproduce. Therefore is is reasonable to exclude measurements exhibiting large residuals in the minimization procedure. The values presented in Table 6.1 are obtained by omitting just the two Δ- and Δ^c-data points nearest to the discontinuity (e.g. data points #8 and #9 in Fig. 6.5(a)). For completeness the resulting values for inclusion of *all* data points are given exemplary for the measurement with $\Theta = 55.13°$ and $P = 45°$: $\Psi_{Obj} = 46.58°$ and $\Delta_{Obj} = -3.23°$.

Material	Parameters	Ψ_{Obj} [°]	Δ_{Obj} [°]
MgF_2	$\Theta = 55.31°$, P=45°	46.33	-4.51
ZnS	$\Theta = 53.13°$, P=45°	46.60	-4.54
ZnS	$\Theta = 55.31°$, P=45°	46.58	-4.44
ZnS	$\Theta = 53.13°$, P=30°	46.73	-4.36
ZnS	$\Theta = 55.31°$, P=30°	46.59	-4.53

Table 6.1: Experimentally determined instrumental depolarization parameters of the imaging components.

6.1.2 Accuracy of Measurements at Silicon Substrates

Having ensured that the ellipsometric microscope measures Ψ and Δ accurately the next step is to evaluate its accuracy with respect to determination of the optical properties of the thin film. Webster's dictionary defines accuracy as "the extent to which a given measurement agrees with the standard value for that measurement". Here the standard or true value for the optical properties is assumed to be the wavelength-corrected refractive index and the thickness as obtained by the commercial point-ellipsometer. As the spot size of this ellipsometer is approximately 1 mm^2 these reference values represent laterally averaged quantities. As explained in Section 2.2.3 the optical quantities n and d are obtained by fitting the measured ellipsometric quantities to a model function for Ψ and Δ. As two quantities are measured, up to two optical properties can be determined simultaneously.

Fig 6.4(a) and 6.5(c)-6.8(c) show the results obtained by fitting n and d simultaneously from the corrected ellipsometric measurements. While for intermediate thicknesses the results are in excellent agreement with the expected values the errors of the refractive index become very large at very small layer thicknesses. The same is true for layer thicknesses close to the period of the ellipsometric quantities. As a consequence of this the relative error of the determined thickness becomes also very large. This behavior is theoretically expected and the reason for it was already discussed in Section 2.2.4: Near to layer thicknesses of $d \approx k \cdot D_\Theta$ ($k \in \mathbf{R}_0^+$) the ellipsometric quantities become insensitive to the refractive index of the layer. Hence the retrieved refractive indices become erroneous. As the optical thickness $n \cdot d$ is still measured accurately the determined thickness is erroneous, too.

In these cases one optical quantity has to be imposed in order to extract the other with a high degree of accuracy. Fig 6.4(b) and 6.5(d)-6.8(d) show the results, when the refractive index is imposed and the layer thickness is obtained by means of a one dimensional fit. The obtained thicknesses d_i^M are in excellent agreement with the expected values d_i and the residue are usually well below 5 nm. Table 6.2 summarizes the average absolute deviation

$$\overline{|\Delta d|} = \frac{1}{N} \sum_{i=1}^{N} |d_i^M - d_i|$$

of the measured thicknesses from their expected value at several instrument settings. It shows very impressively that the overall height-accuracy of the ellipsometric microscope is better

than 3 nm when the refractive index of the thin layer is imposed. The results of the same analysis for 2D-fits and intermediate thicknesses is summarized in Table 6.3. Refractive indices are measured with an accuracy better than 2.5% while thicknesses are accurate to approximately 2.5 nm.

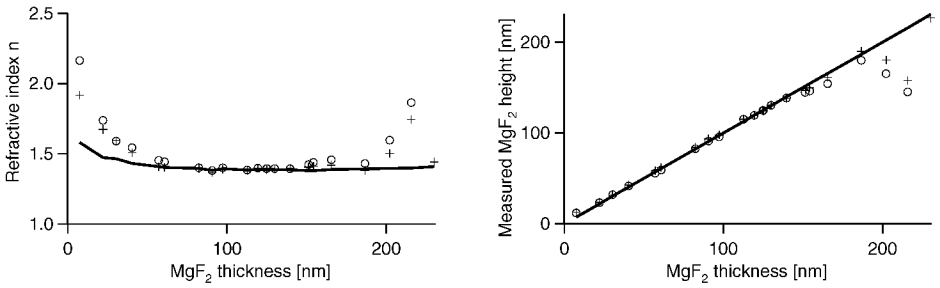

(a) 2D-fit

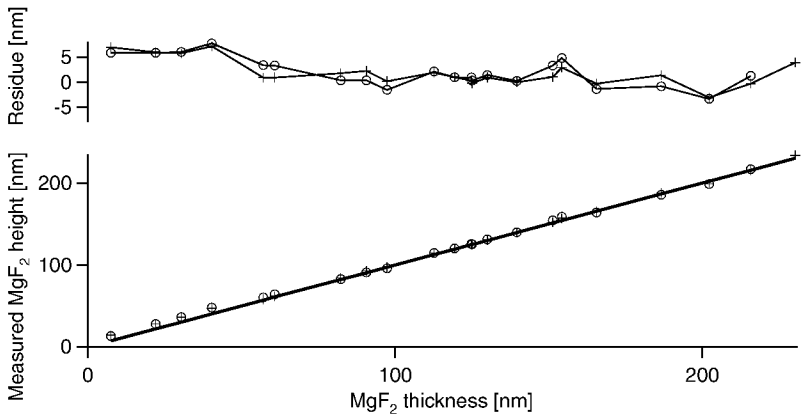

(b) 1D-fit

Figure 6.4: (a) Refractive indices and thicknesses simultaneously obtained by means of a 2D-fit from zone averaged ellipsometric data corrected for detector nonlinearities and instrumental polarization: Shown are data measured with (crosses) and without (circles) compensator. The thick line represents expected data determined with a commercial point-ellipsometer. (b) Resulting thicknesses if the refractive index of MgF_2 (n=1.389) is imposed.

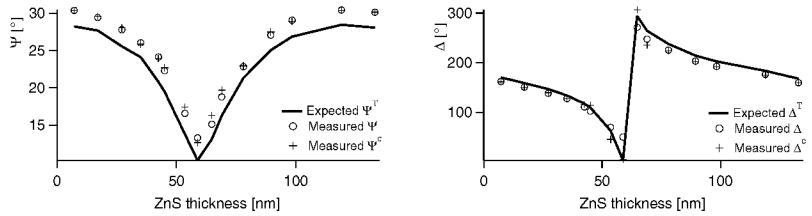

(a) Linearity corrected raw data.

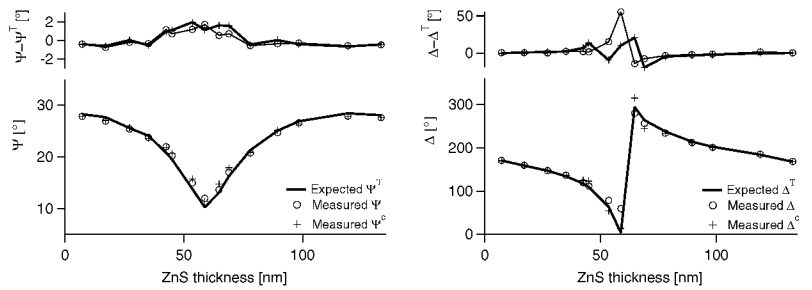

(b) Data corrected for instrumental polarization.

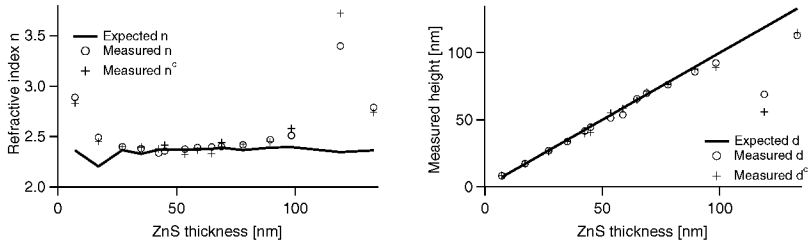

(c) n and d obtained by means of a 2D-fit to corrected Ψ and Δ.

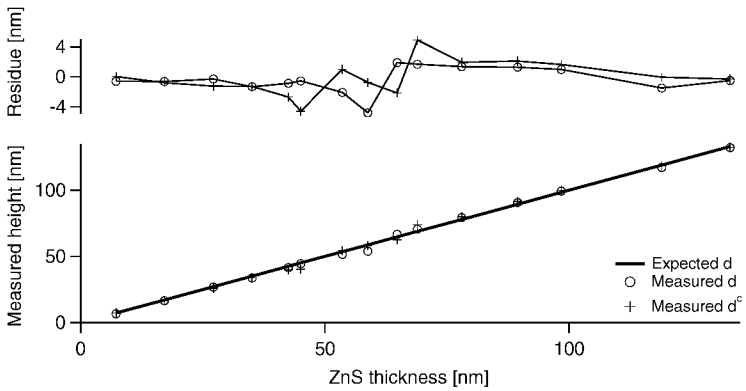

(d) $n = 2.379$ imposed and d retrieved by a 1D-fit to corrected Ψ and Δ.

Figure 6.5: Measurements at silicon wavers coated with layers of ZnS: $\Theta = 55.3°$, $P = \pm 45°$.

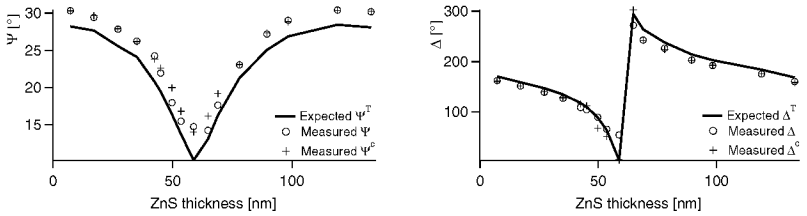

(a) Linearity corrected raw data.

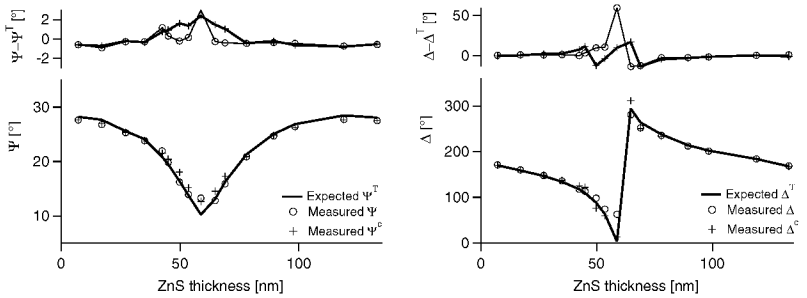

(b) Data corrected for instrumental polarization.

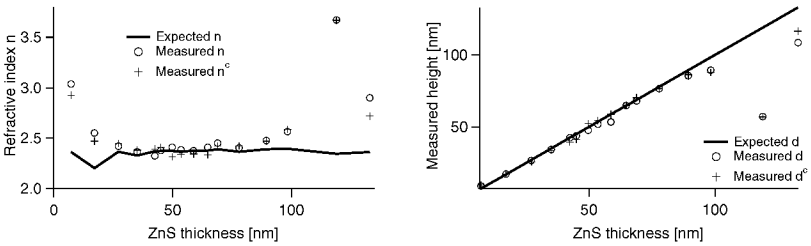

(c) n and d obtained by means of a 2D-fit to corrected Ψ and Δ.

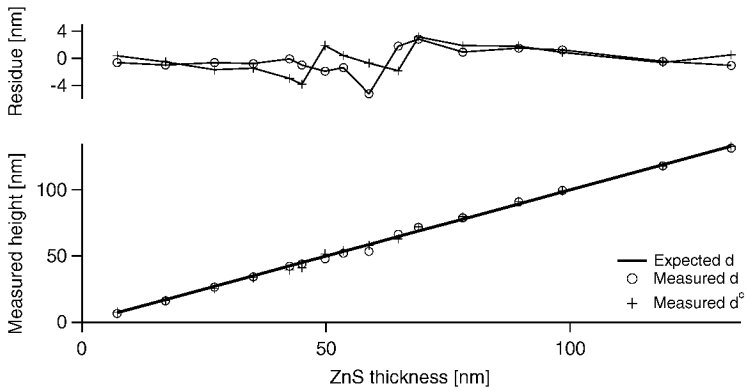

(d) $n = 2.379$ imposed and d retrieved by a 1D-fit to corrected Ψ and Δ.

Figure 6.6: Measurements at silicon wavers coated with layers of ZnS: $\Theta = 55.3°$, $P = \pm 30°$.

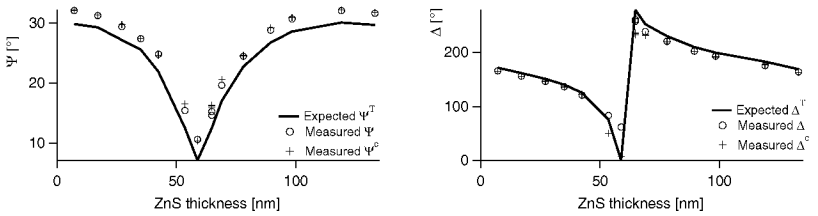

(a) Linearity corrected raw data.

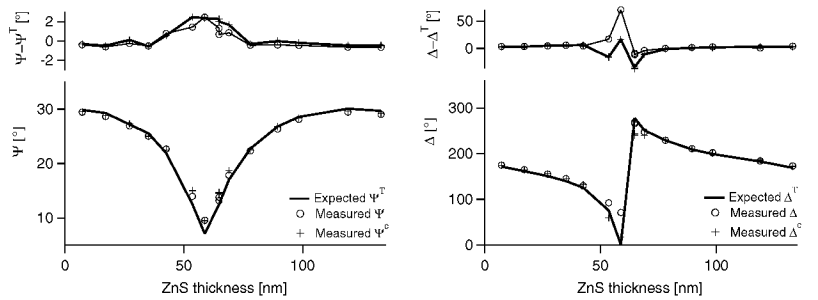

(b) Data corrected for instrumental polarization.

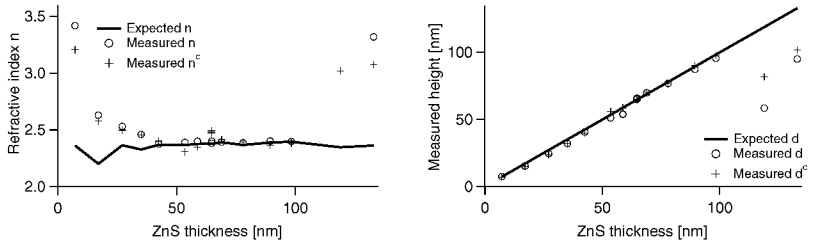

(c) n and d obtained by means of a 2D-fit to corrected Ψ and Δ.

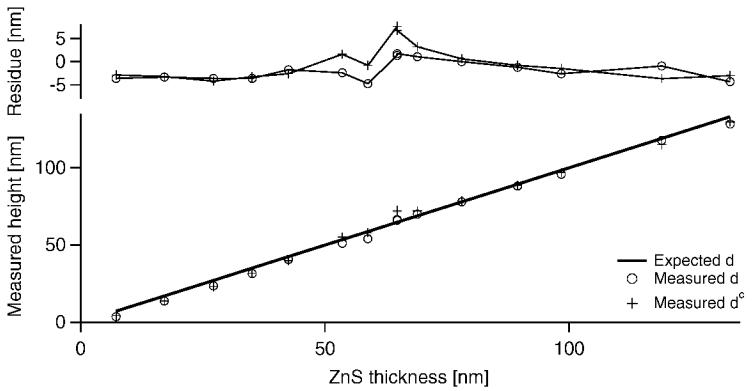

(d) $n = 2.379$ imposed and d retrieved by a 1D-fit to corrected Ψ and Δ.

Figure 6.7: Measurements at silicon wavers coated with layers of ZnS: $\Theta = 53.13°$, $P = \pm 45°$.

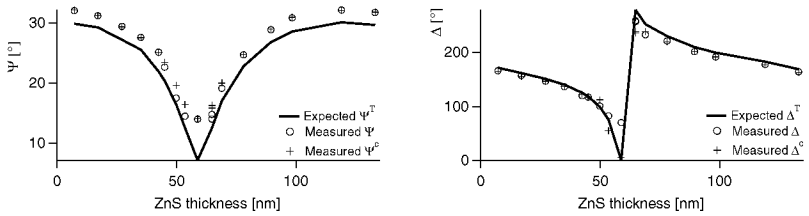

(a) Linearity corrected raw data.

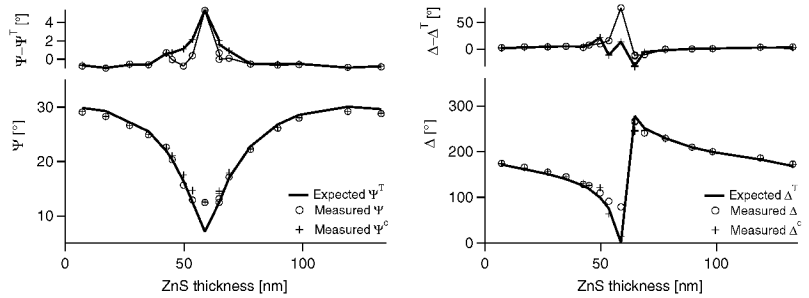

(b) Data corrected for instrumental polarization.

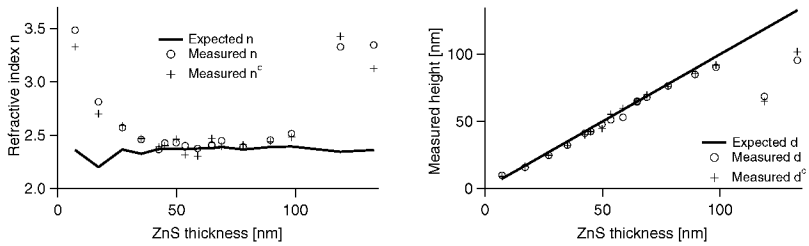

(c) n and d obtained by means of a 2D-fit to corrected Ψ and Δ.

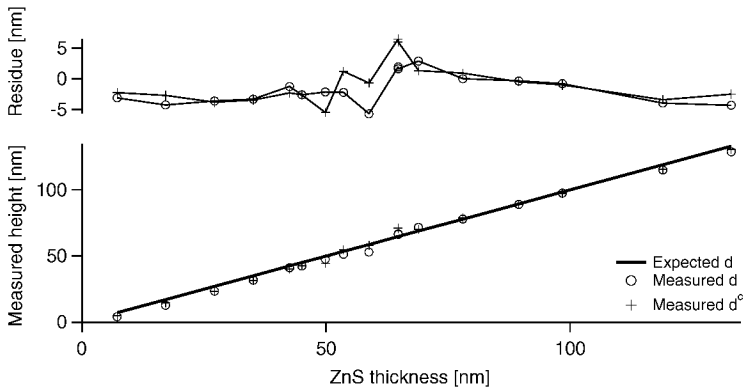

(d) $n = 2.379$ imposed and d retrieved by a 1D-fit to corrected Ψ and Δ.

Figure 6.8: Measurements at silicon wavers coated with layers of ZnS: $\Theta = 53.13°$, $P = \pm 30°$.

Material	Parameters	$\overline{\lvert\Delta d\rvert}$ [nm]	$\overline{\lvert\Delta d^c\rvert}$ [nm]
MgF_2	$\Theta = 55.31°$, P=45°	2.6	2.2
ZnS	$\Theta = 53.13°$, P=45°	2.4	3.0
ZnS	$\Theta = 55.31°$, P=45°	1.4	1.7
ZnS	$\Theta = 53.13°$, P=30°	2.6	2.7
ZnS	$\Theta = 55.31°$, P=30°	1.4	1.5

Table 6.2: Accuracy of the ellipsometric microscope when the refractive index is imposed (1D-fit): The average absolute deviation of the obtained thickness is better than 3 nm (cf. Figs 6.4(b), 6.5(d)-6.8(d)). Measurements with ($\overline{\lvert\Delta d^c\rvert}$) and without ($\overline{\lvert\Delta d\rvert}$) compensator show nearly the same accuracy.

Material	Parameters	$\overline{\lvert\Delta d\rvert}$ [nm]	$\overline{\lvert\Delta d^c\rvert}$ [nm]	$\overline{\lvert\Delta n\rvert}$	$\overline{\lvert\Delta n^c\rvert}$
MgF_2 (50-200 nm)	$\Theta = 55.31°$, P=45°	2.8	2.0	0.023	0.010
ZnS (20-100 nm)	$\Theta = 53.13°$, P=45°	2.1	1.5	0.037	0.062
ZnS (20-100 nm)	$\Theta = 55.31°$, P=45°	2.1	2.4	0.040	0.056
ZnS (20-100 nm)	$\Theta = 53.13°$, P=30°	2.6	2.4	0.063	0.077
ZnS (20-100 nm)	$\Theta = 55.31°$, P=30°	2.2	2.5	0.049	0.061

Table 6.3: Accuracy of the ellipsometric microscope when refractive index and thickness are obtained simultaneously (2D-fit): In the given thickness range the average absolute deviation of the obtained thickness is about 2.5 nm. Measurements with ($\overline{\lvert\Delta d^c\rvert}$) and without ($\overline{\lvert\Delta d\rvert}$) compensator show nearly the same accuracy. The refractive indices are determined with about 2.5% accuracy.

The results presented so far were based on laterally averaged intensities. In order to prove that indeed thicknesses can be measured accurately at every single pixel of the CCD camera Figure 6.9 shows a full-frame 3D-plot of the height topology obtained from two measurement of a MgF_2 sample at polarizer azimuths $P = +45°$ and $P = -45°$. For retrieval of zone averaged and instrumental polarization corrected Ψ- and Δ-pictures the recorded intensities were first corrected for the CCD nonlinearity. Afterwards Ψ- and Δ-images were computed for both polarizer settings. These images were zone averaged pixel wise. The resulting Ψ- and Δ-pictures were then corrected for instrumental polarization. Other processing was not applied. From these Ψ- and Δ-pictures the corresponding thickness map was obtained by means of a pixel wise 1D-fit with 75 nm height as starting value.

Figures 6.10(a)-6.11(b) show histograms of the thicknesses obtained pixel wise on laterally homogeneous areas. The corresponding areas are marked in Fig. 6.12(b). The distributions of the resulting thicknesses are usually extremely narrow (standard deviation ca 0.5 nm). Only thicknesses obtained from ellipsometric data without compensator and measured on uncovered regions exhibit a broader distribution (ca 2nm). This is due to the fact, that for this part of the sample Δ is close to 180°. Following Eq. (4.2) the error propagation law for Δ exhibits a singularity at $\sin\Delta = 0$. Thus, random fluctuations can have considerably greater influence close to $\Delta = 180°$. As indeed the standard deviation of Δ-values obtained from measurements

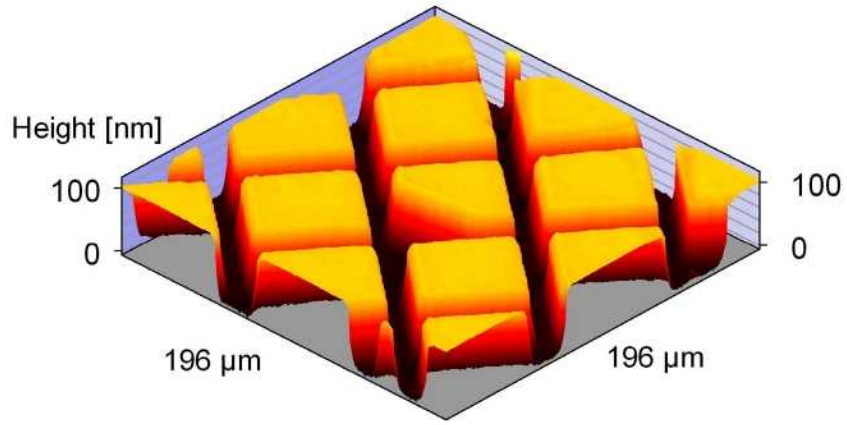

Figure 6.9: 3D-height-topology of a MgF_2 sample as obtained by ellipsometric microscopy. The incident angle was 55.31°. Histograms of heights obtained on homogeneous regions are shown in Figures 6.10 and 6.11.

without compensator is five times larger than the one from measurements with compensator ($\approx 0.20°$) the larger uncertainty of the resulting thickness can be explained.

Figures 6.10(a)-6.11(b) also show the thickness obtained from laterally averaged intensities (thick vertical bar). The intensities were averaged over the same regions used for determination of the histograms. Obviously these thicknesses do not coincide exactly with the means of the histograms. The absolute deviation is less than 0.5 nm and thus the difference is probably due to local intensity variations caused by Fresnel fringes created by small dust particles on the surface of optical components.

Finally, Figure 6.12 shows a comparison of an Scanning Force Microscope (SFM, Jeol JSPM-5200) measurement with the results obtained by ellipsometric microscopy. These measurements were done together with Robert Metzke (Zentralinstitut für Medizintechnik ZIMT, TU München). Figure 6.12(a) shows brightness encoded heights as plotted by the software of the manufacturer of the SFM. Extracting height profiles with nanometer accuracy from long scanning-range SFM-measurements is not an easy task: At the utilized scanning range of 60 μm nonlinearities and hysteresis-behavior of the piezoelectric devices [Meyer et al., 2004] introduce systematic parabolic deviations into the measured data. Such deviation can be compensated by image processing techniques [Bonnell, 2001] - nevertheless the accuracy of the absolute measured height is certainly only accurate to a few nanometers. Fortunately, the presented measurement exhibited only little distortion. Thus, besides from a simple "background subtraction" no further processing of the obtained data was necessary.

Figure 6.12 shows where profiles were extracted in order to allow for comparison with the data retrieved by ellipsometric microscopy. Figure 6.12(b) is a 3D-picture obtained by ellipsometric

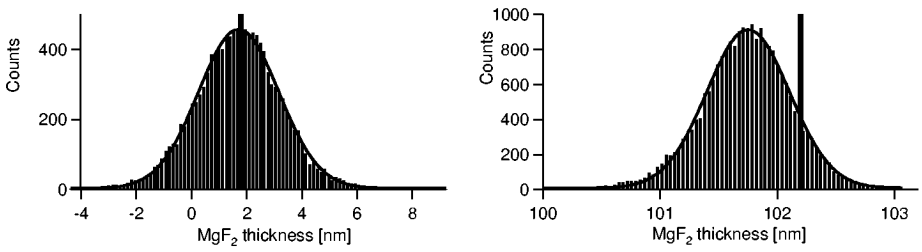

Figure 6.10: Histograms of heights - obtained at single pixels - within a rectangular region free of MgF_2 (a) and coated with MgF_2 (b). The corresponding rectangular regions are drawn in Fig. 6.12(b). The full topology of this sample was already presented in Fig. 6.9. A Gaussian fit to the histograms yielded a mean height of 1.7±2.1 nm and 101.8±0.50 nm, respectively. Note, that the given uncertainties represent the standard deviation of the height distribution and not of the mean height. The thicknesses computed from ellipsometric data, which was obtained by laterally averaging the intensities within the same region, are marked with a thick vertical bar. The small standard deviations of the shown histograms prove that there is no need for smoothing the data by laterally averaging.

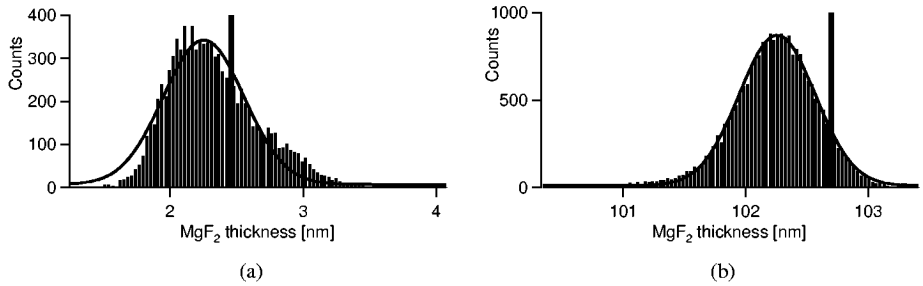

Figure 6.11: Same analysis as in Fig. 6.10 for heights obtained from ellipsometric data where the compensator was utilized. The mean heights are 2.25±0.43 nm and 102.3±0.44 nm, respectively. The given uncertainties represent the standard deviation of the height distribution.

microscopy of exactly the same location. Measuring exactly the same location was possible, because the masks used during MgF2-deposition (electron microscopy grids) have a single non-rectangular opening in their very center. Figures 6.12(c) and 6.12(d) show the comparison of line profiles extracted from SFM-measurements and ellipsometric microscopy. The results are in excellent agreement. Deviations on the right side of Figure 6.12(d) are due to the mentioned parabolic profile-problem inherent in long scanning-range SFM-measurements.

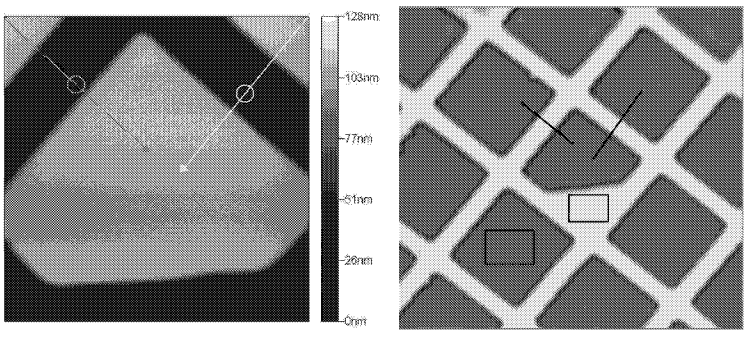

(a) (b)

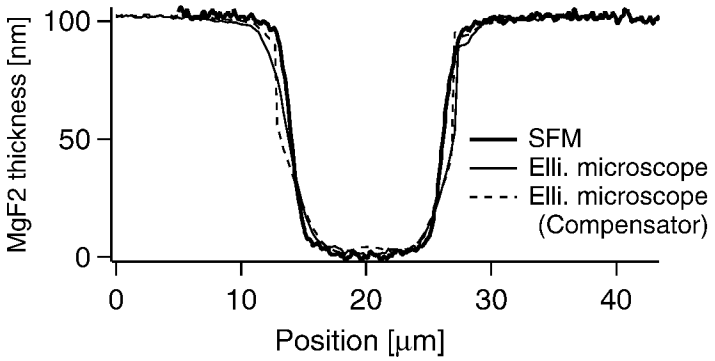

(c)

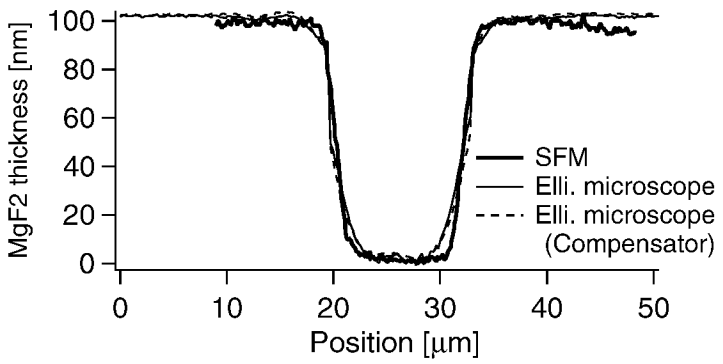

(d)

Figure 6.12: (a) Brightness encoded heights obtained from SFM-measurements. (b) Ellipsometric Δ-image of exactly the same region. The marked rectangular regions were used to evaluate the histograms shown in Figures 6.10 and 6.11. (c), (d) Comparison of the heights extracted along the left and right profiles shown in Figures (a) and (b).

6.2 Measurements on Glass Substrates I

6.2.1 Stray Light Correction Procedure

In this section first experiments at the glass-water interface are presented. To keep the system simple the bare glass-water interface itself was chosen as sample. Therefore standard microscope cover slides were mounted in a chamber which can be filled with fluids. In order to allow for angles of incidence as large as possible an oil immersion objective with a high numerical aperture (NA=1.4) is used for measurements at the glass-water interface. Therefore - unlike silicon substrates - the sample is illuminated through the substrate (see Fig. 6.14(a)).

Figure 6.13 shows measured Ψ and Δ values over a wide range of incident angles in comparison to theoretically expected values. The measured values were computed from linearized (compare to Section 6.1) and laterally averaged ($\approx 35 \times 35$ μm) intensities. In these and all other measurements presented here the polarizer was orientated at 45°. During these measurements the compensator was not yet built into the ellipsometric microscope. Therefore the Δ-values shown in Fig. 6.13 are not quadrant corrected. Obviously, ellipsometric angles calculated directly from raw data show little agreement with the expected values. This systematic deviation stems from partially polarized stray light due to internal reflections originating from the optical components constituting the setup.

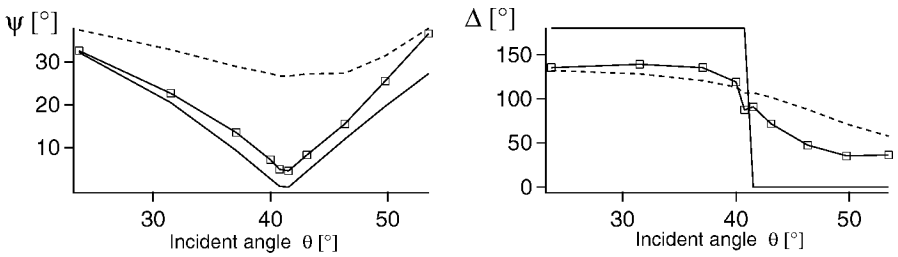

Figure 6.13: Measurements at the glass-water interface: Ψ and Δ are shown in dependence of the incident angle. Displayed are the values calculated from theory (continuous lines), from raw data (broken lines) and from stray light corrected images (squares connected by a line). At the Brewster angle Ψ is supposed to vanish. Δ should be 180° below and 0° above the Brewster angle.

To correct for this, pictures of the internal reflections were recorded for each azimuthal position A of the analyzer. This was done by mounting a 1 cm thick glass plate (BK7, n = 1.5187) with immersion oil to the objective (Fig. 6.14(b)). As the refractive indices of immersion oil and glass plate are matched this ensures that there is no light reflected at this interface and only the internal reflections created by the illuminating beam are recorded by the CCD camera. These pictures were made at all utilized incident angles and subtracted from the measured

data before computing Ψ and Δ values. Figure 6.15 shows the accompanying improvement in image quality very impressively.

All shown measurements were performed utilizing an immersion liquid optimized for fluorescence applications. This turned out to be important, because a focus dependence of the internal-reflection-images was noticed when ordinary immersion liquid was utilized. Obviously this was caused by a small amount of fluorescence of the ordinary immersion oil.

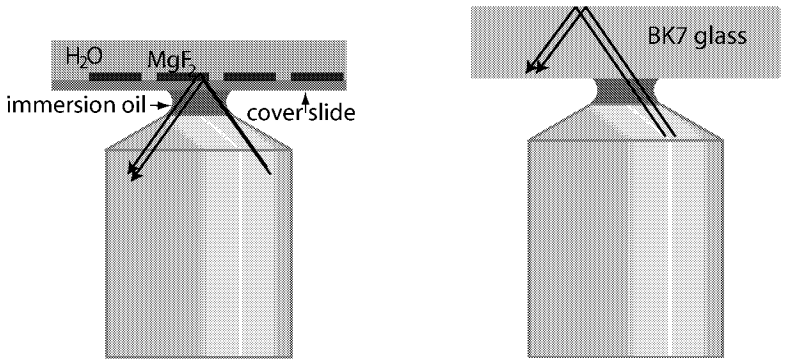

(a) Image recording (b) Recording of internal reflections

Figure 6.14: (a) Due to the small reflectivity of the sample raw data obtained by measurements are severely influenced by spurious stray light created at the optical components constituting the setup.
(b)In order to obtain images of these internal reflections a 1 cm thick BK7-glass plate with the same refractive index as the immersion oil was mounted to the microscope objective. This ensures that there is no light reflected at this interface and only the internal reflections created by the illuminating beam are recorded by the CCD camera. These pictures were made at all utilized incident angles and subtracted from the measured data before computing Ψ- and Δ pictures.

Background subtraction led to a significant improvement in Ψ (see Fig. 6.13). However, significant deviations remain. Especially the accuracy of Δ was barely improved by this procedure. In order to find out whether the remaining deviations can be attributed to failure of the background subtraction intensity traces $I(A)/I_0$ were analyzed at single pixels. Figure 6.16 shows typical single-pixel-traces of $I(A)/I_0$. At smaller angles of incidence the corrected intensity values $I(A)/I_0$ are in very good agreement with the expected curves. However, significant deviations appear at angles $\Theta > 50°$. While on silicon substrates stray light does not pose a problem, the signal to background ratio is much more demanding at the glass-water interface. Due to the decreased reflection coefficients the detected intensities are about 100 - 2500 times fainter. The underlying reason for this is the extremely small difference in refractive index between substrate (glass) and ambient medium (water).

The facts that Δ is almost unaffected by the stray light elimination (see Fig. 6.13) and that it

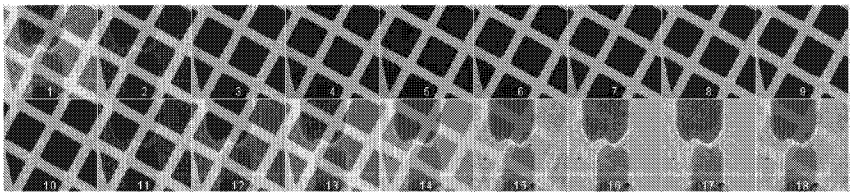

(a) Raw data.

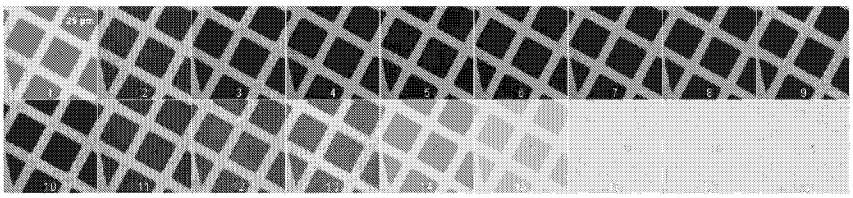

(b) Internal reflections subtracted from raw data.

Figure 6.15: Raw images of a 167.7 nm thick structured layer of MgF_2 at the glass-water interface at an incident angle of 49.6°. The MgF_2 deposition occurred only in the square structures, while regions covered by the electron microscopy grid were not coated. The images show raw data at 18 different analyzer positions A before (a) and after (b) subtraction of background light pictures. The analyzer angles are linearly spaced in the interval from 0° to 170°. The scale bar given in the first stray light corrected image applies to all images.

Figure 6.16: Intensity trace $I(A)$ at the glass-water interface for single pixels at four different incident angles: The thick line represents normalized traces from uncorrected raw data. The normalized and stray light corrected intensity (thin line) is compared to the theoretically expected dependence (broken line). While at smaller incident angles measurement and theory are in good agreement at higher incident angles the increasing amount of uncorrected stray light becomes apparent.

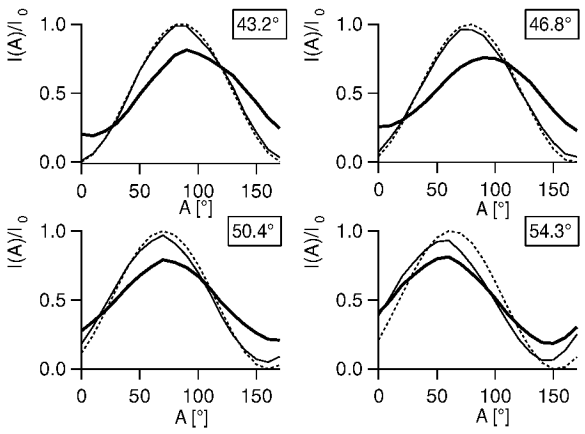

is computed erroneously despite very good agreement between the measured and calculated dependence of the intensity on the analyzer angle show that the Δ inaccuracies are inherent to the system under consideration: Considering Gaussian error propagation from the measured Fourier coefficients a and b to Δ shows that at $\Delta \approx 0°, 180°$ errors tend to diverge (cf. Eq. 4.2).

6.2.2 Measurements at Coated Cover Slides

The measurements presented in the previous section showed, that already the bare glass-water interface itself is a very difficult system for ellipsometry. In order to characterize the performance of the ellipsometric microscope when the Δ-value of the sample is different from $0°$ or $180°$ samples with a structured layer of MgF_2 on the cover slide (cf. Fig. 6.15) were created by vacuum deposition (cf. Section 5.1).

In the following all presented ellipsometric quantities were corrected for the nonlinearity of the CCD and the internal reflections within the microscope. In addition the ellipsometric values were zone averaged in order to avoid certain systematic errors (cf. Section 4.2). The steps necessary to achieve such corrections are:

1. Measure each sample at polarizer settings $\pm P$ (cf. Fig. 6.14(a)).
2. Take pictures of the internal reflections for each azimuthal position A of the analyzer and for both utilized polarizer settings $\pm P$ (cf. Fig. 6.14(b)).
3. Correct all four measured data sets for the nonlinearity of the CCD camera.
4. Subtract for each polarizer setting $\pm P$ the linearized stray light images from the linearized sample-measurements.
5. Compute for each polarizer setting $\pm P$ Ψ and Δ-values by laterally averaging the corrected intensities over homogeneous regions (ca 35×35 μm).
6. Compute zone averaged Ψ and Δ from the values obtained in the last step.

This procedure was performed for each sample at two polarizer settings $P = \pm 45°, \pm 30°$ and at two incident angles $\Theta = 46.6°, 50.1°$. The results obtained by the ellipsometric microscope are shown in Fig. 6.17. The thick continuous line represents theoretical data expected for the sample under consideration at the according incident angle. Measurements with and without compensator are marked by crosses and circles, respectively. The measured data agree qualitatively with the theoretical values. However, the data are very noisy and occasionally it was not possible to compute sensible Ψ- and Δ-values (data points at the level of the top broken horizontal lines). In particular it is impossible to obtain from these data reliable Ψ_{Obj}- and Δ_{Obj}-values in order to correct for the instrumental polarization of the imaging optics.

The susceptibility to failure of the glass-water-system becomes even more obvious when Ψ and Δ images are analyzed at single pixels. Figure 6.18 shows exemplary Ψ and Δ maps. In this figure white pixels correspond to undefined Ψ- and Δ-values. Not all measurements were

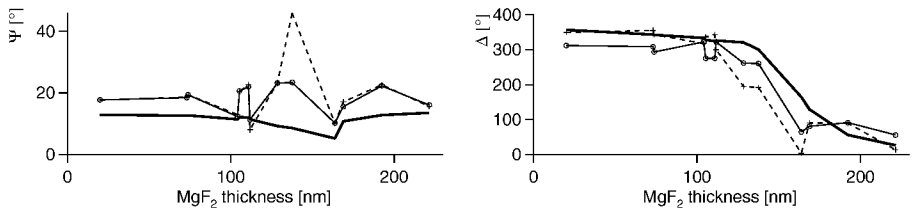

(a) Ψ and Δ measured at $\Theta = 46.6°$, $P = 45°$.

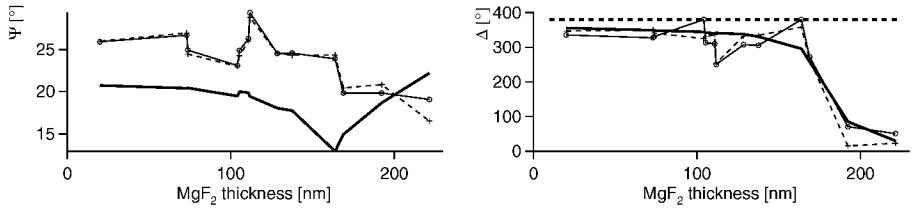

(b) Ψ and Δ measured at $\Theta = 50.1°$, $P = 45°$.

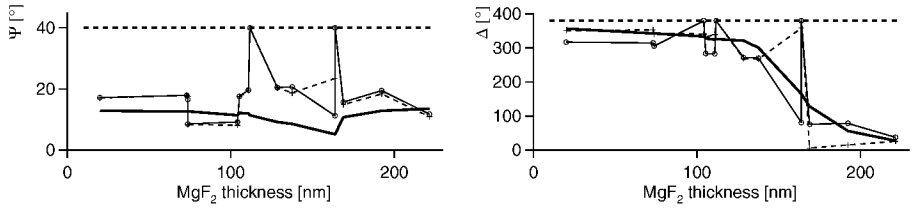

(c) Ψ and Δ measured at $\Theta = 46.6°$, $P = 30°$.

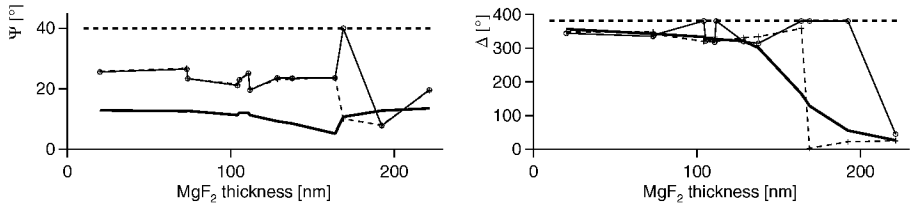

(d) Ψ and Δ measured at $\Theta = 50.1°$, $P = 30°$.

Figure 6.17: Measurements with (crosses) and without (circles) compensator at the glass-MgF_2-water interface: measured ellipsometric quantities in comparison to expected values (thick continuous line). Measurements were performed at incident angles $\Theta \in \{46.6°, 50.1°\}$ and at polarizer settings $P \in \{30°, 45°\}$. All shown data points are already zone averaged, corrected for internal reflections and nonlinearities. Nevertheless the data are very noisy and some data points (same level as thick broken horizontal line) did not compute to sensible values.

affected to the same degree - some measurements yielded much better results, others were even worse.

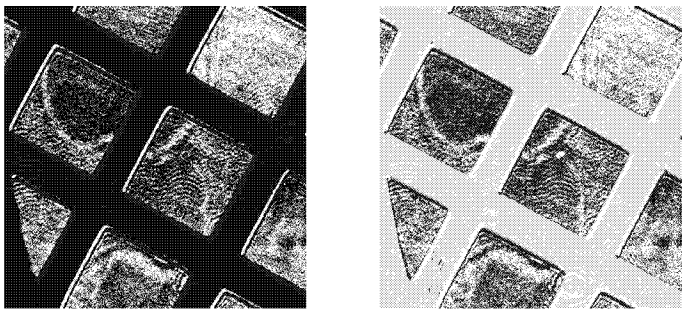

(a) (b)

Figure 6.18: (a) Ψ and (b) Δ images of a 167.7 nm thick structured layer of MgF_2 at the glass-water interface measured at an incident angle of 46.6°. White pixels correspond to locations where Ψ or Δ became complex and therefore unphysical.

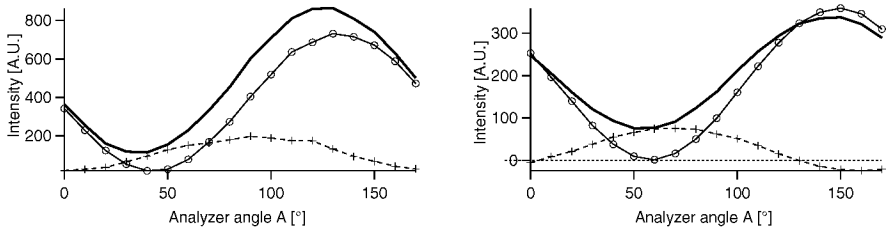

(a) (b)

Figure 6.19: Inadequacy of the stray light correction procedure: Shown are intensity traces $I(A)$ for covered glass substrates at single pixels. The thick lines represent normalized traces from linearized raw data. Data marked by circles represent traces obtained at the same location from an image of the internal reflections. The intensity originating from reflection at the sample is assumed to be the difference of both curves (crosses). In unfavorable cases the difference can even become negative (see Fig. (b))- which is unphysical. Sample data: (a) d=167.7 nm, $\Theta = 50.1°$, $P = 45°$ (b) d=111.8 nm, $\Theta = 46.6°$, $P = 30°$.

The reason for these difficulties is the further reduced signal to noise ratio: At the bare glass surface the reflectivity is very high in contrast to the almost black squares covered by MgF_2 (cf. Fig. 6.15). As all pictures were recorded avoiding pixel saturation the signal originating from the MgF_2 spots represents only a very small part of the dynamic range of the CCD camera. Moreover, the raw intensity at the MgF_2 covered regions is almost entirely dominated by stray light (cf. Fig. 6.19). Please note that in these regions stray light correction corresponds

to subtracting two intensities of nearly equal magnitude. Thus the comparatively small true signal is influenced strongly by the shot noise of the raw data and the background images. The stray light corrected intensity can even become negative (cf. Fig. 6.19(b)), which is unphysical.

6.3 Measurements on Glass Substrates II

6.3.1 Modified Setup

The fact that it was possible to retrieve excellent results on silicon substrates and the analysis of the last section lead to the conclusion, that the elimination of stray light is crucial in order to allow for accurate measurements at the glass-water interface. This stray light is created by internal reflections at the optical component constituting the setup - in spite of the fact, that all lenses are already compensated with anti-reflection coatings specialized to the employed wavelength ($\lambda = 546.1$ nm).

Therefore, it was necessary to find a way of blocking unwanted stray light. This was achieved by spatial filtering of the reflected light. The filtering aperture had to be integrated into the setup in such a way, that not too much spatial or ellipsometric information is lost. The appropriate location for such an aperture is within a plane where the light bundle carrying the ellipsometric information is focused, i.e. at planes conjugated to the back focal plane of the objective. The setup as shown in Fig. 3.1 accommodates two such planes: One is the back focal plane itself, the other is on a level with the image of the pinhole on the deflection mirror (DM). Unfortunately both planes are ineligible: The back focal plane is situated within the objective and therefore inaccessible. Placing an aperture in the other plane would block the illuminating beam.

Hence, the only option left was to create a new plane conjugated to the back focal plane by inserting a telescopic system before the CCD camera (cf. Fig. 6.20). This location has the additional advantage, that stray light is filtered very close to the detection unit. Note, that the position of this telescopic system is constrained by its constituting focal lengths and the focal length of lens 5: In order to obtain focused image formation the lens 6 has to be placed at distance $f_5 + f_6$ to lens 5. The chip of the CCD camera has to be at distance f_7 to lens 7.

In order to filter stray light while allowing light rays carrying ellipsometric information to pass, a pinhole has to be placed at the location of the common focal point of lenses 6 and 7. Because the sample is illuminated under a certain angle of incidence $\Theta \neq 0°$ the pinhole is not centered with respect to the optical axis: The center of the pinhole has to be at distance

$$h_{\mathrm{Ph}} = n_1 \cdot f_{\mathrm{Obj}} \cdot \sin\Theta \, \frac{f_3}{f_4} \frac{f_6}{f_5} \tag{6.4}$$

to the optical axis. This ensures, that at the surface reflected light rays, i.e. the part of the light bundle carrying the ellipsometric information, passes unhindered through the center of the pinhole. In order to maintain lateral resolution also a part of the light diffracted at the

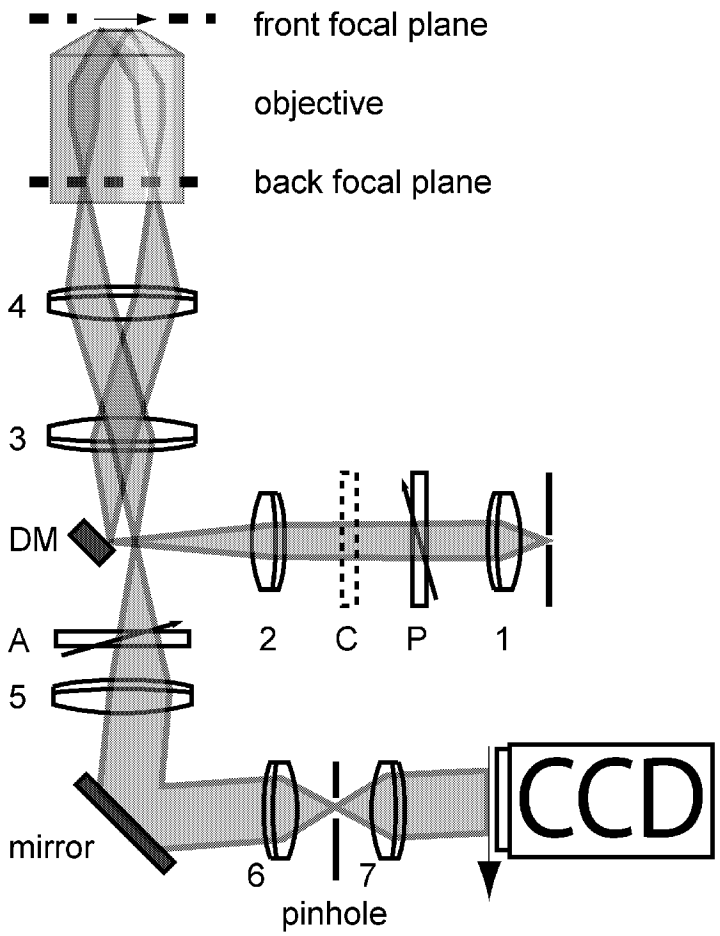

Figure 6.20: In order to allow for accurate ellipsometric measurements at the glass-water interface the setup had to be modified. Stray light caused by internal reflections is filtered by placing a stray light trap in front of the CCD camera.

sample must traverse the pinhole. Note, that the pinhole diameter D_{Ph} effectively limits the numerical aperture of the microscope and thus reduces its lateral resolution. This influence was investigated experimentally and the results are given in Section 6.4.3.

The idea of this stray light trap is relatively simple. The challenge lies in its experimental realization: In practice pinhole diameters ranging from 200 μm to 1 mm were utilized. At the location of the pinhole the image of the illuminating pinhole has a diameter of $D \cdot \frac{f_2}{f_1}\frac{f_6}{f_5} \approx 20\mu$m ($D = 50$ μm). For example: At an incident angle of $\Theta = 46.6°$ a 200 μm pinhole has to be

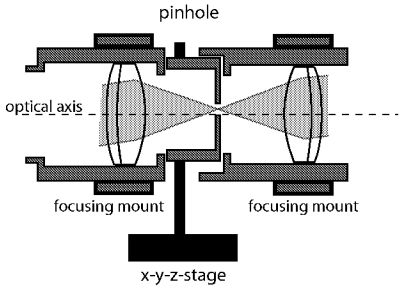

Figure 6.21: Experimental realization of the adjustable pinhole.

centered around a 20 μm spot located at 600 μm distance to the optical axis. In addition the pinhole has to be placed exactly centered with respect to lenses 6 and 7 in order to avoid vignetting. Thus, it is necessary to realize pinhole and lens mounts adjustable while still keeping all components encapsulated in order to prevent contamination with external stray light.

The pinhole is mounted to an x-y-z-positioning unit with micrometer screws (Fig. 6.21). Lenses 6 and 7 are mounted in focusing mounts (focusing mount C35, Linos, Göttingen), allowing for comfortable external positioning. Mounting the pinhole with a bit of tolerance into the neighboring mounting tubes prevents external stray light from entering.

In Figure 6.22 images of measurements with pinhole sizes of 200 μm and 1 mm are shown. For small pinhole sizes spurious reflexes are only visible at the very bottom. Because of the influence of the pinhole on the lateral resolution larger pinhole sizes would be favorable. Unfortunately, the region affected by stray light increases quadratically with the pinhole diameter. Subtraction of background images (obtained as described in Section 6.2.1) does not remove this artifact completely (Figures 6.22(b) and 6.22(d)).

For the 200 μm pinhole the region affected by spurious stray light is relatively small. Outside this region the reduction of internal stray light is remarkable: Traces through the background-to-signal ratio prove that it is completely removed (cf. Fig. 6.23). It can be estimated, that the residual intensities are due to the shot noise of the CCD camera. In praxis that means, that subtraction of internal-reflection images is not necessary anymore. The shown curves were obtained by dividing for each analyzer azimuth A images of the internal reflections, i.e. the background, through data measured at a sample. Because the intensity of the background-images frequently is zero the resulting images were laterally averaged (Gaussian with radius 12 pixels).

Having found an excellent method to eliminate stray light the next section proceeds by presenting ellipsometric measurements obtained with this modified setup.

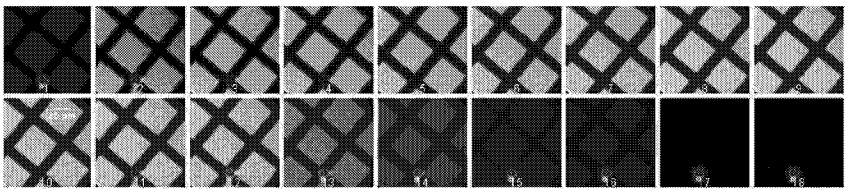

(a) Raw data acquired with a 200 μm stray light filtering pinhole.

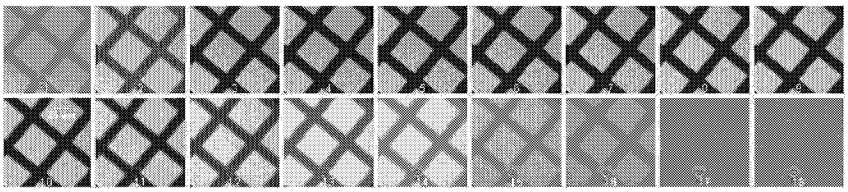

(b) Internal reflections subtracted from raw data (200 μm pinhole).

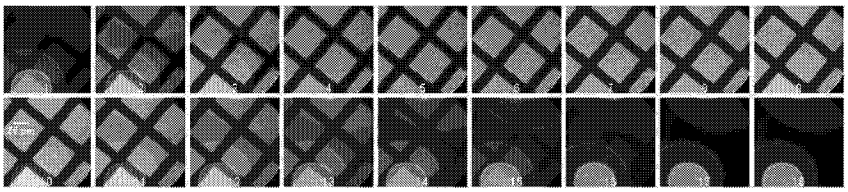

(c) Raw data acquired with a 1 mm stray light filtering pinhole.

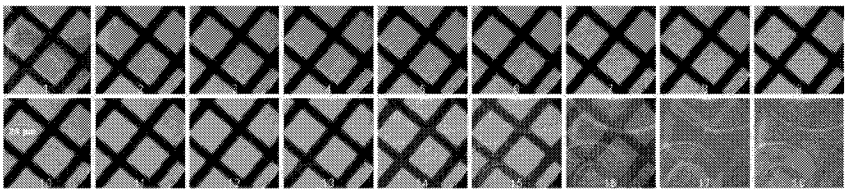

(d) Internal reflections subtracted from raw data (1 mm pinhole).

Figure 6.22: Influence of different stray light filtering pinhole sizes. (a) When a 200 μm pinhole is utilized the internal reflections are restricted to a relatively small region at the bottom of the images. The majority of the field of view is absolutely free of spurious stray light (see Fig. 6.23). (b) Unfortunately background subtraction cannot remove all artifacts. (c) Larger pinhole sizes would be favorable, because they have less effect on the lateral resolution. Unfortunately this enlarges the region affected by internal reflections greatly. (d) Again, background subtraction cannot remove all artifacts. All images were recorded at an incident angle $\Theta = 53.13^\circ$ and $P = 45^\circ$. The MgF_2 layer deposited on the cover slide had two different heights: 162 nm (grating) and 249 nm (plateaus).

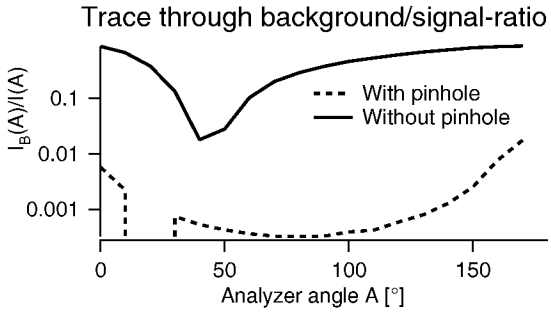

Figure 6.23: The stray light trap completely eliminates internal stray light: Shown are intensity traces $I_B(A)$ of internal reflection images divided by intensities $I(A)$ obtained from measurements at a sample. The broken line corresponds to measurements utilizing the stray light trap and is compared to data obtained from earlier measurements of the same sample (thick line).

6.3.2 Results on Glass

The addition of a pinhole (see modified setup in Fig. 6.20) suppressed stray light very effectively (see Fig. 6.23). Because of this, the procedure of comparing measured and theoretical expected ellipsometric quantities is identical to the procedure successfully applied to silicon substrates: The samples were measured at polarizer settings $P = \pm 45°$. From these measurements Ψ- and Δ- values were computed from intensities, which were linearized and laterally averaged over homogeneous regions (ca 35×35 μm). The resulting ellipsometric quantities were zone averaged in order to eliminate certain systematic errors to first order (see Section 4.2). These experimental data - obtained from measurements with and without compensator - were compared to theoretical data expected for the particular composition of planar stratified layers of each sample.

Figure 6.24(a) presents zone averaged and linearity corrected data in comparison to expected Ψ and Δ. Compared to measurements without stray light trap (see Fig. 6.17) the measured data are extremely smooth, but exhibits systematic deviations. These deviations can be attributed to instrumental polarization of the imaging optics.

This influence of the imaging optics on the polarization can be accounted for by applying the model developed in Section 6.1.1. Minimizing the sum Eq. (6.3) yields $\Psi_{Obj} = 49.0°$ and $\Delta_{Obj} = -11.6°$ for the correction parameters [2]. After correction for instrumental polarization the data are in very good agreement with expected data (Fig. 6.24(b)). Only in the region, where Ψ exhibits a minimum and Δ is discontinuous, the residuals become very large.

[2]Here data exhibiting large residuals (data points #9 and #10) were excluded from the minimization. This is justified as values of $\Psi < 5°$ cannot be measured accurately and Δ-values near the discontinuity depend strongly on small experimental errors (Θ, refractive index of water and small errors in the assumed layer thickness). For completeness the resulting values for inclusion of *all* data points are given: Ψ_{Obj}=49.30° and Δ_{Obj}= -13.11°.

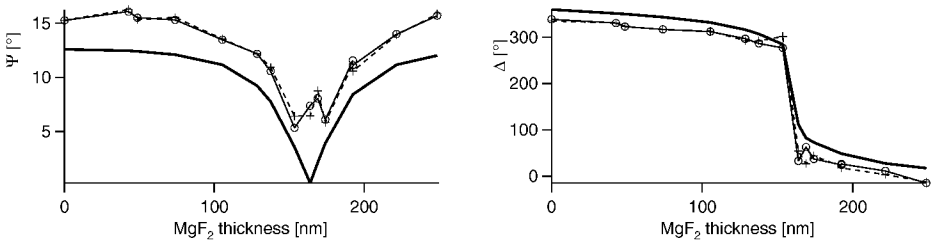

(a)

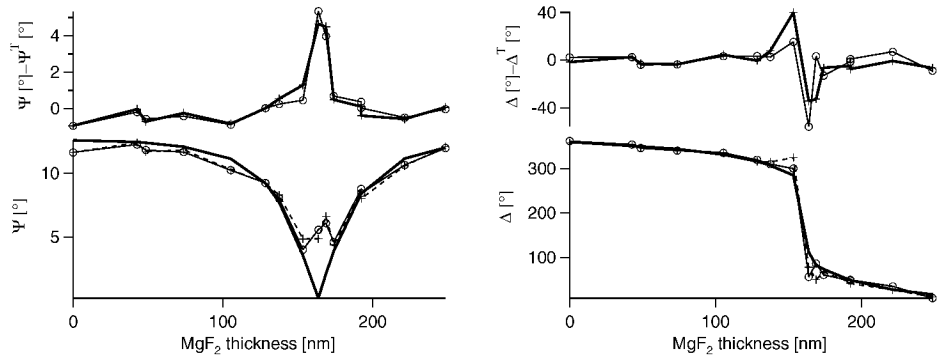

(b)

Figure 6.24: (a) Measured data - already linearized and zone averaged - in comparison to theoretical data (thick line). Measurements with (crosses) and without (circles) compensator are in excellent agreement, but exhibit systematic deviations to theoretical expected data.
(b) Correcting for instrumental polarization brings the measured data in excellent agreement with the expected data.

This can be explained by looking at the laws of error propagation (Eq. (4.1)-(4.4)). Near $\Psi \approx 0^\circ$ errors in $\delta\Psi$ and $\delta\Delta$ tend to diverge. Thus the ellipsometric quantities become extremely sensitive to small experimental errors. This kind of singularity is inherent to measurements with and without compensator.

Unfortunately this behavior cannot be avoided. Although it seems this singular behavior can be removed by measuring at the optimal polarizer setting $P_{\mathrm{Opt}} = \Psi$ (cf. Eq. (4.6)) this is not practicable. Following Eq. (2.14) the parallel reflection coefficient R_p is very small for samples with $\Psi \approx 0^\circ$. By setting P to a very small values, i.e. $P \approx \Psi$, most of the incident intensity is transmitted by the sample and not available for measurements. The already weakly reflecting sample would be measured under conditions where even less light is reflected at the sample.

Increasing the incident intensity, e.g. by using a laser as a light source, would probably not

allow for accurate determination of such small Ψ-values: At such small Ψ-values second order systematic errors become important and zone averaging becomes ineffective [Nijs and Silfhout, 1988].

6.3.3 Accuracy of Measurements at the Glass-Water Interface

Considering the difficulties the glass-water interface poses for ellipsometry, it is almost surprising how accurate Ψ and Δ can be determined with the presented setup. In terms of mean absolute deviations Ψ and Δ are determined accurate up to 0.41° and 4.3°, respectively [3]. In this respect the modified setup is almost equally accurate in determination of Ψ/Δ at the glass-water interface as on silicon substrates (cf. residuals of Ψ and Δ in Figures 6.3, 6.5(b) - 6.8(b)).

However, problematic is the fact, that the system under consideration does not exhibit great contrast in dependence of the deposited thickness of MgF_2: Ψ varies in the range of $[0.1^\circ, 12.6^\circ]$, but the region $[0^\circ, 5^\circ]$ poses serious experimental problems (cf. Section 6.3.2). The same holds for Δ which is very prone to systematic errors in the range of $[140, 175]$ nm. In the complementary thickness range Δ varies about 127°. Using a material with higher refractive index would result in a much higher ellipsometric contrast. MgF_2 was chosen because of its refractive index similarity with hydrated proteins or lipids ($n \approx 1.40 - 1.48$). These considerations led to the choice of one of the most demanding systems for ellipsometry.

Figure 6.25(a) shows the results obtained by fitting n and d simultaneously to the corrected ellipsometric data. At very small heights the obtained refractive indices and thicknesses can be very erroneous. Otherwise, the agreement is surprisingly good. Note that the largest measured thickness is still far away from the period D_Θ=326 nm (cf. Eq. (2.45)) of the ellipsometric quantities. Thus, a reduction of measurable quantities was not observed here (cf. Sections 2.2.4 and 6.1.2). Figure 6.25(b) presents the results obtained when the refractive index is imposed, i.e. the thicknesses were obtained by means of a 1D fit. The mean average deviation of the found quantities with respect to the expected values is summarized in Table 6.4. Refractive indices are found to be about 0.58 % accurate. Thicknesses can be obtained with an average accuracy of 10 nm. Both fits, 2D and 1D, are surprisingly stable with respect to the utilized starting value: Only the first data point shown in Fig. 6.25 varied when starting values far from the expected thicknesses were utilized.

In order to show, that retrieval of thicknesses is not only possible for ellipsometric quantities obtained from laterally averaged intensities, Fig. 6.26 presents full-frame Ψ- and Δ-maps. In addition a 3D-plot of the thicknesses obtained at single pixels is shown. The effect of residual stray light is clearly visible. Fortunately this artifact is restricted to a relatively small region at the very bottom of the images. Figure 6.27 shows histograms of thicknesses obtained at single pixels (with and without compensator) in comparison to thicknesses obtained from laterally

[3] Because of the large influence of systematic errors in the region $\Psi \approx 0^\circ$ the data points #8, #9 and #10 of Fig. 6.24(b) were omitted in this estimate. Thus, the mean absolute deviation was computed from 24 values for Ψ and Δ, each.

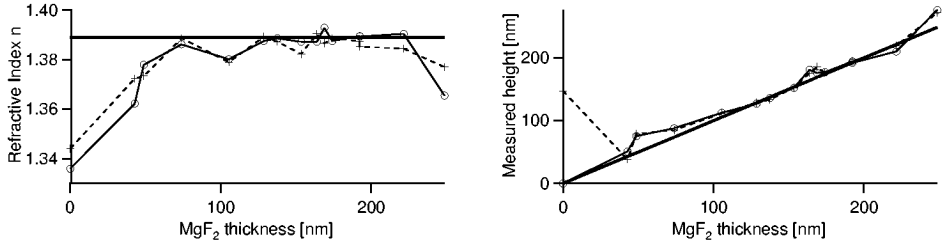

(a) 2D-fit

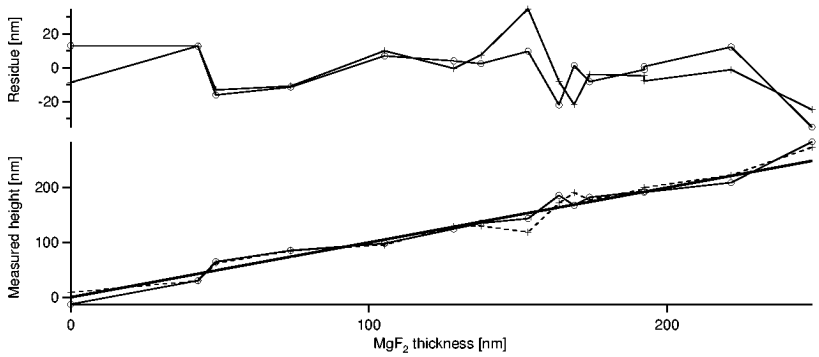

(b) 1D-fit

Figure 6.25: (a) Refractive indices and thicknesses simultaneously obtained by means of a 2D-fit from zone averaged ellipsometric data corrected for detector nonlinearities and instrumental polarization: Shown are data measured with (crosses) and without (circles) compensator. The thick line represents expected data. (b) Resulting thicknesses, if the refractive index of MgF_2 (n=1.389) is imposed.

		2D-fit		1D-fit
Material	Parameters	$\overline{\lvert \Delta d \rvert}$ [nm]	$\overline{\lvert \Delta n \rvert}$	$\overline{\lvert \Delta d \rvert}$ [nm]
MgF_2	Q = 46.6°, P=45°	8.8	$5.8 * 10^{-3}$	10.9

Table 6.4: Accuracy of the ellipsometric microscope at the glass-water interface. The average absolute deviation of the obtained thickness is about 10 nm. Because of its great proneness to errors the first data point of the graphs presented in Fig. 6.25 was excluded for computation of the mean absolute deviation.

averaged intensities (thick vertical bar). A Gaussian fit to the histograms yielded mean heights of 82.3±5 and 76.67±6 nm for thicknesses obtained from data measured with and without compensator, respectively.

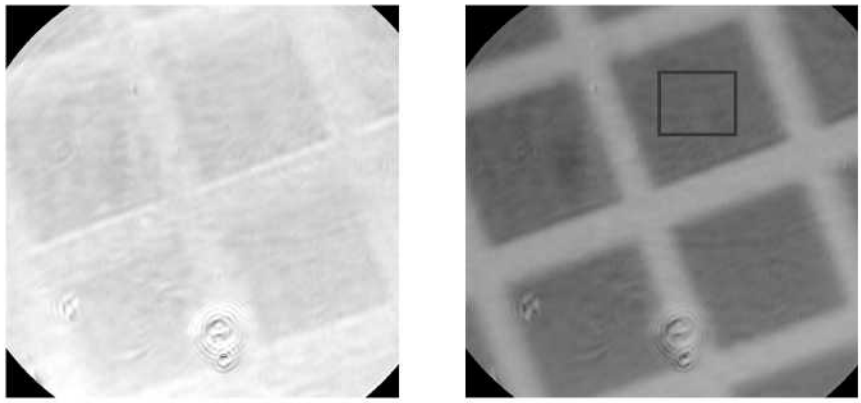

(a)

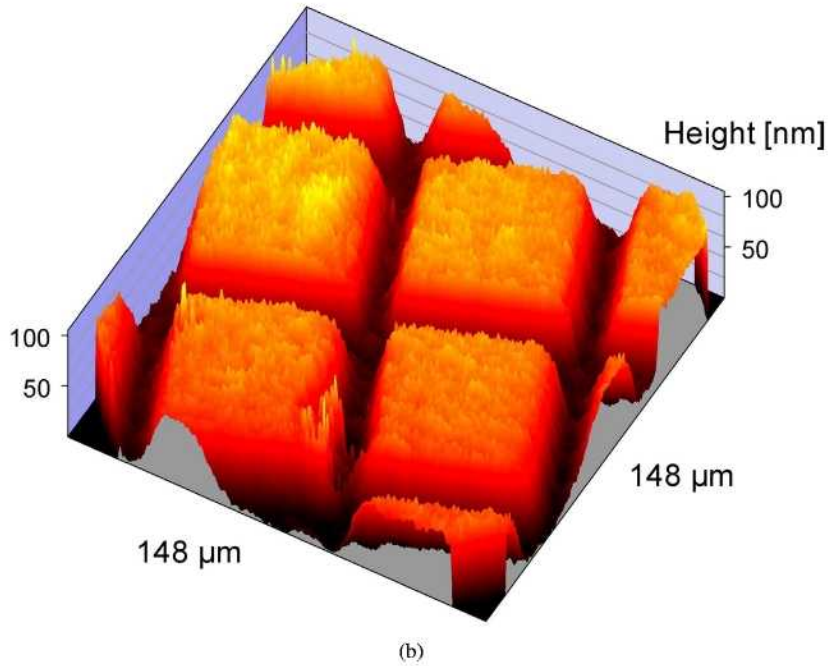

(b)

Figure 6.26: (a) Contrast enhanced images of `Y` (left) and `D` (right). The rectangle marks the region from which the histograms shown in Fig. 6.27 were obtained.
(b) 3D plot of the thicknesses obtained by means of a 1D-fit. The residual stray light reflex causes distortion of the obtained thicknesses. Fortunately this effect is restricted to a very small region.

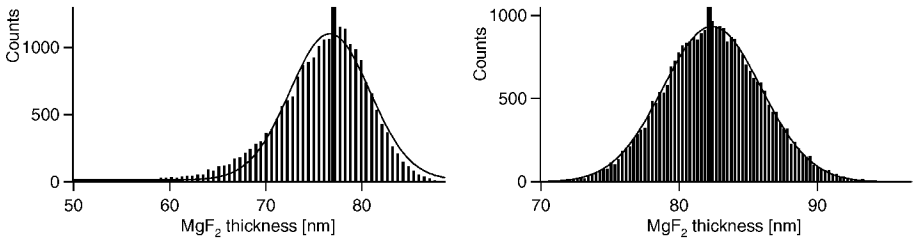

Figure 6.27: Histogram of the thicknesses within the rectangular region marked in Fig. 6.26(a). A Gaussian fit to the histogram of data obtained from measurements with (right) and without (left) compensator yielded mean heights of 82.3±5 and 76.67±6 nm, respectively. The vertical thick bars marks the thickness obtained by laterally averaging the intensities within the same region.

6.4 Lateral Resolution

In this section the lateral resolution of the ellipsometric microscope will be discussed. In order to determine the lateral resolution experimentally, edge diffraction patterns of structures on silicon wavers were analyzed (cf. Fig. 6.28). Structures with unresolvably sharp boundaries were obtained by reactive ion etching of thermally oxidized silicon wavers. To this end silicon wavers exhibiting a certain thickness of oxide were coated with a positive photo resist and structured by photolithography (UV, $\lambda = 365$ nm). After development of the photo resist only regions which were not exposed to UV light were still covered by resist. The subsequent etching process removed the oxide exclusively in regions not covered by the photo resist. An edge width of less than 0.2 μm was found by scanning electron microscopy on these structures. SEM measurements and wavers with structures of three different heights (25 nm, 103 nm, and 137 nm) were prepared and kindly provided by Claudia Cesa from the Research Centre Jülich.

Because the sample is illuminated under a certain angle of incidence it is expected, that the lateral resolution depends on the spatial direction (see Section 2.3.3). In Fig. 6.29 profiles across structures parallel (thick continuous line in (a), (b)) and perpendicular (crosses in (a), (c)) to the plane of incidence are shown. In order to obtain the measured diffraction patterns with higher signal-to-noise ratio the profiles were laterally averaged (29 μm, 151 pixels) in a direction perpendicular to the drawn line profile.

Profiles obtained from structures perpendicular to the plane of incidence show considerably more edge ringing than those acquired from structures parallel to it. Moreover, the diffraction patterns measured at structures parallel to the plane of incidence seem to be slightly narrower than those derived from parallel structures.

These results were also predicted by the scalar theory of diffraction presented in Section 2.3.3. Otherwise the measured curves show little agreement with the theoretically computed diffraction patterns. The reason for this is twofold: Firstly, the presented scalar diffraction theory

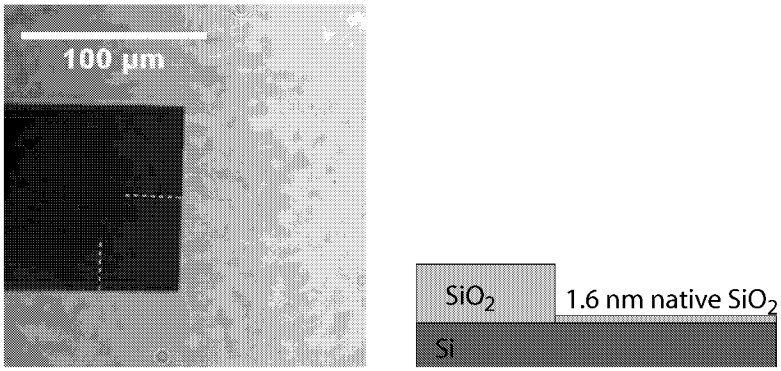

Figure 6.28: (a) Image of a typical SiO_2-structure used to determine the lateral resolution of the ellipsometric microscope. The black region corresponds to a SiO_2 plateau of 103 nm height. The sample is illuminated under an angle of incidence ($\Theta = 53.13°$) and it is expected, that the resolution depends on the spatial direction (see Section 2.3.3). The broken lines mark the locations of the profiles shown in Fig. 6.29. The vertical profile is parallel to the projection of the plane of incidence into the image plane. (b) The sketch shows the layer system of the samples under consideration. Silicon wavers are always covered with a thin layer of native SiO_2.

was only valid for paraxial optics, i.e. for imaging systems with low numerical aperture. Secondly, the scalar model completely neglects the vectorial nature of the light, i.e. the direction of energy flow (Poynting vector) and the state of polarization[4].

It shall be mentioned, that other effects affect the spatial dependence of the lateral resolution of ellipsometric microscopy, too, e.g. depolarization of edge-diffracted waves. Edges parallel and perpendicular to the incident field, i.e. parallel to the diagonals in Fig. 6.28(a), are expected to not affect the polarization direction of the incident field [Kimura and Wilson, 1994].

[4]An accurate description of diffraction phenomena in the case of polarized light, high aperture systems and diffracting objects smaller than λ can become very complicated. Any application of a diffraction model can be separated into two steps: First, an accurate description of the near fields exiting the diffracting object and secondly the propagation of those fields. In the simple scalar diffraction model presented in Section 2.3.3 the near field of an edge was approximated with a Heaviside unit function - which is certainly not a self-consistent solution of the Maxwell equations for this given boundary problem. Thus, it is difficult to identify the cause for deviations between theory and experimental data: inaccurate initial near field data, or application of a limited propagation model.
One diffraction (propagation) model including the vectorial nature of the light can be found in Richards and Wolf [1959], Wolf [1959]. This model is frequently used and can be interpreted in terms of a modified Huygens-Fresnel principle: Wave fronts are regarded as centres of secondary disturbances of plane waves. It is frequently utilized to describe optical disk readout [Cheng et al., 2000] but also has been utilized in the context of imaging ellipsometry [Zhan and Leger, 2002a] in order to simulate the signal obtained with a high aperture microspot ellipsometer (see Section 1.1). For the microspot technique, where a beam of polarized light is focused onto the sample, such modeling is - in contrary to the approach followed here - of utter importance for the technique itself.

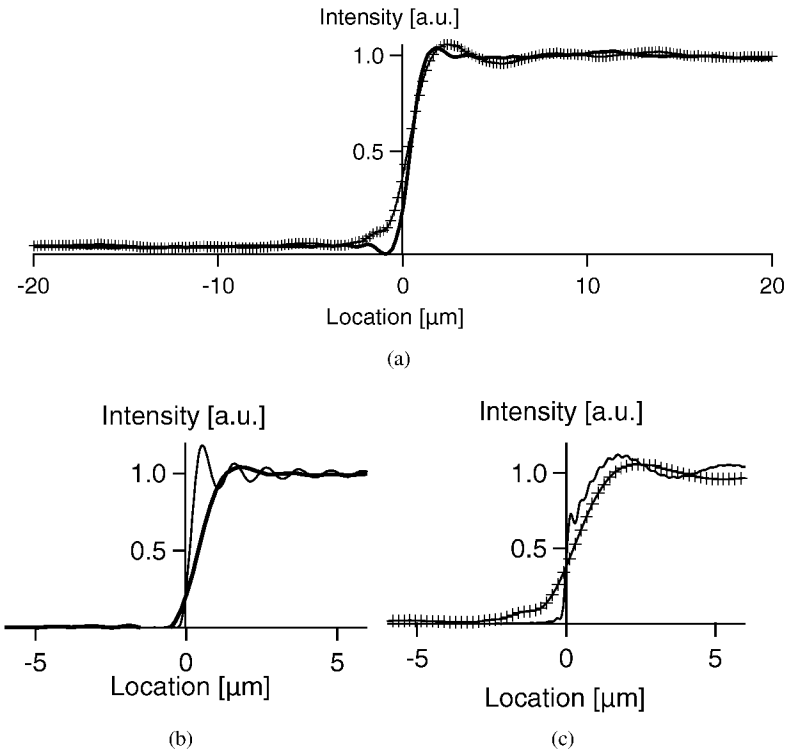

Figure 6.29: Figure (a) shows profiles of edge structures (103 nm SiO_2, cf. Fig. 6.28) parallel (thick continuous line) and perpendicular (crosses) to the plane of incidence. The polarizer azimuths were $P = 45°$ and $A = 110°$. The transition region is presented enlarged in Figures (b) and (c) for parallel and perpendicular structures, respectively. In addition the theoretical curves (thin continuous line) for unpolarized light (NA=0.95, $\Theta = 53.13°$, $\lambda = 546.1$ nm, cf. Section 2.3.3) are shown. The curves considerably disagree and the limitations (low aperture systems, unpolarized light) of the simple scalar diffraction theory become apparent.

Another closely related phenomenon is the appearance of edge birefringence, that appears near boundaries of objects with different refractive indices. This effect was studied by Oldenbourg [1991] by means of a polarization ray-tracing model. As all these effects affect the spatial dependence of the lateral resolution to a similar extent. It is difficult to separate their influence on basis of the data acquired with the ellipsometric microscope.

In order to show the extend of depolarization at edge structures Fig. 6.30 presents exemplary Ψ/Δ-Profiles drawn over edges (103 nm height) parallel and perpendicular to the plane of incidence. In order to show the diffraction effects with higher signal-to-noise ratio these profiles were obtained by laterally averaging single-pixel Ψ/Δ-values in a direction perpendicular to

the line profile. Clearly, the edge ringing of the intensities propagates to Ψ and Δ. The affected region exhibits the same extent as observed for the intensities.

Figure 6.30 also shows height profiles obtained from such Ψ/Δ-profiles. In order to see height dependent resolution effects three samples with different heights were measured. Although edge-depolarization can lead to artifacts in the determined height profiles - especially for high edge-structures (see 137 nm profile in Figures 6.30(c), 6.30(d), 6.30(g) and 6.30(h)) - it appears, that the transition region of the height profiles is considerably narrower. This is especially apparent for height profiles determined from ellipsometric measurements with utilized compensator. Also edge ringing is less pronounced compared to Ψ/Δ profiles.

So far only the extent of the transition region has been discussed. This extent is not a fair variable for comparison with typical resolution specifications given frequently in terms of the Rayleigh criterion (see Section 2.3.2). The next section will present the concept of the modulation transfer function. This concept will be used in order to analyze the lateral resolution of the ellipsometric microscope in a more comparable fashion to usual resolution specification, given in terms of the Rayleigh criterion.

6.4.1 The Modulation Transfer Function MTF

When a certain value is given for the lateral resolution of an imaging system it is critical to note, that this usually does not mean, that details beyond this limit cannot be resolved. In reality the contrast of the image of a periodic structure decreases with the spatial frequency of its period (see Fig. 6.31). The relation between image contrast

$$C(k) = \frac{I_{\max} - I_{\min}}{I_{\max} + I_{\min}}$$

and the corresponding spatial frequency k of the object is thereby called *modulation transfer function* [Pluta, 1989a].

In the case of incoherent imaging the modulation transfer function can be related to the point spread function of the imaging system: Similar to Eq. (2.47) image formation $I'(x',y')$ can be described as a convolution of the object intensity $I(x,y)$) and the point spread function

$$I'(x',y') = I(x,y) \star \mathrm{PSF}(x,y). \tag{6.5}$$

The symbol $\star$ denotes the convolution operation. By transforming this equation into the Fourier space and utilizing the convolution theorem the relation between modulation transfer function $\mathrm{MTF}(k_x,k_y)$ becomes apparent:

$$\mathrm{MTF}(k_x,k_y) = |\mathrm{OTF}(k_x,k_y)| = \left| \frac{\mathscr{F}(I'(x',y'))}{\mathscr{F}(I(x,y))} \right| = |\mathscr{F}(\mathrm{PSF}(x,y))|, \tag{6.6}$$

where the symbol $\mathscr{F}$ denotes the Fourier transformation. The MTF is the modulus of the optical transfer function $\mathrm{OTF}(k,k_y)$ which describes the ratio of the image and the object frequency spectra. Thus, a low value of the MTF means that the corresponding spatial frequency

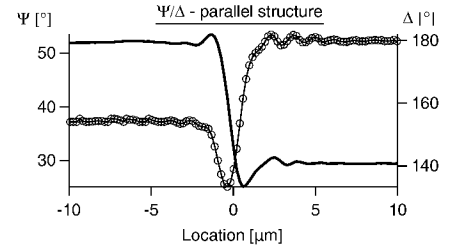

(a) Ψ/Δ (parallel) of 103 nm sample

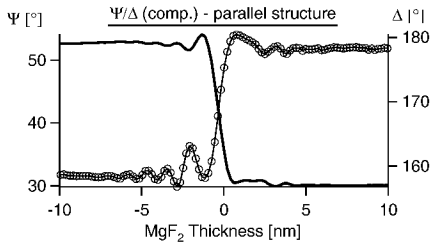

(b) Ψ/Δ (parallel, comp.) of 103 nm sample

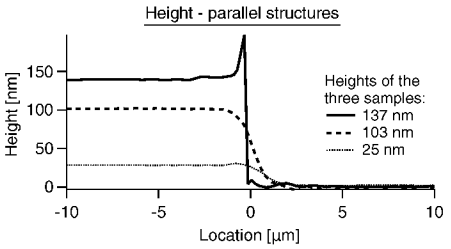

(c) Heights in the transition region

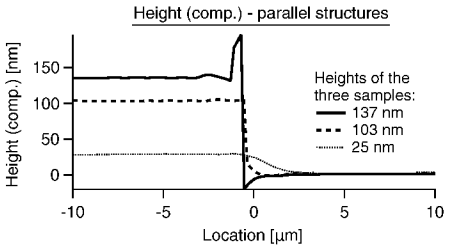

(d) Heights (comp.) in the transition region

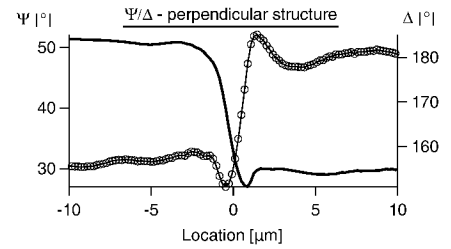

(e) Ψ/Δ (perp.) of 103 nm sample

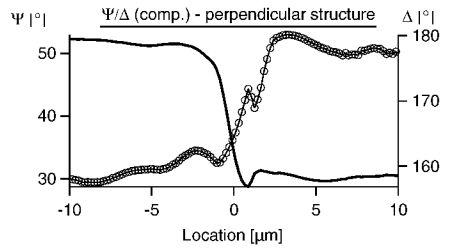

(f) Ψ/Δ (perp., comp.) of 103 nm sample

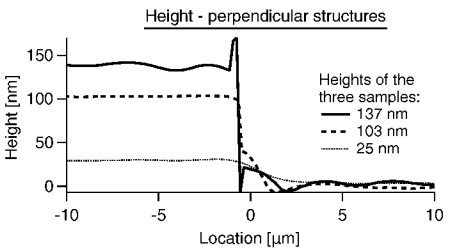

(g) Heights in the transition region

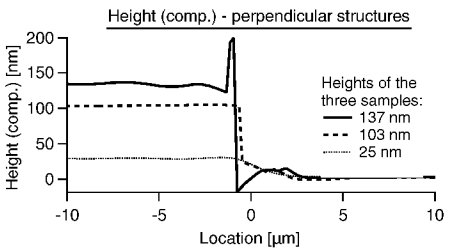

(h) Heights (comp.) in the transition region

Figure 6.30: Shown are Ψ/Δ- and height profiles of edge structures. Δ values are marked by circles. Edge ringing is also present in Ψ/Δ profiles and is considerably more pronounced for structures perpendicular to the plane of incidence. The extents of the transition regions are approximately the same for three samples with different heights ($\approx$2 μm for parallel and $\approx$2.5μm for perpendicular structures). Depolarization at the edges leads to spurious Ψ/Δ values and hence to erroneous heights. Note that this is restricted to a very narrow region.

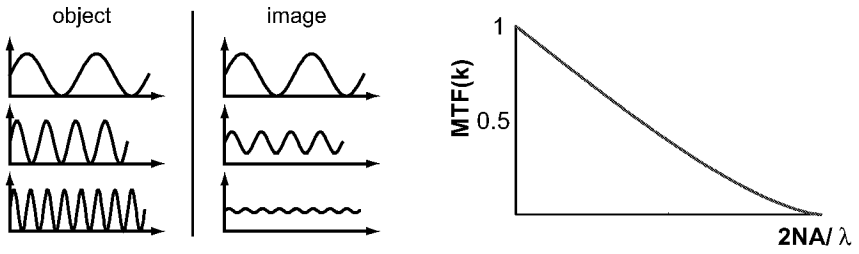

Figure 6.31: Concept of the modulation transfer function: higher spatial frequencies are reproduced with less contrast.

is barely transfered by the system. The corresponding image intensity variations have little contrast (see Fig. 6.31).

Similar relations can be derived for the case of coherent imaging: All considerations correspond then to optical disturbances, i.e. the electrical field of the light, instead of intensities. The MTF and the PSF are replaced by the *amplitude transfer function* and the amplitude point spread function (see Section 2.3.2), respectively [Reynolds et al., 1989].

As the MTF is defined as the modulus of two intensity spectra (cf. Eq. 6.6) it is - in contrary to the amplitude transfer function - accessibly to direct measurement. One standardized method will be presented in the next Section.

6.4.2 Measuring the MTF: the Knife-Edge Method

The procedure for measuring the MTF is outlined in ISO 12233. The method is known as the "knife-edge method" and represents a method for determination of the MTF in one direction only. It relies on one-dimensional measurements of a line profile over a step-like structure (see Fig. 6.32). The resulting profile is the result of the convolution of the object intensity with the line spread function LSF. The LSF is related to the PSF by

$$\mathrm{LSF}(x) = \int_{-\infty}^{\infty} dy\, \mathrm{PSF}(x,y), \tag{6.7}$$

i.e. the second dimension of the PSF is eliminated by integration. By differentiating the measured edge profile numerically one obtains the LSF of the imaging system (cf. Fig. 6.32). Analogous to Eq. (6.6) the MTF is then obtained by a Fourier transformation:

$$\mathrm{MTF}(k) = |\mathscr{F}(\mathrm{LSF}(x))|. \tag{6.8}$$

The procedure is outlined in Fig. 6.33. The spatial frequency, where the MTF drops below a value of 0.1 is identical to the one found by the Rayleigh criterion (cf. Section 2.3.2) [Williams and Burns, 2001].

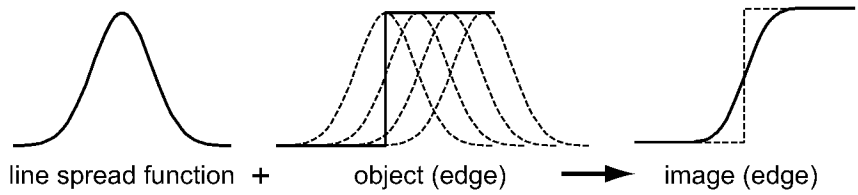

Figure 6.32: Determining the line spread function from a measured edge profile: The edge profile is the result of the convolution of the line spread function with the object irradiance. Thus, a simple differentiation of the measured profile yields the LSF.

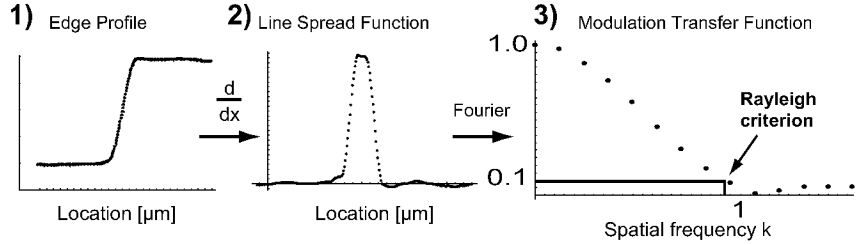

Figure 6.33: Determination of the MTF from a measured edge profile. The spatial frequency, where the MTF drops first below a value of 0.1 can be related to the Rayleigh resolution criterion.

It is important to note here, that this procedure is strictly only valid for incoherent imaging. In ellipsometric microscopy the object is illuminated coherently, because of the small illumination aperture (see Section 4.6). The question is whether this scheme is nevertheless applicable in the case of coherent imaging.

The problem is, that in the case of coherent imaging the concept of an intensity line spread function is strictly speaking ill-defined. Image formation cannot be described by convolution on basis of intensities. Such a procedure is only possible on level of the strength of the electrical fields, but those are inaccessible to direct measurement. Thus, differentiation of the edge profile does not yield the line spread function - it yields something which is by intuition closely related. Hence it is questionable if Eq. 6.8 yields a sensible result.

It is therefore instructive to reflect the definition of the MTF (Eq. 6.6) once more: It is defined as the modulus of the image frequency spectrum normalized to the object frequency spectrum. In our case we consider edge-structures, which can be modeled by use of the Heaviside unit function $U(x)$. Computing the frequency spectrum of this object structure

$$\mathcal{F}(U(x)) = \frac{1}{ik} + \pi\delta(k) \tag{6.9}$$

it becomes apparent, that such a structure is - apart from $k \approx 0$ - continuous in frequency, i.e. it is composed of all possible frequencies. Measuring now the frequencies which are trans-

fered to the image space by computing $\mathcal{F}(I'(x'))$ and normalizing this result to the incident spectrum $\mathcal{F}(U(x))$ yields the MTF:

$$\mathrm{MTF}(k) = \left|\frac{\mathcal{F}(I'(x'))}{\mathcal{F}(U(x))}\right| = \left|\frac{\mathcal{F}(I'(x'))}{\frac{1}{ik}+\pi\delta(k)}\right| \overset{k\neq 0}{=} \mathcal{F}\left(\frac{d}{dx'}I'(x')\right) \tag{6.10}$$

In the last equality it has been used, that a multiplication in frequency space corresponds to a spatial differentiation. This is mathematically the same procedure for determination of the MTF as outlined previously for the case of incoherent imaging: The line profile has to be differentiated and by Fourier transformation of this result one obtains the MTF. Thus, it is apparent that the MTF is not inevitably connected to the LSF - it is a concept which can be generalized to coherent imaging.

For determination of the lateral resolution edge profiles as shown in Figures 6.29 and 6.30 were extracted from three different samples (25 nm, 103 nm, and 137 nm). Analyzed were intensity, Ψ, Δ and height profiles. Each of these profiles was extracted from measurements with and without the compensator and parallel and perpendicular to the plane of incidence. Altogether 48 profiles were analyzed. In order to measure the diffraction patterns with a high signal-to-noise ratio the intensity and Ψ/Δ profiles were averaged perpendicularly to the profile direction (151 pixels, 29 μm). The height profiles were obtained from the averaged Ψ/Δ profiles.

As one pixel corresponds to 0.191 μm in object space, sampling of the profiles proceeded beyond the Nyquist limit of the smallest structures expected to be still observable. Because the height profiles can obtain discontinuities it was necessary to apply averaging filters to the raw profiles: The sharp transition of the heights in combination with the spurious over- or undershooting of the obtained height profiles (see 137 nm profile in Fig. 6.30) would lead to a spurious amplification of high frequencies, and thus to an overestimation of the resolution. That is why to *all* profiles a moving median and a moving average filter with kernel size 5 was applied[5]. The median filter removes outliers, i.e. the over- and undershooting artifacts, and the successive moving average smears out the discontinuities. For more details to the properties of these filters see Section 5.5. The kernel size 5 was chosen, because it corresponds to a length still below the expected resolution. Fig. 6.34 exemplary shows that the applied averaging and filtering procedure has little influence on the obtained lateral resolution.

The resulting profiles were then differentiated. A central difference scheme [Press et al., 1986] was applied to interior points, a forward and a backward difference scheme to the first and last point, respectively. In order to avoid frequency leakage due to finite window size the data were multiplied by a Bartlett window [Press et al., 1986] before performing a discrete Fourier transformation. This helps to get a smoother estimate of the frequency spectrum. The resulting

[5] Application of averaging filters, when one is concerned about resolution, is an unconventional procedure. As mentioned, this is strictly speaking only necessary for discontinuous height profiles. The much smoother intensity profiles would not demand such measures. In order to keep the results obtained from different quantities (intensity, Ψ/Δ, height) comparable averaging was applied to all profiles. However, Fig. 6.34 shows, that for the intensity profiles the averaging procedure has little influence on the obtained lateral resolution.

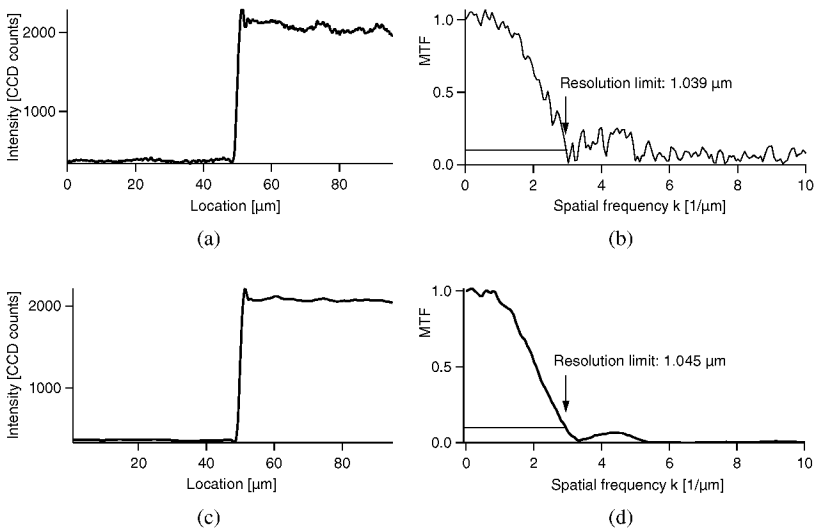

Figure 6.34: Influence of the utilized averaging procedure: (a) presents a raw intensity profile (width: 1 pixel, 103 nm SiO_2, $\Theta = 53.13°$, $P = 45°$, $A = 110°$, parallel to the plane of incidence) and in Fig. (b) the resulting MTF is given. Fig. (c) shows the averaged profile (width: 151 pixels, moving median and average filter with kernel size 5). The resulting MTF (d) is considerably smoother, but the actual resolution limit did not change.

MTF was then scanned for the spatial frequency k_c where it first droped below a value of 0.1. By usage of the Nyquist sampling theorem [Press et al., 1986] this cut-off frequency can be related to a spatial resolution:

$$\Delta x \approx \frac{\pi}{k_c}. \tag{6.11}$$

Fig. 6.35 shows exemplary the results of all intermediate steps for a discontinuous height profile. The cut-off frequency found in this spectrum corresponds to a lateral resolution of 0.5 μm.

Figure 6.36 summarizes the findings for all 48 analyzed line profiles. The lateral resolution found in each category (intensity, Ψ, Δ and height) is shown. The data represents maximum values found for the three different sample heights. Considering the very conservative manner in which these values were obtained it seems plausible to estimate the lateral resolution limit for structures parallel to the plane of incidence to about 1 μm. For structures perpendicular to the plane of incidence the resolution limit is 1.7 μm. The sample can always be rotated in order to resolve the structures of interest with a resolution of 1 μm.

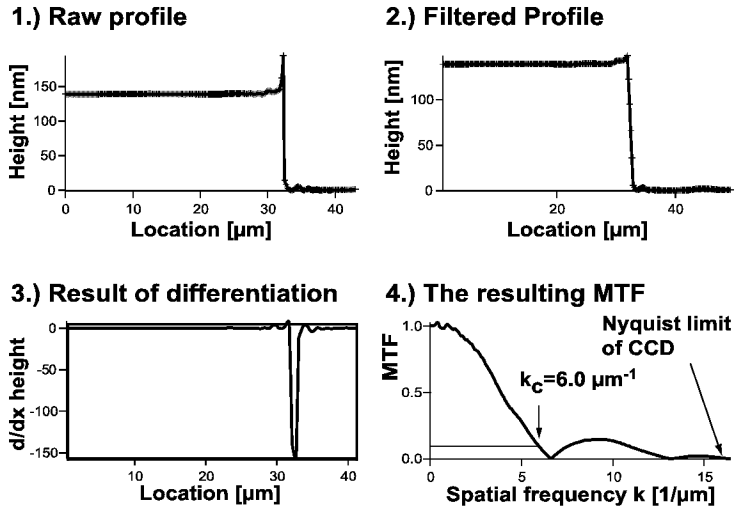

Figure 6.35: The procedure for determination of the lateral resolution is shown exemplary for a discontinuous height profile (parallel to the plane of incidence). Overshooting is reduced by application of a moving median filter. The subsequent moving average filter smears out discontinuities and is intended in order to remove spurious resolution due to artifacts (discontinuities). The kernel sizes of both filters were 5 pixels, i.e. ca 1 μm. Note that this is a very conservative choice. The modulus of the Fourier transform of the differentiated edge profile yields the MTF. The cut-off frequency k_c found here corresponds to a lateral resolution of 0.5 μm. Comparing this to the Nyquest limit $\pi/(0.191\ \mu\text{m/pixel})$ of the CCD camera reveals, that the magnification of the microscope is perfectly matched to its imaging performance.

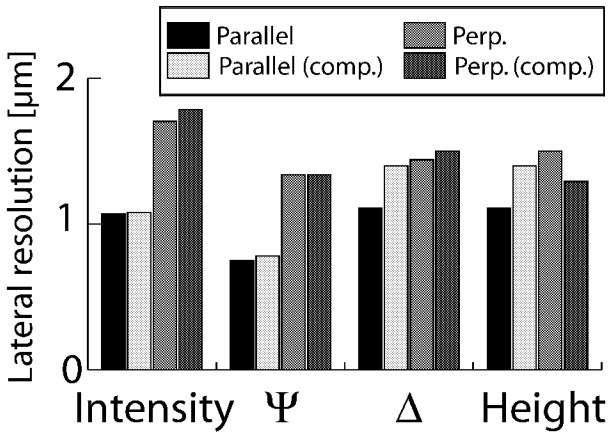

Figure 6.36: Conservative estimate of the lateral resolution of the ellipsometric microscope, determined by measurement of its modulation transfer function. Shown are maximum values for the three different sample heights.

6.4.3 The Influence of the Stray Light Pinhole on the Lateral Resolution

In order to be able to perform accurate ellipsometric measurements at the glass-water interface it was necessary to insert a stray light filtering pinhole at a plane conjugated to the back focal plane of the microscope objective (cf. Section 6.3.1). An unwanted side effect of this pinhole is its influence on the lateral resolution: Effectively this pinhole limits the numerical aperture. In order to estimate the influence of this pinhole on the lateral resolution a series of experiments with varying pinhole diameters was made. Because glass substrates with sharp structures were not available these experiments were performed at the air-silicon interface, using the silicon substrates with etched structures already described in Section 6.4. The results are shown in Fig. 6.37.

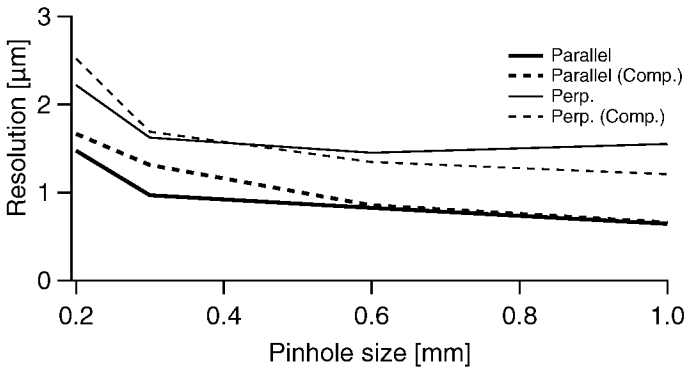

Figure 6.37: Influence of the stray light filtering pinhole on the lateral resolution: Shown are maximum values obtained from intensity profiles across three different step heights (25, 103 and 137 nm) in dependence of the diameter of the stray light filtering aperture. A significant deterioration is not observable for pinhole diameters larger than 300 μm.

A significant deterioration of the lateral resolution was only observed for the 200 μm pinhole. Note that for large pinhole diameters and structures parallel to the plane of incidence the shown values are better than without any pinhole (cf. Fig. 6.36). This just means, that the influence of large pinholes is smaller than the effect of slight defocusing due to the subjective impression of the experimentator.

Finding a quantitative model for the observed behavior is difficult. The utilized part of the objective exit pupil aperture is located at its very edge, where suboptimal behavior is expected (cf. Fig. 6.38): These regions are expected to exhibit a reduced transmission ability due to the large angles of incidence of the collected light rays. This would have to be incorporated in any accurate model.

The pinhole size for which the sudden increase of the lateral resolution limit of structures perpendicular to the plane of incidence is observed coincides with the prediction of a very

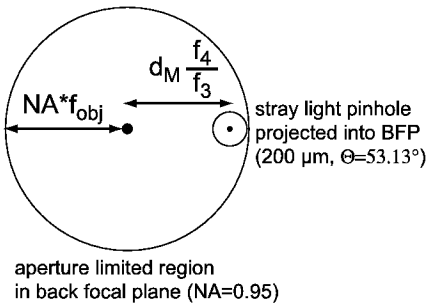

Figure 6.38: Projection of the 200 μm stray light filtering pinhole into the back focal plane (true to scale).

simple model. The slope of the curve should suddenly increase if the pinhole diameter starts to constrain the diffraction orders from both sides:

$$d_M \frac{f_4}{f_3} + \frac{D_{Ph}}{2} \cdot \frac{f_5}{f_6} \frac{f_4}{f_3} = \mathrm{NA} f_{obj} \tag{6.12}$$

For the utilized objective (NA=0.95, $f_{obj} = 3.6$ mm) and an angle of incidence $\Theta = 53.13°$ (i.e. the deflection mirror position is $d_M = 1.8$ mm, see Eq. (3.4)) a pinhole diameter of 225 μm is obtained. Transferring these findings to measurements at the glass-water interface the limit of the pinhole diameter is estimated to 320 μm (NA=1.4, $f_{obj} = 2.61$ mm, $d_M = 1.8$ mm). Of course, this would have to be validated by experiments at the glass-water interface.

6.5 Height Sensitivity

For determination of the vertical sensitivity patterned thin films of cellulose on silicon substrates were measured. The advantage of these samples was, that extremely thin films were homogeneously deposited on the substrate. The samples were kindly provided by Florian Rehfeldt (Institut für Biophysik E22, TU München) and a detailed description of the sample preparation can be found in Rehfeldt and Tanaka [2003]. The final sample had the following layer composition: As substrate served a thermally oxidized silicon waver. The oxide had a thickness of 147 ± 5 nm ($n(\lambda = 546.1\ \mathrm{nm}) = 1.465$). The oxide layer was rendered hydrophobic by grafting of self-assembled monolayers of Octadecyltrimethoxysilane (ODTMS, $d = 2$ nm, $n = 1.5$). This hydrophobicity is needed in order to allow for transfer of trimethylsilyl-cellulose (TMSC) monolayers by the Langmuir-Blodgett method. This transfer was repeated successively. Afterwards the film was dried and the hydrophobic trimethylsilyl side chains were cleaved by exposing the film to fuming HCl, resulting in a regenerated cellulose film ($d = 4.5 - 5$ nm, $n = 1.5$). Finally, the thin cellulose films were microstructured by deep UV photolitography (cf. Fig. 6.39).

Figure 6.40 presents profiles obtained along the path shown in Fig. 6.39(a). The heights shown in Fig. 6.40(a) were obtained at single pixels, whereas the data shown in Fig. 6.40(b) were computed from laterally averaged intensities (moving median and averaging filters with kernel size 5×5). The utilized kernel size is equal to the lateral resolution of the instrument and barely influences the lateral resolution (cf. Fig. 6.34). The thick layer of thermal oxide serves as a contrast layer and allows for accurate measurement of ultra thin films.

The noise level present in the measurements was determined by fitting a Gaussian function to height-histograms obtained from laterally homogeneous regions. This yielded maximum standard deviations of $\sigma = 0.5$ nm and σ =0.28 nm for heights obtained from unaveraged and averaged intensities, respectively. The observed noise level had the same magnitude as observed for thick films (cf. Section 6.1.2, Figures 6.10 and 6.11). Thus, when lateral averaging is applied, the smallest resolvable height step can be as small as 5 Å. Thereby, the averaging filters barely influence the lateral resolution (cf. Fig 6.34).

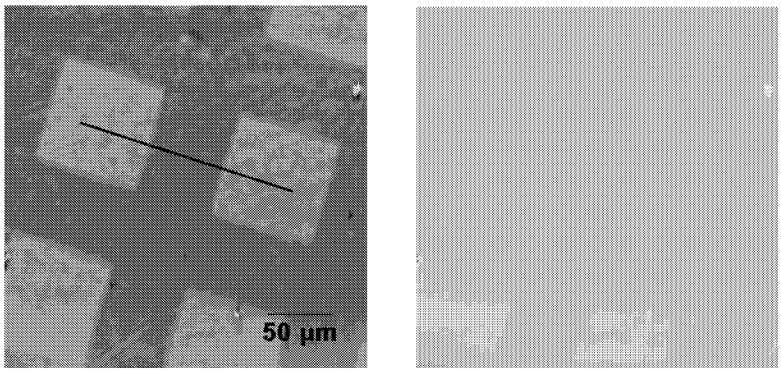

(a) (b)

Figure 6.39: (a) Ψ and (b) Δ image of a structured cellulose film (4.5-5 nm) on an oxidized ($d = 153.6$ nm) silicon substrate. The height of the oxide layer was determined by ellipsometric microscopy. In the bright areas the cellulose film was removed by UV photolitography. The angle of incidence was $\Theta = 57.6°$, the polarizer azimuth $P = 45°$.

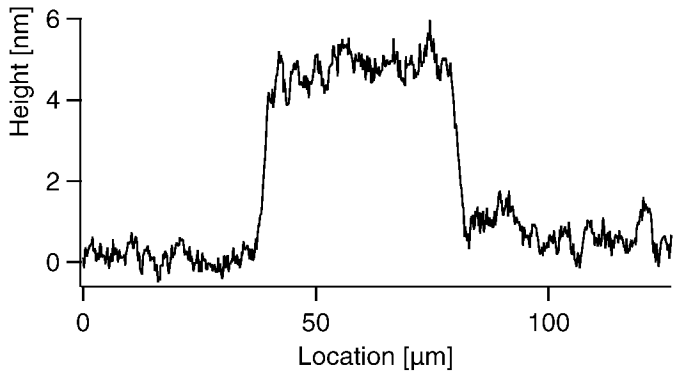

(a)

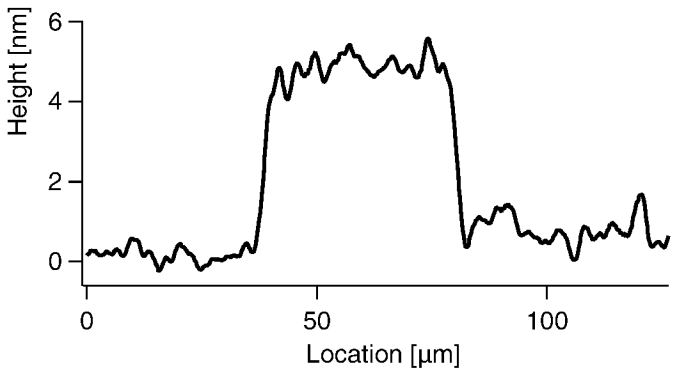

(b)

Figure 6.40: Height profiles of the structured cellulose film shown in Fig. 6.39. The data shown in (b) were computed from laterally averaged intensities (moving median and average filter with kernel size 5×5 pixels). The data shown in (a) originates from unaveraged intensities. Analyzing the width of height-histograms obtained from homogeneous regions by fitting a Gaussian function yielded the following noise levels: (a): ±0.5 nm and (b): ±0.28 nm. Thus, the smallest detectable height step can be smaller than 5 Å.

Chapter 7

Outlook

The very successful experiments performed in this work form the foundation for future applications of ellipsometric microscopy to real systems. Especially experiments at the glass-water interface offer a wide range of interesting questions, which could make full use of the additional dimension ellipsometry has to offer: Its ability to measure refractive indices with an extreme accuracy of about 0.5%. This could be used to determine quantities affecting the refracting index indirectly, e.g. temperature, concentration or mixing ratios of different surface-wetting fluids. In the following section some suggestions are formulated for technical improvements.

Shortening Measurement Times

At the moment measurements on silicon and glass substrates last for 5 and 10-14 minutes, respectively. Especially measurement times at the glass-water interface have to be reduced in order to allow for observation of dynamic processes (e.g. wetting films or moving cells). When comparing the CCD-camera exposure times utilized for each of the substrates (0.08 seconds for silicon and 4.8-8 seconds for glass substrates, respectively) it is easy to see that there is plenty of room for improvement: When measuring silicon substrates almost 5 minutes are used to adjust the rotating components. At the moment the compensator is rotated in and out at every analyzer setting, which is very time consuming. When the measurement sequence is changed such that first all measurements proceed without compensator and subsequently with it is expected that this time can be reduced to about 90 seconds.

The actual measurement time can be reduced by a factor of two if the background images were recorded only once at the beginning of a measurement series (cf. Section 5.4). The background images are recorded with the same exposure time as used for the actual measurement in order to correct for dark currents and amplifier offsets. Thus, they can be reused for subsequent measurements.

On glass substrates exposure times can be further reduced by a factor of 4 if instead of a 50

μm pinhole a 100 μm pinhole would be used. Such a pinhole is already mounted to the filter wheel holding the first pinhole. It was never used in order to avoid the introduction of an additional degree of uncertainty: The influence of the finite pinhole size on the ellipsometric performance. Now that the instrument is fully characterized and all major systematic errors have been identified nothing argues against the use of a larger pinhole. In Section 4.6 estimates about the influence of the finite pinhole size were given. A 100 μm pinhole would have negligible influence on Ψ. Outside the range $[125\ \text{nm}, 165\ \text{nm}]$ Δ would be changed by approximately 1°, in between it would be necessary to take the finite pinhole size into account. Additionally, it is expected, that the increase in incident intensity is accompanied by a considerable enhancement of image quality as the increased illumination aperture would reduce the appearance of Fresnel fringes, arising from diffraction at inevitable dust particles on the optical components.

Thus it seems feasible to reduce measurement times at glass substrates to about 3-5 minutes. Note that during this time actually two measurements are performed: one with and one without compensator. If an additional reduction of the measurement time is required this could be achieved by applying different algorithms for determination of the ellipsometric quantities. A method based on acquisition of only 4 images was presented in Cohn et al. [1988] and Cohn [1990].

Enhancing the Vertical Resolution

Figure 3.7 showed that the deflection mirror masks part of the image forming light bundles. This causes loss of the high spatial frequencies gained due to oblique illumination. By introducing a semi-transparent mirror between deflection mirror (DM) and lens 3 this masking could be avoided and might further increase the lateral resolution (cf. Fig. 7.1).

Vertical Accuracy on Glass

Enhancing the contrast of Ψ and Δ in dependence of the film thickness would allow to increase the accuracy of the determined heights. This could be achieved by using a contrast layer between substrate (glass) and the thin film of interest. Concerning silicon substrates such contrast layers in the form of thermally oxidized substrates are obligatory when ultra-thin films are investigated.

Finding an appropriate contrast layer for the glass-water interface is not trivial. It should cause good contrast for Ψ and Δ in dependence of the thin film thickness of the layer of interest. At the same time it has to be ensured that this contrast is not created by an almost singular behavior: Near $\Psi \approx 0^\circ, 90^\circ$ even small variations of the measured Fourier coefficients a, b can cause huge changes in Ψ and Δ (see Eqs. 4.1 and 4.2), i.e. ultimately the contrast in the measured quantities a, b is relevant. This can be ensured by avoiding layer systems for which $\Psi \approx 0^\circ, 90^\circ$ is expected.

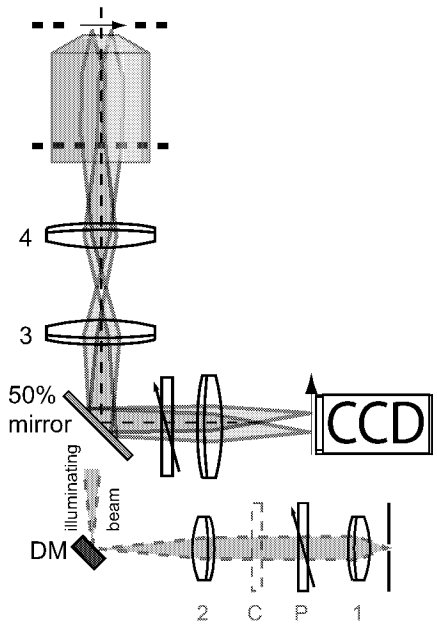

Figure 7.1: Remedy for blocking of the imaging light bundle (cf. Fig. 3.7): By introducing a semi-transparent mirror between deflection mirror (DM) and lens 3 the imaging (shown) and illuminating (partially shown) light bundles would be separated. This would prevent the loss of the high spatial frequencies gained by oblique illumination of the sample.

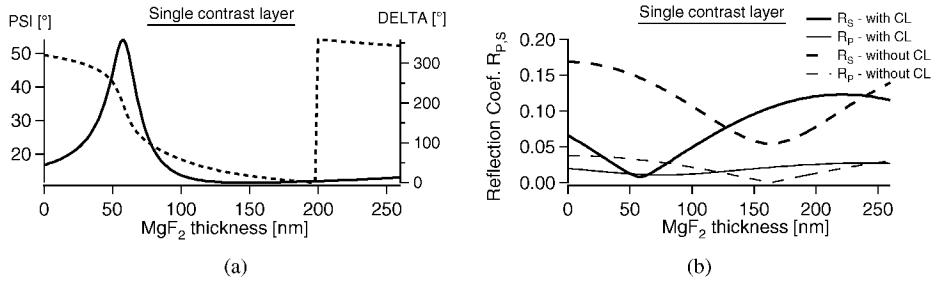

Figure 7.2: (a) Ψ (thick line) and Δ (broken line) for various film thicknesses of MgF_2 when a single contrast enhancing layer (115 nm, $n = 1.42$) is used. The incident angle is $\Theta = 46.63°$. (b) The reflection coefficients $R_{p,s}$ for various MgF_2 thicknesses with (continuous lines) and without (broken lines) the mentioned contrast layer. The reflectivities are considerably reduced resulting in increased measurement times.

For the investigation of thin films with an refractive index similar to MgF_2 a single contrast enhancing layer of 115 nm of a material with refractive index $n \approx 1.42$ would be optimum (cf. Fig. 7.2). A material with such a refractive index that can be deposited with standard techniques and is compatible to the biological system of interest might be difficult to find. That is why a second system of two contrast enhancing layers is proposed: 260 nm MgF_2 followed by 125 nm ZnS (cf. Fig. 7.3). In other applications ZnS was proved to be fairly

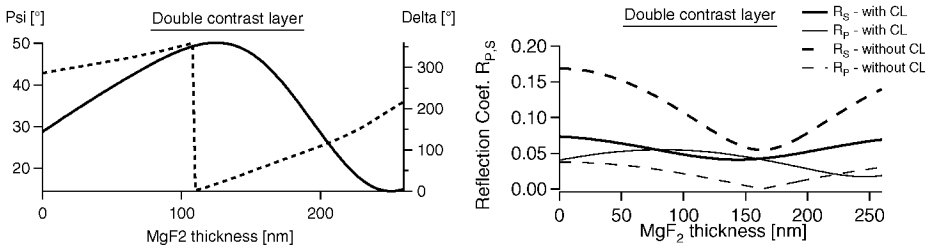

Figure 7.3: (a) Ψ (thick line) and Δ (broken line) for various film thicknesses of MgF_2 when a double contrast enhancing layer (glass, 260 nm MgF_2, 125 nm ZnS) is utilized. The incident angle is $\Theta = 46.63°$. (b) The reflection coefficients $R_{p,s}$ for various MgF_2 thicknesses with (continuous lines) and without (broken lines) the mentioned contrast layer. The reflectivities are considerably reduced, resulting in increased measurement times.

biocompatible [Chan and Nie, 1998] but contact with strong acids should be avoided as toxic hydrogen sulfide will be created. Possibly this layer system might have to be passivated with an additional thin layer of SiO_2 in order to allow for standard surface chemistry.

Unfortunately, all found contrast layers considerably decrease the reflectivity of the samples. This can be compensated for by increasing measurement times or the incident intensity as the problem of internal reflections has been solved. The latter system of contrast layers has the advantage that the reflectivity in dependence of the thin film thickness of the samples would be fairly constant, resulting in sample independent acquisition times.

Higher reflectivities and fair contrast in the ellipsometric quantities could be achieved by using a transparent support of the thin film with higher refractive index than glass cover slides. Objective and immersion liquid have to be index matched to this support in order to avoid spurious reflexes from the bottom side. Such an objective (Apo100XOHR, 100x, NA=1.65, Olympus) and the appendant cover slides and immersion liquid (n=1.78) are commercially available. Unfortunately good contrast in Ψ and Δ cannot be achieved without an additional layer. Figure 7.4 shows the reflection coefficients and the ellipsometric quantities in dependence of the MgF_2 film height when a contrast layer of 200 nm SiO_2 is employed. The incident angle was assumed to be $\Theta = 45°$. The ellipsometric contrast is very good and the reflectivity of the sample is on average much higher. Additionally the range of measurable thin film thicknesses would be considerably enlarged: Depending on the angle of incidence an absolute thin film thicknesses up to approximately 500 nm would be measurable.

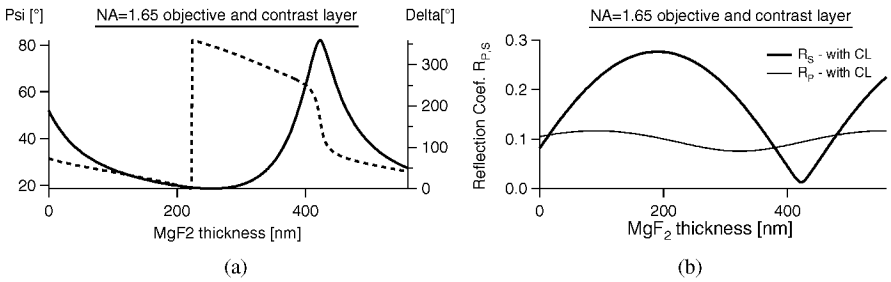

Figure 7.4: (a) Ψ (thick line) and Δ (broken line) for various film thicknesses of MgF_2 for a cover slide with refractive index n=1.78. An additional contrast layer (200 nm SiO_2 with n=1.465) was assumed. The incident angle is $\Theta = 45°$. (b) The reflection coefficients $R_{p,s}$ for various MgF_2 thicknesses. The reflectivities are on average much higher than those of all other proposed systems.

Bibliography

M. Abramowitz and I.A. Stegun. *Handbook of Mathematical Functions*. New York: Dover, 1970. 29

A. Albersdörfer, G. Elender, G. Mathe, K.R. Neumaier, P. Paduschek, and E. Sackmann. High resolution imaging microellipsometry of soft surfaces at 3μm lateral and 5 Å normal resolution. *Appl. Phys. Let.*, 72(23):2930–2932, 1998. 12

H. Arwin, S. Welin-Klintström, and R. Jansson. Off-null ellipsometry revisited: Basic considerations for measuring surface concentrations at solid/liquid interfaces. *J. Colloid Interface Sci.*, 156:377–382, 1993. 12

D.E. Aspnes. Effects of component optical activity in data reduction and calibration of rotating-analyzer ellipsometers. *J. Opt. Soc. Am.*, 64(6):812–819, 1974a. 41, 42, 45, 57

D.E. Aspnes. Optimizing precision of rotating-analyzer ellipsometers. *J. Opt. Soc. Am.*, 64 (5):639–646, 1974b. 50

R.M.A. Azzam. Oscillating-analyzer ellipsometer. *Rev. Sci. Instrum.*, 47(5):624–628, 1976. 19

R.M.A. Azzam and N.M. Bashara. *Ellipsometry and polarized light*. North Holland: Amsterdam, 1996. 9, 16, 20, 23

T. Beaglehole. Performance of a microscopic imaging ellipsometer. *Rev. Sci. Instrum.*, 59: 2557–2559, 1988. 12

J. Beuthan, O. Minet, J. Helfmann, M. Herrig, and G. Müller. The spatial variation of the refractive index in biological cells. *Physics in Medicine and Biology*, 41(3):369–382, 1996. 67

Dawn Bonnell, editor. *Scanning Probe Microscopy and Spectroscopy. Theory, Techniques and Application*. Wiley-VCH, 2001. 89

M. Born and E. Wolf. *Principles of Optics: Electromagnetic Theory of Propagation, Interference and Diffraction of Light*. New York: Cambridge University Press, 1999. 15, 26, 28, 38, 60

W.C.W. Chan and S.M. Nie. Quantum dot bioconjugates for ultrasensitive nonisotopic detection. *Science*, 281(5385):2016–2018, 1998. 124

John C. Chang, Gregory J. Brewer, and Bruce C. Wheeler. A modified microstamping technique enhances polylysine transfer and neuronal cell patterning. *Biomaterials*, 24:2863–2870, 2003. 9

Xianfu Cheng, Huibo Jia, and Duanyi Xu. Vector diffraction analysis of optical disk readout. *Applied Optics*, 39(34):6436–6440, 2000. 108

R.A. Chipman. Polarization analysis of optical systems. *Optical Engineering*, 28(2):90–99, 1989. 62, 63, 65

R.A. Chipman and L.J. Chipman. Polarization aberation diagrams. *Optical Engineering*, 28 (2):100–106, 1989. 65

R. F. Cohn. Evaluation of alternative algorithms for dynamic imaging microellipsometry. *Applied Optics*, 29:304–315, January 1990. 122

R.F. Cohn, J.W. Wagner, and J. Kruger. Dynamic imaging microellipsometry: theory, system design, and feasibility demonstration. *Applied Optics*, 27:4664–4671, 1988. 12, 122

R.W. Collins. Automated rotating element ellipsometers: Calibration, operation, and real-time applications. *Rev. Sci. Instrum.*, 61(8):2029–2062, 1990. 41, 42, 43, 44, 45, 50, 54

A.E. Conrady. *Applied Optics and Optical Design, Part I.* Oxford University Press; Dover Publications, 1957. 62

CrystalTechno LTD. Website Crystaltechno LTD. www.crystaltechno.com/Materials/ZnS.htm. 68

M.J. Dodge. Refractive properties of magnesium fluoride. *Appl. Opt.*, 23(12):1980–1985, 1984. 68

U.W. Eisenecker and C. Krzysztof. Template-Metaprogramming. Eine Einführung. *OBJEKTspektrum*, (3):96–102, 1998. 69

A. En Naciri, L. Broch, L. Johann, and R. Kleim. Fixed polarizer, rotating polarizer and fixed analyser spectroscopic ellipsometer: accurate calibration method, effect errors and testing. *Thin Solid Films*, 406(5):103–112, 2002. 19

M. Erman and J.B. Theeten. Spatially resolved ellipsometry. *J. Appl. Phys.*, 69:859–873, 1986. 11

G.D. Feke, D.P. Snow, R.D. Grober, P.J. de Groot, and L. Deck. Interferometric back focal plane microellipsometry. *Applied Optics*, 37(10):1796–1802, 1998. 10, 12

H. Haferkorn. *Bewertung optischer Systeme*. Berlin: Verlag der Wissenschaften, 1986. 38, 59

H. Harke, R. Teppner, O. Schulz, H. Orendi, and H. Motschmann. Description of a single modular optical setup for ellipsometry, surface plasmons, waveguide modes, and their imaging techniques including brewster angle microscopy. *Rev.Sci.Instrum*, 68(8):3130–3134, 1997. 12

P.S. Hauge and F.H. Dill. Design and operation of ETA, an automated ellipsometer. *IBM J. Res. Develop.*, 17(6):472–489, 1973. 19, 81

An Ilsin, Yue Cong, N.V. Nguyen, B.S. Pudliner, and R.W. Collins. Instrumentation considerations in multichannel ellipsometry for real-time spectroscopy. *Thin Solid Films*, 206(1-2): 300–305, 1991. 54, 55, 56

ISO 12233. *Photography - electronic still-picture cameras - resolution measurements*. International Organization for Standardization, 2000. 112

C.D. James, R. Davis, M. Meyer, A. Turner, S. Turner, L. Kam, G. Banker, H. Craighead, M. Isaacson, J. Turner, and W. Shain. Aligned microcontact printing of micrometer-scale poly-l-lysine structures for controlled growth of cultured neurons on planar microelectrode arrays. *IEEE Transactions on Biomedical Engineering*, 47(1):17–21, 2000. 9

G. Jin, R. Jansson, and H. Arein. Imaging ellipsometry revisited: Developments for visualization of thin transparent layers on silicon substrates. *Rev. Sci. Instrum.*, 67:2930–2936, 1996. 9, 12

P. Karageorgiev, H. Orendi, B. Stiller, and L. Brehmer. Scanning near-field ellipsometric microscope imaging ellipsometry with a lateral resolution in nanometer range. *Appl. Phys. Lett.*, 79(11):1730–1732, 2001. 13

Shuichi Kawabata. Alignment method for rotating analyzer ellipsometry. *J. Opt. Soc. Am. A*, 4(4):664+, 1987. 41

S. Kimura and T. Wilson. Confocal scanning dark-field polarization microscopy. *Applied Optics*, 33(7):1274–1278, 1994. 108

R. Kleim, L. Kuntzler, and A. El Ghemmaz. Systematic errors in rotating-compensator ellipsometry. *J. Opt. Soc. Am. A*, 11(9):2550, 1994. 19

C. Lheveder, S. Hénon, R. Mercier, G. Tissot, P. Fournet, and J. Meunier. A new brewster angle microscope. *Rev. Sci. Instrum.*, 69(3):1446–1450, 1998. 13, 14

A.-H. Liu, P.C. Wayner, and J.L. Plawsky. Image scanning ellipsometry for measuring nonuniform film thickness profiles. *Applied Optics*, 33(7):1223–1229, 1994. 12

M. Luttmann, J.L. Stehle, C. Defranoux, and J.P. Piel. High accuracy IR ellipsometer working with a Ge Brewster angle reflection polarizer and grid analyzer. *Thin Solid Films*, 313-314: 631–641, 1998. 54

Y.J. van der Meulen and N.C. Hien. Design and operation of an automated, high-temperature ellipsometer. *J. Opt. Soc. Am.*, 64(6):804–811, 1973. 41

E. Meyer, H.J. Hug, and R. Bennewitz. *Scanning Probe Microscopy - The Lab on a Tip*. Springer Verlag, Berlin Heidelberg, 2004. 89

K. Neumaier. *PhD thesis TU Munich: Entwicklung und Anwendung eines Ellipsometrischen*

Mikroskops zur lokalen Dickenmessung ultradünner, mikrostrukturierter Adsorbatfilme auf Festkörperoberflächen. Herbert Utz Verlag, 1999. 63

K.R. Neumaier, G. Elender, E. Sackmann, and R. Merkel. Ellipsometric microscopy. *Europhys. Lett.*, 49:14–19, 2000. 10

N.V. Nguyen, B.S. Pudliner, A. Ilsin, and R.W. Collins. Error correction for calibration and data reduction in rotating-polarizer ellipsometry: applications to a novel multichannel ellipsometer. *J. Opt. Soc. Am. A*, 8(6):919–931, 1991. 19, 54

J.M.M. de Nijs, A. Holtslag, and A. van Silfhout. Calibration method for rotating-analyzer ellipsometers. *J. Opt. Soc. Am. A*, 5(9):1466–1471, 1988. 41, 43

J.M.M. de Nijs and A. van Silfhout. Systematic and random errors in rotating-analyzer ellipsometry. *J. Opt. Soc. Am. A*, 5(6):773–781, 1988. 54, 57, 104

M.G. Nikolaides, S. Rauschenbach, S. Luber, K. Buchholz, M. Tornow, G. Abstreiter, and A.R. Bausch. Silicon-on-insulator thin film resistor for chemical and biological sensor applications. *ChemPhysChem*, 4:1104–1106, 2003. 71

R. Oldenbourg. Analysis of edge birefringence. *Biophys. J.*, 60(3):629–641, 1991. 109

Opto - Technological Laboratory. Website Opto - Technological Laboratory. www.optotl.ru/ZnSEng.htm. 68

H.K. Pak and B.M. Law. 2D Imaging ellipsometric microscope. *Rev. Sci. Instrum.*, 66:4972–4976, 1995. 12

Maksymilian Pluta. *Advanced Light Microscopy, Vol. 1 Principles and Basic Properties*. New York: Elsevier, 1989a. 110

Maksymilian Pluta. *Advanced Light Microscopy, Vol. 2 Specialized Methods*. New York: Elsevier, 1989b. 10, 41

W.H Press, B.P. Flannery, S.A. Teukolsky, and W.T. Vetterling. *Numerical Recipes*. Cambridge University Press, 1986. 70, 78, 114, 115

D.M. Radman and B.D. Cahan. Errors in "Effects of component optical activity in data reduction and calibration of rotating-analyzer ellipsometers". *J. Opt. Soc. Am.*, 71(12):1646, 1981. 45, 57

F. Rehfeldt and M. Tanaka. Hydration forces in ultrathin films of cellulose. *Langmuir*, 19(5): 1467–1473, 2003. 118

R. Reiter, H. Motschmann, H. Orendi, A. Nemetz, and W. Knoll. Ellipsometric microscopy. imaging monomolecular surfactant layers at the air-water interface. *Langmuir*, 8:1784–1788, 1992. 12

G.O. Reynolds, J.B. DeVelis, G.B. Parrent, and B.J. Thompson. *The New Physicsal Optics Notebook: Tutorials in Fourier Optics*. SPIE Optical Engineering Press, 1989. 27, 59, 112

B. Richards and E. Wolf. Electromagnetic diffraction in optical systems II. Structure of the image field in aplanatic systems. *Proc. Soc. London Ser. A*, 253:358–379, 1959. 108

John C. Russ. *The Image Processing Handbook*. CRC Press; 2nd edition, 1995. 73

P. Schiebener, J. Straub, J.M.H. Levelt Sengers, and J.S. Gallagher. Refractive index of water and steam as function of wavelength, temperature and density. *J. Phys. Chem. Ref. Data*, 19:677, 1990. 68

C.W. See, M.G. Somekh, and R.D. Holmes. Scanning optical microellipsometer for pure surface profiling. *Applied Optics*, 35(34):6663–6668, 1996. 12

S.V. Shatalin, R. Juskaitis, J.B. Tan, and T. Wilson. Reflection conoscopy and micro-ellipsometry of isotropic thin-film structures. *Journal of Microscopy*, 179:241–252, 1995. 10

R. Singhvi, A. Kumar, G.P. Lopez, G.N. Stephanopoulos, D.I.C. Wang, G.M. Whitesides, and D.E. Ingber. Engineering cell-shape and function. *Science*, 264(5159):696–698, 1994. 9

TIFF 6.0 Specifications. Adobe Developers Association: Adobe Systems Incorporated, TIFF 6.0 Specification. http://www.adobe.com/Support/TechNotes.html. 69

D. van Noort, J. Rumberg, E.W.H. Jager, and C.F. Mandenius. Silicon based affinity biochips viewed with imaging ellipsometry. *Meas. Sci. Technol.*, 11:801–808, 2000. 9

E. Waluschka. Polarization ray trace. *Optical Engineering*, 28(2):86–89, 1989. 62

D. Williams and P.D. Burns. Diagnostics for digital capture using MTF. *Proceedings of IS&T's PICS Conference*, 2001. 112

E. Wolf. Electromagnetic diffraction in optical systems I. An integral representation of the image field. *Proc. Soc. London Ser. A*, 253:239–257, 1959. 108

Q. Zhan and J.R. Leger. High-resolution imaging ellipsometer. *Applied Optics*, 41(22):4443–4450, 2002a. 108

Q. Zhan and J.R. Leger. Microellipsometer with radial symmetry. *Applied Optics*, 41(22): 4630–4637, 2002b. 11

Important Symbols

A	azimuthal angle of the analyzer	20
C	azimuthal angle of the compensator	21
D_{Ph}	diameter of the stray light filtering pinhole	97
D_Θ	film thickness period of Ψ and Δ	24
P	azimuthal angle of the polarizer	20
$R(P)$	residual function - used for calibration of the polarizer azimuth P	41
$R_{p,s}$	overall parallel (p) or perpendicular (s) reflection coefficient of a system of stratified planar layers	17
$T_{p,s}$	overall parallel (p) or perpendicular (s) transmission coefficient of a system of stratified planar layers	17
Δ	ellipsometric angle, represents the phase shift shift introduced due to reflection at the sample	17
Δ_{Obj}	quantity describing the instrumental polarization of the imaging optics	78
$\Gamma_{P,A}$	residual ellipticity - an imperfection of polarizers	43
$\Phi(P)$	phase difference function - used for calibration of the polarizer azimuth P	42
Ψ	ellipsometric angle, represents the ratio of the moduli of the reflection coefficients R_p and R_s	17
Ψ_{Obj}	quantity describing the instrumental polarization of the imaging optics	78
Θ	$\Theta \equiv \Theta_1$, incident angle	15
Θ_j	angle of incidence in the jth layer	15
λ	wavelength of the light	17
$\mathbf{E}_{Det}$	Jones vector of the electrical field strength at the detector	20
$\mathbf{E}_{Det}^{\dagger}$	Hermitian conjugate of $\mathbf{E}_{Det}$	21
$\text{sgn}(x)$	returns sign of x	21
$\theta(P)$	phase function - used for calibration of the analyzer azimuth A	42
a, b	Fourier coefficients of the at the detector measured intensity ($I(A)$)	21

a^c, b^c	Fourier coefficients of the at the detector measured intensity (with compensator)	22
d_j	thickness of layer j	17
f_{1-7}	focal lengths of lenses constituting the setup	32
f_{obj}	object side focal length of the microscope objective	25
f_{tube}	focal length of the tube lens	25
n_j	refractive index of layer j	15
r^p	parallel reflection coefficient at an interface	15
r^s	perpendicular reflection coefficient at an interface	15
$r^{p,s}_{j,j+1}$	reflection coefficient at an interface of layers j and $j+1$	16
t^p	parallel transmission coefficient at an interface	15
t^s	perpendicular transmission coefficient at an interface	15
INA	numerical aperture of the illumination	58
NA	numerical aperture of the objective	28

Danksagung

An dieser Stelle möchte ich allen danken, die zum Gelingen dieser Arbeit beigetragen haben. Mein Dank gilt insbesondere

... Prof. "Rudi" Merkel, der mir die Möglichkeit gab dieses Thema zu bearbeiten und mir dabei völlig freie Hand ließ - freilich nicht ohne zahlreiche wertvolle Tipps aus seinem ungeheuren Wissens- und Ideenfundus beizusteuern. Vielen Dank auch dafür, dass Du dich auf das Experiment "Fernbetreuung" eingelassen hast.

... Prof. Sackmann und Prof. Rief dafür, dass sie mich in ihrem Institut nicht nur als Gast duldeten sondern als vollwertigen E22'ler am Institutsbetrieb teilhaben ließen.

... Rudolf Lehrhuber für den guten Willen meine zahlreichen und laienhaften Konstruktionszeichnungen dem Sinn nach zu interpretieren. Viele Ideen zur konkreten Realisierung feinmechanischer Bauteile für diesen Aufbau stammen von ihm.

... Katrin Prechtel für die vielen physikalischen und weniger physikalischen Gespräche und dafür, dass sie mich für diese Arbeit angeworben hat. Als eine der letzten Optikfetischisten am Institut konnte ich in den zahlreichen Diskussionen mit Dir sehr profitieren.

... Claudia Cesa für die Präparation der strukturierten SiO_2-Siliziumsubstrate und Robert Metzke für die AFM-Messung meiner Proben - es hat wirklich Spaß gemacht mal an einem Gerät zu messen, das einfach so funktioniert!

... Jörg Schilling - dem Einzigen, mit dem man am Institut über Programmier- und Bildverarbeitungsprobleme reden konnte.

... allen Motomus, die nicht unwesentlich zur (feucht)fröhlichen Atmosphäre bei E22 beigetragen haben, aber insbesondere Olli für die Einführung und den Beistand an der Aufdampfanlage. Nicht zuletzt Motomu selber für aufmunternde Worte zwischendurch - danke!

... allen Ex-Merkels, als da wären Christian M., Melanie und Michael, die der Merkel-Gruppe ihren besonderen Flair (PuyoPuyo, Xool, etc. ...) gaben.

... allen E22'lern, die durch Hilfsbereitschaft und Kollegialität eine exzellente Arbeitsatmosphäre schufen, ohne dabei den Spaß zu kurz kommen zu lassen. Insbesondere Christian D., Manfred, Rainer, Alex, Murat, Jörg, Nök, Flo und allen anderen, die an dieser Stelle keinen Platz mehr finden.

Besonderer Dank gilt meinen Eltern, die mich immer in allen meinen Entscheidungen unterstützt haben, meiner Schwester Susi für's Korrekturlesen ausgewählter Teile der Arbeit und "last, but not least" meiner Freundin Ute für die seelische Unterstützung und psychologischen Beistand während der ganzen Arbeit.

Schriften des Forschungszentrums Jülich
Reihe Materie und Material / Matter and Materials

1. **Physik der Nanostrukturen**
   Vorlesungsmanuskripte des 29. IFF-Ferienkurses vom 9. bis 20.3.1998
   (1998), ca. 1000 Seiten
   ISBN: 3-89336-217-7

2. **Magnetische Schichtsysteme**
   Vorlesungsmanuskripte des 30. IFF-Ferienkurses vom 1. bis 12.3.1999
   (1999), ca. 1300 Seiten, zahlreiche z.T. farb. Abb.
   ISBN: 3-89336-235-5

3. **Femtosekunden und Nano-eV: Dynamik in kondensierter Materie**
   Vorlesungsmanuskripte des 31. IFF-Ferienkurses vom 13. bis 24.3.2000
   (2000), ca. 1000 Seiten, zahlreiche z. T. farb. Abb.
   ISBN: 3-89336-205-3 (Hardcover)

4. **Massenspektrometrische Verfahren der Elementspurenanalyse**
   Kurzfassungen der Vorträge und Poster des 5. Symposiums und des
   12. ICP-MS-Anwendertreffens vom 18. bis 21. September 2000 in Jülich
   zusammengestellt von H.-J. Dietze, J. S. Becker (2000), XVI, 109 Seiten
   ISBN: 3-89336-267-3

5. **Neutron Scattering**
   Lectures of the Laboratory Course
   held at the Forschungszentrum Jülich from 26 September to 6 October 2000
   herausgegeben von Th. Brückel, G. Heger, D. Richter (2000), 382 pages
   ISBN: 3-89336-269-X

6. **Baryon Excitations**
   Lectures of the COSY Workshop
   held at the Forschungszentrum Jülich from 2 to 3 May 2000
   edited by T. Barnes and H.-P. Morsch (2000), 203 pages
   ISBN: 3-89336-273-8

7. **Neue Materialien für die Informationstechnik**
   Vorlesungsmanuskripte des 32. IFF-Ferienkurses vom 05. bis 16.03.2001
   herausgegeben von R. Waser (2001), ca. 1200 Seiten, zahlreiche z. T. farb. Abb.
   ISBN: 3-89336-279-7

Schriften des Forschungszentrums Jülich
Reihe Materie und Material / Matter and Materials

8. **Deutsche Neutronenstreutagung 2001**
Kurzfassungen der Vorträge und Poster der
Deutschen Neutronenstreutagung 2001 vom 19. bis 21. Februar 2001 in Jülich
zusammengestellt von Th. Brückel (2001), XVI, 186 Seiten
ISBN: 3-89336-280-0

9. **Neutron Scattering**
Lectures of the 5th Laboratory Course
held at the Forschungszentrum Jülich from 18 September to 28 September 2001
edited by Th. Brückel, G. Heger, D. Richter, R. Zorn (2001), 418 pages
ISBN: 3-89336-288-6

10. **Soft Matter. Complex Materials on Mesoscopic Scales**
Lecture manuscripts of the 33rd IFF winter school on March 04 - 14 2002
edited by J. K. G. Dhont, G. Gompper, D. Richter (2002),
c. 1000 pages, many partly coloured illustrations
ISBN: 3-89336-297-5 (Hardcover)

11. **Proceedings of the symposium on threshold meson production in pp and pd interaction**
Extended COSY-11 Collaboration Meeting Cracow, 20 - 24 June 2001
edited by P. Moskal, M. Wolke (2002), 274 pages
ISBN: 3-89336-307-6

12. **Polarized Neutron Scattering**
Lectures of the 1st Summer School held at the Forschungszentrum Jülich
from 10 to 14 September 2002
edited by Th. Brückel, W. Schweika (2002), 360 pages
ISBN: 3-89336-314-9

13. **Beam Cooling and Related Topics**
255th International WE-Heraeus-Seminar, Bad Honnef, May 13 - 18, 2001
Proceedings
edited by D. Prasuhn (2002), PDF-Datei auf CD
ISBN: 3-89336-316-5

14. **Fundamentals of Nanoelectronics**
34th Spring School of the Department of Solid State Research,
10 - 21 March 2003, Jülich, Germany
edited by S. Bluegel, M. Luysberg, K. Urban, R. Waser (2003), c. 1000 pages
ISBN: 3-89336-319-X (Hardcover)

Schriften des Forschungszentrums Jülich
Reihe Materie und Material / Matter and Materials

15. **Neutron Scattering**
Lectures of the Laboratory course held at the Forschungszentrum Jülich
edited by Th. Brückel, G. Heger, D. Richter, R. Zorn (2003), 375 pages
New, revised edition of Materie und Material / Matter and Materials Volume 9
ISBN: 3-89336-324-X

16. **Proceedings of the 1st Summer School 2002 and Workshop on COSY Physics**
28. August - 4. September 2002
Organizing Committee: K. Brinkmann, M. Büscher, et al. (2003), CD-ROM
ISBN: 3-89336-331-9

17. **Resource-orientated Analysis of Metallic Raw Materials: Findings of CRC 525 for Aluminium**
edited by W. Kuckshinrichs, P. N. Martens (2003), CD-ROM
ISBN: 3-89336-342-4

18. **The Physics of Spallation Processes: Theory, Experiments and Applications**
by F. Goldenbaum (2004), V, 174 pages
ISBN: 3-89336-346-7

19. **Physics meets Biology: From Soft Matter to Cell Biology**
Lecture manuscripts of the 35th IFF Spring School from March 22 – April 2, 2004, Jülich, Germany
edited by G. Gompper, U. B. Kaupp, J. K. G. Dhont, D. Richter, R. G. Winkler (2004), c. 900 pages
ISBN: 3-89336-348-3

20. **Advanced Cold Moderators ACoM-6**
Proceedings of the 6th International Workshop on Advanced Cold Moderators held at Forschungszentrum Jülich from 11 to 13 September 2002
edited by H. Conrad (2004), 223 pages
ISBN: 3-89336-363-7

21. **Proceedings of the second symposium on threshold meson production in pp and pd interaction**
Extended COSY-11 Collaboration Meeting, Cracow, 1-3 June 2004
Ed. by P. Moskal (2004), c. 300 pages
ISBN: 3-89336-366-1

Schriften des Forschungszentrums Jülich
Reihe Materie und Material / Matter and Materials

22. **Ferroelectric Tunnel Junctions**
by J. Rodríguez Contreras (2004), VIII, 162 pages
ISBN: 3-89336-368-8

23. **Development of Ellipsometric Microscopy as a Quantitative High-Resolution Technique for the Investigation of Thin Films at Glass-Water and Silicon-Air Interfaces**
by F. Linke (2004), 135 pages
ISBN: 3-89336-373-4

Ellipsometric microscopy is a novel technique that combines the merits of ellipsometry and light microscopy, i.e. it allows spatially resolved, non-destructive, label-free measurements of thin film thickness and refractive index at high lateral resolution. In this book the technique is completely characterized and the steps necessary to convert ellipsometric microscopy from a qualitative technique into a reliable and quantitative method are described. The presented data show that on silicon substrates heights of thin films can be measured with a lateral resolution of 1 µm and the absolute height accuracy was found to be 1-3 nm.

Furthermore, the adaptations necessary to allow for measurements at the glass-water interface are described. This was of special interest, because it enables measurements at biologically relevant systems in their native environment – thus, opening a huge field of possible applications of ellipsometric microscopy. Especially the comparatively small differences in refractive indices between substrate (glass) and ambient medium (water) proved to be a challenge for instrument design. Film thicknesses and refractive indices can be determined now also at the glass-water interface with an accuracy of 10 nm and 0.5 %, respectively.

Forschungszentrum Jülich
in der Helmholtz-Gemeinschaft

Band/Volume 23
ISBN 3-89336-373-4

Materie und Material
Matter and Materials